ENGINEERING
LIBRARY

APR 26 1950

JOURNAL OF THE
AERONAUTICAL
SCIENCES

VOLUME 17 APRIL, 1950 NUMBER 4

CONTENTS

The Effect of Variation of Mass on the Dynamic Stability of Jet-Propelled Missiles ..... M. V. BARTON 197

Supersonic Tests of Conventional Control Surfaces on a Double-Wedge Airfoil ..... MICHAEL PINDZOLA 204

Minimum Weight of Stiffened Cylindrical Shells in Pure Bending .. W. R. MICKS 211

Analysis and Design of Stiffened Shear Webs ..... PAUL H. DENKE 217

Dynamic Stability at High Speeds from Unsteady Flow Theory ..... I. C. STATLER 232

Some Exact Solutions of the Flow Through Annular Cascade Actuator Discs ..... STEPHEN L. BRAGG AND WILLIAM R. HAWTHORNE 243

Readers' Forum: "Remarks on the Interaction Between Parallel Streams of Subsonic and Supersonic Velocities," by Mac C. Adams; "The Extension of the Prandtl-Glauert Rule," by E. V. Laitone; "Stability of Alclad Plates," by P. P. Bijlaard; "Another Note on the Velocity of Sound," by C. B. Millikan; "On Downwash Corrections in Unsteady Flow," by John W. Miles; "A Note on Boundary-Layer Type Solutions in Applied Mechanics," by S. F. Borg 250–255

Published by the
INSTITUTE OF THE AERONAUTICAL SCIENCES, INC.

JOURNAL OF THE AERONAUTICAL SCIENCES

Editor: HUGH L. DRYDEN, *Director, N.A.C.A.*

Associate Editor: ROBERT R. DEXTER *Associate Editor:* BERNEICE H. JARCK

The Institute of the Aeronautical Sciences publishes monthly the JOURNAL OF THE AERONAUTICAL SCIENCES and the AERONAUTICAL ENGINEERING REVIEW.

The JOURNAL OF THE AERONAUTICAL SCIENCES prints papers of scientific and technical interest to Institute members and subscribers. In general, it provides an opportunity for specialists to publish articles disclosing new knowledge and new applications in the field of the aeronautical sciences. The JOURNAL restricts itself to the aeronautical aspects of advances in science and engineering, and papers printed have either been submitted directly to the JOURNAL or have been previously presented at a meeting of the Institute.

The AERONAUTICAL ENGINEERING REVIEW keeps members and subscribers informed regarding the contents of new books and current periodicals in the field of aeronautics. It reviews new developments in the aircraft industry and reports on progress from house organs and catalogs published by aircraft and engine manufacturers and other companies engaged in aeronautical activities. It publishes papers on applied engineering and aircraft production. News of Institute activities is published in the REVIEW.

Statements and opinions expressed in the JOURNAL are to be understood as individual expressions of the authors and not those of the Institute.

SUBSCRIPTION RATES

Journal of the Aeronautical Sciences
Published Monthly

United States and Possessions		Foreign Countries Including Canada (American Currency Rate)	
1 Year	$12.00	1 Year	$13.00
Single Copies	1.50	Single Copies	1.50

Aeronautical Engineering Review
Published Monthly

United States and Possessions		Foreign Countries Including Canada (American Currency Rates)	
1 Year	$3.00	1 Year	$3.50
Single Copies	0.50	Single Copies	0.50

Notices of change of address should be sent to the Institute at least 30 days prior to actual change of address.

Manuscripts for publication, proofs, and all correspondence should be addressed to the Editorial Office of the JOURNAL.

Correspondence regarding subscriptions may be addressed to Publication Office, 20th and Northampton Sts., Easton, Pa., or to the Editorial Office of the JOURNAL OF THE AERONAUTICAL SCIENCES, 2 East 64th Street, New York 21, New York.

Copyright, 1950, by the Institute of the Aeronautical Sciences, Inc.

Entered as Second Class Matter at the Post Office, Easton, Pa., May 1, 1937. Acceptance for mailing at a special rate of Postage provided for in the Act of August 24, 1912. Authorized April 29, 1937.

JOURNAL OF THE AERONAUTICAL SCIENCES

VOLUME 17 APRIL, 1950 NUMBER 4

The Effect of Variation of Mass on the Dynamic Stability of Jet-Propelled Missiles*

M. V. BARTON†

The University of Texas

ABSTRACT

The variation of mass of a jet-propelled missile, caused by expending fuel, produces jet damping forces that, in addition to the variation of the mass itself, affect the dynamic stability and, hence, the flight behavior of the missile. The equations of motion in the vertical plane for an airjet-type missile and a rocket-type missile having a constant rate of loss of mass are developed, and the characteristics of the jet damping forces are indicated. The equations of motion are solved for the simplified case of a symmetrical rocket missile in free flight, and an evaluation is made to determine the effect of a gust disturbance on the subsequent behavior of the missile. These results are compared with the behavior of a constant mass missile. It is shown that the disturbance of the variable mass missile damps out more rapidly than it does for the constant mass missile, indicating that the variable mass missile is more stable. The oscillation frequency for the variable mass missile increases with time and is greater than the oscillation frequency for the constant mass missile.

INTRODUCTION

AS A JET-PROPELLED MISSILE—such as a rocket that carries its own oxygen or an airjet that takes oxygen from the atmosphere—expends fuel, its mass decreases. The effect of the loss of mass has been considered in analyses of the performance of high-altitude rockets and in the problem of escape from the earth by many investigators, among which are Malina and Smith,[1] Tsien and Malina,[2] Malina and Summerfield,[3] and Seifert, Mills, and Summerfield.[4] In these cases the dynamic stability of the missile has not been of particular concern. For rocket- or airjet-type missiles that are to be flown either guided or unguided mainly within the atmosphere, the problem of stability and control is an important consideration. Many of these missiles have aerodynamic surfaces such as wings and tails whose function is to control and stabilize the missile in flight. It has been determined that the variation in mass causes so-called jet damping forces that should be considered along with the aerodynamic forces in determining the stability of missiles. The effect of these forces caused by the variation in mass will be considered herein.

There are a number of ways of expressing the equations of motion for a system of variable mass. One of these methods involves a study of the change of momentum in an infinitesimal increment of time, and another is a study of the effective forces acting at any instant. Considering the first of these methods, it is possible to interpret Newton's equation as the equality between the change of momentum and the impulse for an interval dt, or

$$d(mV) = F\,dt$$

The change in momentum should account for the change of momentum of the initial system, as well as the change of momentum of the particles leaving the system. An understanding of the kinematics of the motion is necessary for successful application, since relative velocities between detaching particles and the parent mass must be considered.

The second method, which is the one used here, is particularly suited to systems for which the mass flow is steady. This method depends on the equality between the "effective forces" of the particles of a system and the external forces. The mass of a particle times its acceleration is called the effective force. The physical significance of the jet damping forces is clearly indicated by this method.

Received February 16, 1949.

* This investigation was undertaken as a part of the research program at the Defense Research Laboratory, The University of Texas, under Contract NOrd-9195 with the Bureau of Ordnance of the Navy Department. The author wishes to express his appreciation to the Bureau of Ordnance for the support of this work and to Dr. Dana Young for his many valuable suggestions.

† Professor of Aeronautical Engineering and Research Engineer, Defense Research Laboratory.

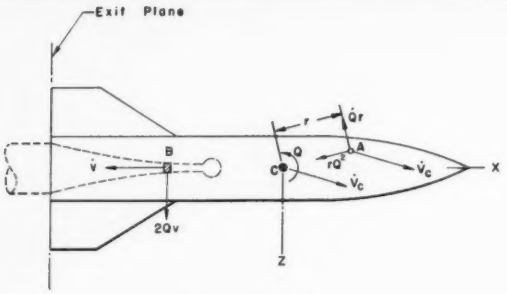

FIG. 1. Missile.

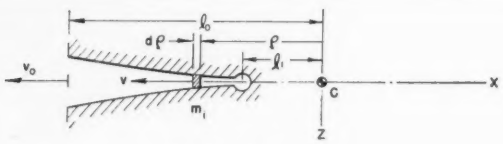

FIG. 2. Rocket jet.

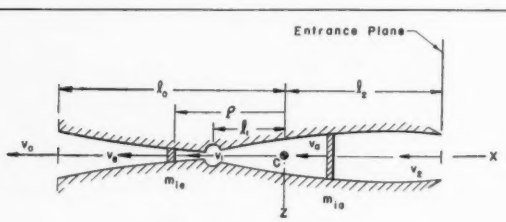

FIG. 3. Airjet flow.

EQUATIONS OF MOTION

A schematic diagram of a missile is shown in Fig. 1. Two propulsive arrangements are to be considered: the rocket unit shown in Fig. 2 and the airjet unit shown in Fig. 3. The following assumptions will be made.

(1) Only motion in a vertical plane is considered.

(2) In the case of the rocket, the system investigated at any instant consists of the missile body or frame, the jet inside the body from the exit plane to the fuel injection point, and the fuel. The airjet consists of the foregoing components plus the airflow inside the missile from the entrance plane at the nose to the fuel injection point.

(3) The external forces are lift, drag, and weight. The aerodynamic forces are caused by pressures that are measured from an atmospheric datum.

(4) The reservoir of fuel is located symmetrically about the longitudinal axis of the missile. The fuel has no velocity relative to the missile frame.

(5) The mass flow is symmetrically located about the longitudinal axis of the missile. The mass flow is steady—that is, the mass of material passing any cross section at any time is a constant.

(6) The missile is roll-stabilized, and cross-coupling terms between a symmetrical motion (roll, yaw, and sideslip) and a symmetrical motion (pitch, longitudinal displacement, and transverse displacement) are not considered.

Consider the missile shown in Fig. 1, with the X and Z axes fixed relative to the body and with the origin at C. If the missile is rotating with an angular velocity Q, then the acceleration of any particle A of the rigid frame is the vector sum of the absolute acceleration $\dot{V}_C$ of the reference point C plus the tangential acceleration $\dot{Q}r$ and the normal acceleration Q^2r of A relative to C. Since a particle B of the interior jet has a velocity v and an acceleration $\dot{v}$ relative to the rotating axes XZ, its absolute acceleration will have the acceleration $\dot{v}$ in the negative X direction and the Coriolis acceleration $2Qv$ in the Z direction, in addition to the accelerations of the type indicated for a particle of the frame.

The effective force for a particle is the product of its mass and the absolute acceleration. The effective forces for the particles of the frame and jet consist of the effective forces for both the frame and jet, as if these particles composed a rigid body, and the effective forces of the jet caused by the motion of the particles of the jet relative to the rigid body. Equating the sum of the effective forces and moment to the external forces and moment, we have

$$\left.\begin{aligned} \dot{V}_{cx}\sum^{b} m_i + \dot{Q}\sum^{b} m_i r_z - Q^2\sum^{b} m_i r_x - \sum^{j} m_i \dot{v} &= F_x \\ \dot{V}_{cz}\sum^{b} m_i - \dot{Q}\sum^{b} m_i r_x - Q^2\sum^{b} m_i r_z + 2Q\sum^{j} m_i v &= F_z \\ \dot{Q}\sum^{b} m_i r^2 + 2Q\sum^{j} m_i v\rho &= M_C \end{aligned}\right\} \quad (1)$$

where

r_x, r_z = X and Z components of distance between any particle i and C

$\sum^{b}$ = summation over all particles of body including frame, jet, and fuel at any instant

$\sum^{j}$ = summation over all particles of jet at any instant

$\dot{V}$ = dV/dt, etc.

Choosing point C as the instantaneous center of mass, then

$$\sum^{b} m_i r_x = \sum^{b} m_i r_z = 0$$

The instantaneous mass moment of inertia about C is

$$\sum^{b} m_i r^2 = I$$

The components of $\dot{V}_C$ in directions of the rotating axes X and Z are

$$\left.\begin{array}{ll} \dot{V}_X + V_Z Q & \text{in the } X \text{ direction} \\ \dot{V}_Z - V_X Q & \text{in the } Z \text{ direction} \end{array}\right\} \quad (2)$$

Using C as the center of mass and substituting the values of the components for $\dot{V}_C$ into Eq. (1) gives

$$\left.\begin{array}{l} m\dot{V}_X + mV_Z Q - \sum^{j} m_i \dot{v} = F_X \\ m\dot{V}_Z - mV_X Q + 2Q\sum^{j} m_i v = F_Z \\ I\dot{Q} + 2Q\sum^{j} m_i \rho v = M_C \end{array}\right\} \quad (3)$$

where m = total mass of missile including the jet at any instant. In the first of these equations, the term involving the jet acceleration is the jet thrust, while the jet terms in the last two equations are the jet damping force in the Z direction and the jet damping pitching moment, respectively.

In the study of stability and control of aircraft, it is usually convenient to consider only the small changes of attitude, velocities, and accelerations from a steady-state flight condition. These changes are called perturbations. The quantities are expressed in terms of a constant part plus a small change. Thus, for example, the velocity in the X direction is expressed as the sum of a constant velocity and a change in velocity.

$$V_X = U_1 + u$$

similarly,

$$Q = Q_1 + q$$

The lower case letter usually denotes the change in the quantity. This follows the notation used in Durand's *Aerodynamic Theory*.[5] The external aerodynamic forces are then composed of constant value of lift, drag, and moment plus a change in these values. These forces and moments are resolved into components in the coordinate axis directions and are expressed in terms of stability derivatives. For example,

$$F_X = X_0 + X_u u + X_w w + X_q q \quad (4)$$

where

X_0 = force in X direction caused by control movement

$X_u = \partial X/\partial u$ = rate of change of force in X direction due to change in velocity in X direction

$X_w = \partial X/\partial w$ = rate of change of force in X direction due to change in velocity in Z direction

In addition to the aerodynamic forces, the change in the components of weight in the coordinate directions as the attitude of the missile changes must be considered.

Since the mass flow of the jet has been assumed constant, the jet thrust is constant and does not appear in the equations of motion for small perturbations. By using the Durand notation, the equations of motion [Eqs. (3)] in the vertical plane become ($q = \dot{\theta}$)

$$\left.\begin{array}{l} \dot{u} - \dfrac{X_u}{m} u - \dfrac{X_w}{m} w + \left(-\dfrac{X_q}{m} + W_1\right) q + \\ \qquad\qquad g\cos\theta_1\theta = \dfrac{X_0}{m} \\ -\dfrac{Z_u}{m} u + \dot{w} - \dfrac{Z_w}{m} w + \left(-U_1 - \dfrac{Z_q}{m}\right) q + \\ \qquad\qquad \dfrac{2}{m} q\sum^{j} m_i v = \dfrac{Z_0}{m} \\ -\dfrac{M_u}{I} u - \dfrac{M_w}{I} w + \dot{q} - \dfrac{M_q}{I} q + \dfrac{2}{I} q\sum^{j} m_i \rho v = \dfrac{M_0}{I} \end{array}\right\} \quad (5)$$

where

$m = m_0 - ct$

$I = mK^2$

m_0 = initial mass at time $t = 0$ (slug)

c = mass flow, a constant (slug per sec.)

K = instantaneous radius of gyration at time t (ft.)

θ_1 = angle of missile axis from horizontal reference line for steady-state flight condition

Jet Forces for Rocket-Type Missiles

In order to determine the jet forces, the summation of the effective forces on the particles of the jet must be made. Consider the jet shown in Fig. 2. If the mass density of the gas of the jet is γ and the cross-sectional area of the jet is A at any section a distance ρ from the mass center, then for steady continuous flow

$$\begin{array}{ll} \gamma A v = c = \text{constant} \\ v = c/\gamma A \\ m_i = \gamma A\, d\rho \end{array}$$

Therefore

$$\left.\begin{array}{ll} \sum^{j} m_i v = c\displaystyle\int_{l_1}^{l_0} d\rho = c(l_0 - l_1) \\ \sum^{j} m_i \dot{v} = c\displaystyle\int^{v_0} dv = cv_0 \\ \sum^{j} m_i \rho v = c\displaystyle\int_{l_1}^{l_0} \rho d\rho = (c/2)(l_0^2 - l_1^2) \end{array}\right\} \quad (6)$$

Hence, in Eqs. (3) the jet thrust is cv_0, and the jet damping terms are $2Qc(l_0 - l_1)$ and $Qc(l_0^2 - l_1^2)$. In a similar manner, the corresponding terms in Eqs. (5) can be determined. The equations of motion are, therefore,

$$\left.\begin{array}{l} m\dot{V}_X + mV_Z Q - cv_0 = F_X \\ m\dot{V}_Z - mV_X Q + 2c(l_0 - l_1)Q = F_Z \\ I\dot{Q} + c(l_0^2 - l_1^2)Q = M_C \end{array}\right\} \quad (7)$$

and the equations in terms of the perturbations are

$$
\left.\begin{aligned}
&\dot{u} - \frac{X_u}{m}u - \frac{X_w}{m}w + \left(-\frac{X_q}{m} + W_1\right)q + g\cos\theta_1\theta = \frac{X_0}{m}\\
&-\frac{Z_u}{m}u + \dot{w} - \frac{Z_w}{m}w + \left(-U_1 - \frac{Z_q}{m}\right)q + 2\frac{c}{m}(l_0 - l_1)q + g\sin\theta_1\theta = \frac{Z_0}{m}\\
&-\frac{M_u}{I}u - \frac{M_w}{I}w + \dot{q} - \frac{M_q}{I}q + \frac{c}{I}(l_0^2 - l_1^2)q = \frac{M_0}{I}
\end{aligned}\right\} \quad (8)
$$

The last set of the equations of motion can be simplified by making certain assumptions and approximations.

Thus, for a missile having symmetry about two planes and having zero incidence between the longitudinal axis and the flight path for a steady flight condition and flying horizontally at supersonic speed so that Z_q/m can be neglected in comparison with U_1, the equations of motion become

$$
\left.\begin{aligned}
&\dot{u} - (X_u/m)u + g\theta = X_0/m\\
&\dot{w} - \frac{Z_w}{m}w + \left[2\frac{c}{m}(l_0 - l_1) - U_1\right]q = \frac{Z_0}{m}\\
&-\frac{M_w}{I}w + \dot{q} + \left[\frac{c}{I}(l_0^2 - l_1^2) - \frac{M_q}{I}\right]q = \frac{M_0}{I}
\end{aligned}\right\} \quad (9)
$$

Jet Forces for Airjet-Type Missiles

The jet forces for the airjet-type missile will be developed in a manner similar to those for the rocket, the main difference being that the flow of air from the entrance plane to the fuel injection point must also be considered in the case of the airjet.

The jet terms in Eqs. (3) will be evaluated in two parts: one involving the entering air and the other the exhaust jet, as shown in Fig. 3. Using the subscript a to denote the values pertaining to the airflow and e for the exhaust jet, then for steady flow at any cross section

$$
\begin{aligned}
v_a &= c_a/\gamma_a A_a\\
v_e &= c_e/\gamma_e A_e
\end{aligned}
$$

where $c_e - c_a = c$, rate of mass of fuel flow; also

$$
\begin{aligned}
m_{ia} &= \gamma_a A_a d\rho\\
m_{ie} &= \gamma_e A_e d\rho
\end{aligned}
$$

Therefore

$$
\left.\begin{aligned}
\sum^j m_i v &= c_a\int_{-l_2}^{l_1} d\rho + c_e\int_{l_1}^{l_0} d\rho = c_a(l_2 + l_1) + c_e(l_0 - l_1)\\
\sum^j m_i \dot{v} &= c_a\int_{v_2}^{v_1} dv + c_e\int_{v_1}^{v_0} dv = c_a(v_1 - v_2) + c_e(v_0 - v_1)\\
\sum^j m_i \rho v &= c_a\int_{-l_2}^{l_1}\rho\, d\rho + c_e\int_{l_1}^{l_0}\rho\, d\rho = \frac{c_a}{2}(l_1^2 - l_2^2) + \frac{c_e}{2}(l_0^2 - l_1^2)
\end{aligned}\right\} \quad (10)
$$

where

v_1 = velocity of mass flow at point where fuel is added
v_2 = air inlet velocity at entrance plane
v_0 = jet outlet velocity at exit plane

The jet thrust can be expressed in terms of the fuel mass flow and air mass flow as $c(v_0 - v_1) + c_a(v_0 - v_2)$. Similarly, the jet damping force and moment are, respectively,

$$
\begin{aligned}
&2[c(l_0 - l_1) + c_a(l_2 + l_0)]Q\\
&[c_a(l_0^2 - l_2^2) + c\,(l_0^2 - l_1^2)]Q
\end{aligned}
$$

The equations of motion for the airjet therefore can be expressed as

$$
\left.\begin{aligned}
&m\dot{V}_X + mV_Z Q - [c(v_0 - v_1) + c_a(v_0 - v_2)] = F_X\\
&m\dot{V}_Z - mV_X Q + 2[c(l_0 - l_1) + c_a(l_2 + l_0)]Q = F_Z\\
&I\dot{Q} + [c_a(l_0^2 - l_2^2) + c(l_0^2 - l_1^2)]Q = M_C
\end{aligned}\right\} \quad (11)
$$

or

$$
\left.\begin{aligned}
&\dot{u} - \frac{X_u}{m}u - \frac{X_w}{m}w + \left(-\frac{X_q}{m} + W_1\right)q + g\cos\theta_1\theta = \frac{X_0}{m}\\
&-\frac{Z_u}{m}u + \dot{w} - \frac{Z_w}{m}w + \left(-U_1 - \frac{Z_q}{m}\right)q + \frac{2}{m}[c(l_0 - l_1) + c_a(l_2 + l_0)]q = \frac{Z_0}{m}\\
&-\frac{M_u}{I}u - \frac{M_w}{I}w + \dot{q} - \frac{M_q}{I}q + \frac{1}{I}[c(l_0^2 - l_1^2) + c_a(l_0^2 - l_2^2)]q = \frac{M_0}{I}
\end{aligned}\right\} \quad (12)
$$

As for the rocket, these last equations for specified steady flight conditions can be simplified to

$$\left.\begin{aligned}
&\dot{u} - (X_u/m)u + g\theta = X_0/m \\
&\dot{w} - \frac{Z_w}{m}w + \\
&\left\{\frac{2}{m}[c(l_0 - l_1) + c_a(l_2 + l_0)] - U_1\right\} q = \frac{Z_0}{m} \\
&-\frac{M_w}{I}w + \dot{q} + \\
&\left\{\frac{1}{I}[c(l_0^2 - l_1^2) + c_a(l_0^2 - l_2^2)] - \frac{M_q}{I}\right\} q = \frac{M_0}{I}
\end{aligned}\right\} \quad (13)$$

Significance of Jet Damping Terms

The terms for the jet damping of the rocket given in Eqs. (9) are $2(c/m)(l_0 - l_1)q$ for the force in the Z direction and $(c/I)(l_0^2 - l_1^2)q$ for the pitching moment. It is interesting to note that, since l_1 locates the position of the origin of the mass which is eventually ejected and l_0 locates the position of the detachment of the mass from the main body, if the detaching mass originates at the point where it is ejected so that $l_0 - l_1 = 0$, then there are no jet damping forces. The influence of the jet damping force in the Z direction depends on the relative magnitude of $2(c/m)(l_0 - l_1)$ and U_1, which occur together in the coefficient for q. Since U_1 is the velocity in the X direction, which in this case has been taken as supersonic, it is likely that for many rockets $U_1 \gg (2c/m)(l_0 - l_1)$, so that $(2c/m)(l_0 - l_1)$ can be neglected in comparison with U_1. A similar situation exists for the terms in the jet damping pitching moment where $(c/I)(l_0^2 - l_1^2)$ is compared with M_q/I. In this case, however, it is possible to have the value of $(c/I) \times (l_0^2 - l_1^2)$ 10 to 20 per cent or more of the value of M_q/I.

Similarly, for the equations of motion for the airjet, the jet damping terms may be small in comparison with the values of quantities with which they are combined. It should be noted, however, that the magnitude of the jet damping terms may be somewhat higher than before, since they include the effect of the mass flow of air throughout the length of the body.

Solution of Equations

Even though the magnitude of the jet damping terms may be small relative to the other quantities with them, the character of the solution of the equations of motion for the variable mass missile may be quite different from the solution of the equations for the constant mass missile because of the fact that in the former case the coefficients in the equations are not constant.

Since the last two equations of the simplified equations of motion for the rocket [Eqs. (9)] and the airjet [Eqs. (13)] contain only the two unknowns w and q, it is possible to express them in terms of one unknown q. Thus, for the special case of free flight with no control forces acting so that $X_0 = Z_0 = M_0 = 0$, both sets of equations can be written in the form

$$m^2\ddot{q} + Am\dot{q} + (B + Cm)q = 0 \quad (14)$$

where, for the rocket,

$$\begin{aligned}
A &= K^{-2}[c(l_0^2 - l_1^2 - K^2) - M_q - Z_wK^2] \\
B &= K^{-2}[Z_wM_q - Z_wc(l_0^2 - l_1^2) + 2M_wc(l_0 - l_1)] \\
C &= -M_wU_1K^{-2}
\end{aligned}$$

and, for the airjet,

$$\begin{aligned}
A &= K^{-2}[c(l_0^2 - l_1^2 - K^2) + c_a(l_0^2 - l_2^2) - M_q - Z_wK^2] \\
B &= K^{-2}\{Z_wM_q - Z_w[c(l_0^2 - l_1^2) + c_a(l_0^2 - l_2)^2] + 2M_w[c(l_0 - l_1) + c_a(l_2 + l_0)]\} \\
C &= -M_wU_1K^{-2}
\end{aligned}$$

Changing to m as the independent variable so that $y = qm$, then Eq. (14) may be written as

$$m^2y'' + amy' + (b + em)y = 0 \quad (15)$$

where $y' = dy/dm$, etc. The substitution $y = m^\beta x$ transforms Eq. (15) into Bessel's differential equation in $x(m)$, so that, finally, the solution of Eq. (14) becomes

$$\left.\begin{aligned}
q &= m^{-(a+1)/2}[C_1J_\nu(2\sqrt{em}) + C_2Y_\nu(2\sqrt{em})] \\
w &= m^{-(a+1)/2}\{C_1[DJ_\nu(2\sqrt{em}) + E2\sqrt{em}J_{\nu+1}(2\sqrt{em})] + \\
&\qquad C_2[DY_\nu(2\sqrt{em}) + E2\sqrt{em} \times Y_{\nu+1}(2\sqrt{em})]\}
\end{aligned}\right\} \quad (16)$$

where, for the rocket,

$$\begin{aligned}
\nu &= \sqrt{(-a+1)^2 - 4b} \\
a &= -\{1 + K^{-2}[(l_0^2 - l_1^2) - c^{-1}(M_q + Z_wK^2)]\} \\
b &= 1 + K^{-2}\{(l_0^2 - l_1^2) + c^{-1}[-Z_w(l_0^2 - l_1^2) + 2M_w(l_0 - l_1) - (M_q + Z_wK^2)] + c^{-2}Z_wM_q\} \\
e &= -c^{-2}K^{-2}M_wU_1 \\
D &= M_w^{-1}[c(l_0^2 - l_1^2 + K^2) + (cK^2/2)(a + 1 - \nu) - M_q] \\
E &= (cK^2/2)M_w^{-1} \\
J &= \text{Bessel's function of the first kind} \\
Y &= \text{Bessel's function of the second kind} \\
C_1, C_2 &= \text{arbitrary constants}
\end{aligned}$$

In general, the Bessel's functions in Eqs. (16) are of high order and large argument so that an asymptotic approximation can be effectively used. The form used herein is

$$J_\nu(x) \doteq \frac{\cos[x - (\pi/4) - (\nu\pi/2)]}{\sqrt{(1/2)\pi x}}$$

$$Y_\nu(x) \doteq \frac{\sin[x - (\pi/4) - (\nu\pi/2)]}{\sqrt{(1/2)\pi x}}$$

The particular problem of the effect of a gust will be considered. If we assume that a gust velocity of w_0 in the Z direction is suddenly applied at the time the

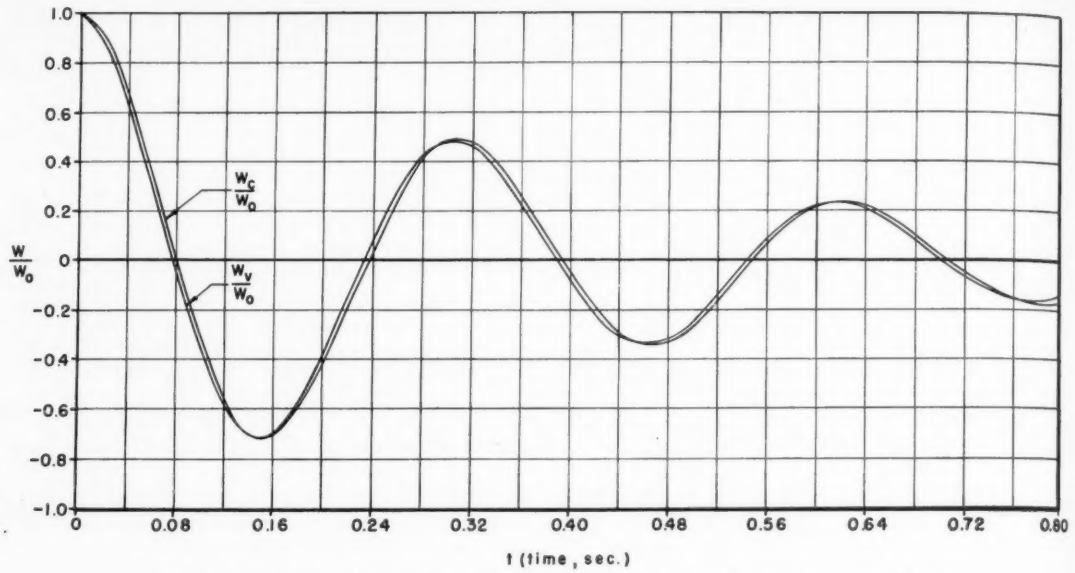

FIG. 4. Effect of disturbance W_0 on behavior of a variable mass and a constant mass missile.

missile is in steady free flight, then the boundary conditions to be satisfied are $w = w_0$ at $t = 0$ and $q = 0$ at $t = 0$. These conditions determine the values of C_1 and C_2 so that Eqs. (16) become

$$\left.\begin{aligned} \frac{w}{w_0} &= \left(\frac{m}{m_0}\right)^{-[(a/2)+(3/4)]}\left[\frac{D}{E2\sqrt{em_0}}\sin 2\sqrt{e}\times(\sqrt{m_0}-\sqrt{m}) + \left(\frac{m}{m_0}\right)^{3/4}\cos 2\sqrt{e}\times(\sqrt{m_0}-\sqrt{m})\right] \\ \frac{q}{w_0} &= \frac{1}{E2\sqrt{em_0}}\left(\frac{m}{m_0}\right)^{-[(a/2)+(3/4)]}\sin 2\sqrt{e}\times(\sqrt{m_0}-\sqrt{m}) \end{aligned}\right\} \quad (17)$$

These values give curves of damped oscillations of changing frequency with time.

Comparison of Variable Mass and Constant Mass Rockets

In order to obtain an idea of the effect of the variation in mass on the motion and stability of a rocket, the solution for a particular rocket will be compared with one for which it is assumed the mass is constant.

The solution of Eqs. (9), assuming m is a constant and $c = 0$ for the same boundary conditions as before—namely, $w = w_0$ and $q = 0$ at $t = 0$—is

$$\left.\begin{aligned} \frac{w}{w_0} &= e^{\alpha t}\left[\cos\omega t + \left(\frac{\alpha}{\omega} - \frac{M_q}{mK^2\omega}\right)\sin\omega t\right] \\ q/w_0 &= (M_w/mK^2\omega)\, e^{\alpha t}\sin\omega t \end{aligned}\right\} \quad (18)$$

where

$$\alpha = (1/2m_0K^2)(M_q + Z_wK^2)$$

$$\omega = \frac{1}{2m_0K}\sqrt{-K^{-2}(M_q + Z_wK^2)^2 + 4(Z_wM_q - M_wU_1m_0)}$$

Eqs. (17) and (18) have been evaluated for the following hypothetical values:

m_0	= 15 slugs	M_q	= −300 lbs. ft. sec.
c	= 0.25 slug per sec.	K	= 2.5 ft.
Z_w	= −20 lbs. sec. per ft.	l_0	= 5 ft.
Z_q	= −20 lbs. sec.	l_1	= 0
M_w	= −20 lbs. sec.	U_1	= 1,900 ft. per sec

The results for the transverse velocity w are shown in Fig. 4. In this figure, the subscript c denotes the constant mass missile and the subscript v denotes the variable mass missile. It is evident in this case that, since the curves have decreasing amplitude with time, both the constant mass missile and the variable mass missile are dynamically stable. Further, since the amplitude of the velocity of the variable mass missile decreases more rapidly than that for the constant mass missile, the net effect of the jet damping forces and variations in mass is to increase the dynamic stability. These curves are indicated for too short a time to show the effect, but the frequency of the oscillation of the variable mass missile is increasing with time, whereas the frequency for the other missile is constant.

The ratio of the amplitudes of the pitching velocity and transverse velocity, as determined by the envelope of the curves of the type in Fig. 4, has been determined, and the results are shown in Fig. 5. The amplitude of the velocity for the variable mass is always less than for the constant mass missile. Since the amplitude of the motion damps out rapidly, it is somewhat academic

to compare the ratios of the amplitudes of the motion for a time much over 1 sec. However, the curves in Fig. 5 have been determined for a period of 10 sec. to show the trend of the ratios as the time becomes large.

The frequency of oscillation of the variable mass missile is not a constant. The ratio of the frequency of the variable mass missile and the constant mass missile is indicated in Fig. 5. It is evident in this case that the frequency of oscillation for the variable mass missile only becomes slightly greater than that for the constant mass missile even 10 sec. after the disturbance w_0.

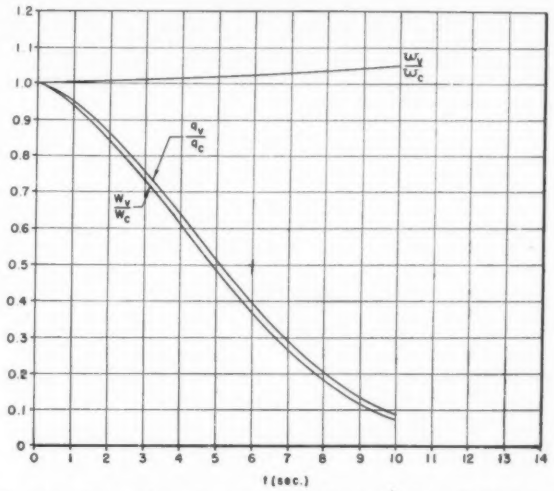

FIG. 5. Comparison of velocity amplitudes and oscillation frequencies of a variable mass and a constant mass missile.

REFERENCES

[1] Malina, F. J., and Smith, O. M. A., *Flight Analysis of Sounding Rocket*, Journal of the Aeronautical Sciences, Vol. 5, No. 5, pp. 199–202, March, 1938.

[2] Tsien, H. S., and Malina, F. J., *Flight Analysis of a Sounding Rocket with Special Reference to Propulsion by Successive Impulses*, Journal of the Aeronautical Sciences, Vol. 6, No. 2, pp. 50–58, December, 1938.

[3] Malina, F. J., and Summerfield, M., *The Problem of Escape rom the Earth by Rocket*, Journal of the Aeronautical Sciences, Vol. 14, No. 8, pp. 471–480, August, 1947.

[4] Seifert, H. S., Mills, M. M., and Summerfield, M., *The Physics of Rockets*, American Journal of Physics, May–June, 1947.

[5] Durand, W. F., *Aerodynamic Theory*, Vol. 5, Division N, Chapt. V; Durand Reprinting Committee, Pasadena, Calif., January, 1943.

[6] Watson, G. H., *Theory of Bessel Functions;* Cambridge University Press, 1945.

Notice to Contributors

Manuscripts submitted for publication *must* be double- or triple-spaced originals. There should be wide margins on both sides of the sheets and triple spacing around formulas to allow for the marking of directions for the printer.

Original drawings (jet black India ink on white paper or tracing cloth) should accompany the manuscript. (*Blueprints are not acceptable.*) Photographs *must* be on glossy white paper. The smallest lettering on 8- by 10-in. figures should be no less than 1/4 in. high.

Only the simplest formulas should be typewritten; all others should be carefully written in pen and ink. The difference between capital and lower-case letters and Greek symbols should be clearly distinguished.

See Inside Back Cover of this issue for further details.

Supersonic Tests of Conventional Control Surfaces on a Double-Wedge Airfoil

MICHAEL PINDZOLA*
United Aircraft Corporation

SUMMARY

Results of supersonic tunnel tests made to obtain the characteristics of conventional control surfaces are summarized. A symmetrical double-wedge airfoil of 7 per cent thickness, with 15 and 30 per cent trailing-edge flaps, was used as a model. Pressure measurements and Schlieren photographs of the airfoil were taken in a two-dimensional channel at Mach Numbers 1.38, 1.48, and 1.58. The pressure data were reduced to lift coefficient, drag coefficient, lift to drag ratio, section moment coefficient, flap moment coefficient, and center of pressure points for every test angle of attack. Comparisons of the experimental data were made with the linearized and shock-expansion theories of references 1, 2, and 3. Agreement with Busemann's second-order linear theory and the shock-expansion theory is good except where such unpredictable phenomena as the following exist: (1) the shock detachment from the leading edge of the airfoil, (2) the forward movement of the shock emanating at the hinge point of the flap, and (3) separation on the upper flap surface to a limiting case at which the top trailing-edge shock moves to the hinge point. The tests were especially significant in determining the effects of these irregularities on airfoil characteristics. Since a presentation of all the material would be somewhat lengthy, only representative results are given in this paper.

DESCRIPTION OF TEST EQUIPMENT

THE U.A.C. RESEARCH DEPARTMENT WIND TUNNEL, in which this investigation was made, is a two-dimensional channel of 3.7 by 15.4-in. cross section at the test section. Continuous operation is obtained through a vacuum-type system in which part of the mass airflow can be recirculated. This feature allows a simple control of the stagnation air temperature, which was kept constant at 175°F. At this temperature, condensation was eliminated in the test section.

Nozzles were designed for Mach Numbers 1.4, 1.5, and 1.6 by the method of characteristics, with a boundary-layer correction of 0.010 in. per in. of the nozzle length downstream of the throat. Subsequent calibration showed the correction to be slightly conservative, since actual Mach Numbers of 1.38, 1.48, and 1.58 were obtained. Nozzles were constructed of laminated mahogany with a high luster finish.

The model was mounted from the tunnel floor on a strut of $^1/_4$-in. thickness. A biconvex windshield enclosed this strut and, in addition, the pressure tube leads and a rod to set the airfoil angle of attack. The changing of the angle of attack was possible during operation.

A single-pass, double-mirror Schlieren optical system was used to observe the flow field. Both spark and time-exposure photographs of the flow pattern were obtained.

DESCRIPTION OF MODELS

The basic model for this investigation was a 6-in. chord symmetrical double-wedge airfoil of 7 per cent thickness. Detachable flaps were machined to fit the airfoil as shown in Fig. 1. Since the sting interrupted the flow over the bottom airfoil surface, flaps were machined at both positive and negative slopes to obtain pressure data for both surfaces. Two sets of flaps intercepting 15 and 30 per cent of the chord length, respectively, were made with fixed deflection angles of plus and minus 5°, 10°, 15°, and 20°. Pressure taps were installed in two rows along the chord with a total of eight on the upper forward surface and ten on the flap and portion of the upper rear surface of the wedge. In addition, a check tap was installed on the bottom forward surface.

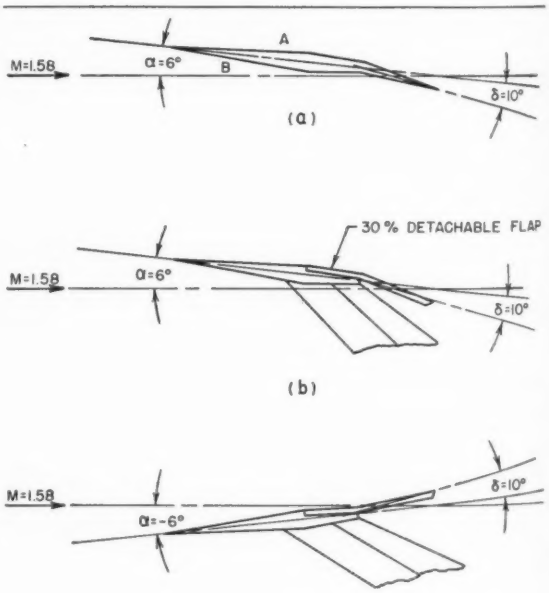

FIG. 1.

Presented at the Aerodynamics Session, Annual Summer Meeting, I.A.S., Los Angeles, July 21–22, 1949.

* Research Engineer.

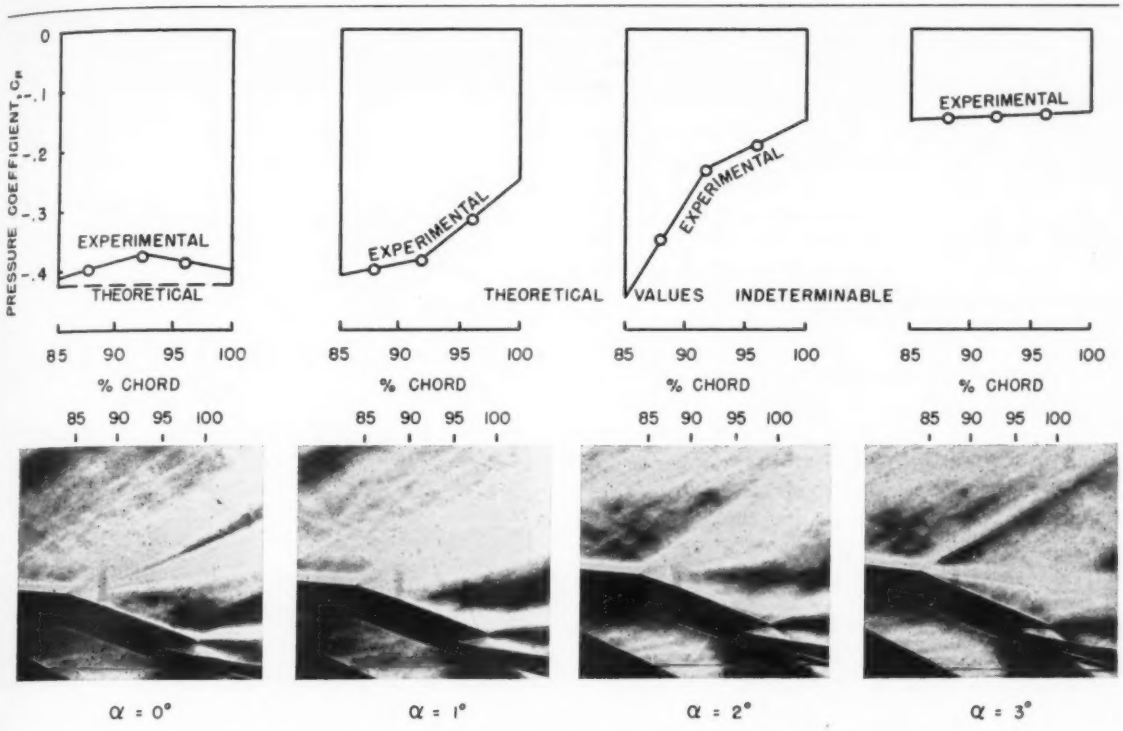

FIG. 2. Separation effects at $M = 1.48$ on 15 per cent chord flap deflected 15°.

METHOD OF OBSERVATION

A complete set of pressure data and a Schlieren photograph were taken at angle-of-attack increments of 1° through a range indicated in Table 1.

TABLE 1

Flap		Angle-of-Attack Range		
% Chord	Deflection, Deg.	$M = 1.38$	$M = 1.48$	$M = 1.58$
15	0	−3 to 3	−7 to 7	−9 to 9
15	5	−3 to 1	−7 to 4	−9 to 6
15	10	−3 to 1	−7 to 3	−8 to 5
15	15	−3 to 1	−7 to 3	−8 to 5
15	20	−4 to 0	−7 to 2	−9 to 4
30	0	−3 to 3	−7 to 7	−9 to 9
30	5	−4 to 3	−7 to 4	−9 to 6
30	10	−4 to 1	−7 to 3	−9 to 4
30	15	...	−7 to 0	−9 to 2
30	20	...	−7 to −1	−9 to 0

Limits were dictated by bow shock detachment at the negative angles and by either complete separation or hinge shock detachment at the positive angles.

The interruption of flow caused by the sting on the bottom surface of the airfoil made pressure readings on this surface meaningless. Therefore, to obtain a complete airfoil pressure distribution for any given set of conditions, data from two separate runs were used. For example, Fig. 1a shows the airfoil with a 30 per cent chord, 10° downward deflected flap operating at $\alpha = 6°$ and $M_0 = 1.58$. The pressure distribution data for surface A are obtained from the run on the configuration in Fig. 1b at $\alpha = 6°$. Corresponding data for surface B are obtained from the run on the configuration in Fig. 1c at $\alpha = -6°$.

DISCUSSION

Since the nature and effects of the irregularities in the flow pattern cannot be predicted by existing theory, a discussion of them is of interest. This is most easily accomplished with the aid of Schlieren photographs and corresponding pressure distribution diagrams shown in Figs. 2, 3, and 4. These typical examples were taken from the runs at Mach Number 1.48 on the 15 per cent chord flaps. The theoretical results shown in the diagrams were computed by the shock-expansion theory.

Separation

The series of diagrams and photographs of Fig. 2 shows various stages of boundary-layer separation. As separation increases, the pressure on the portion of the flap affected approaches free-stream static pressure. Where separation is complete, as at $\alpha = 3°$, the trailing-edge shock moves forward to the hinge point. Lift and pressure drag of the airfoil are decreased with the existence of this condition. The center of pressure of the airfoil moves forward.

Hinge Shock Forward

The plots and photographs depicting the hinge shock forward irregularity are shown in Fig. 3. Note that the flaps in the photographs are deflected upward, simulating the bottom surface of an airfoil with downward flap deflection. Under normal conditions, a shock originates at the lower surface hinge point of the airfoil as shown in Fig. 3 at $\alpha = -2°$. This shock turns the air stream through the angle of the flap deflection. However, when previous disturbances slow the air stream down to a Mach Number at which this shock detaches, it moves forward, in effect making a longer flap. This condition is shown at $\alpha = -4°$. The increase in pressure behind this shock thus acts over a greater portion of the airfoil. Although it would appear that the experimental pressure coefficients on this effective flap would drop below the theoretical, such was not the case on any flap where the hinge shock moved forward. An increase in lift and pressure drag results, in addition to a rearward shift of the location of the center of pressure.

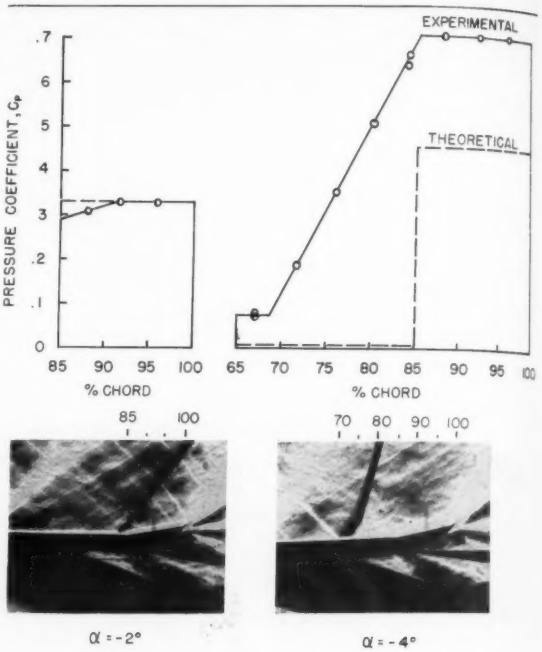

FIG. 3. Hinge shock forward effect at $M = 1.48$ on 15 per cent chord flap deflected 10°.

Detached Bow Shock

Comparative plots and photographs at points of attached and detached bow shocks are shown in Fig. 4. At $\alpha = -7°$, the upper forward surface is inclined at too great an angle for the particular free-stream Mach Number, and the bow wave separates from the wedge tip. This causes a high pressure at the leading edge of the airfoil which decreases steadily to the theoretically predicted value. The results are an increase in lift curve slope, an increase in drag, and a forward shift of the airfoil center of pressure location.

COMPARISON WITH THEORY

The experimental results of this test were compared with the first- and second-order linear theories of references 1 and 2, as well as the shock-expansion theory of reference 3. In all cases, the results agree favorably with the second-order linear and shock-expansion theories up to points where irregularities occur. A representative set of comparative characteristic curves is given in Figs. 5 through 9. These were obtained at a Mach Number of 1.58 on the airfoil with a 30 per cent chord deflected 15°. During test, the bow shock was detached at angles of attack of −8° and −9° for this run. Partial separation of the flow on the top flap surface occurred at 0° angle of attack. Separation was complete at the 1° and 2° points.

LIFT COEFFICIENT

The curves of the lift coefficient, C_L, versus angle of attack, α, are shown in Fig. 5. The experimental curve crosses the zero ordinate at −3.5°. Corresponding values for the first-order linear, second-order linear, and shock-expansion theories are −4.5°, −3.7°, and −3.9°,

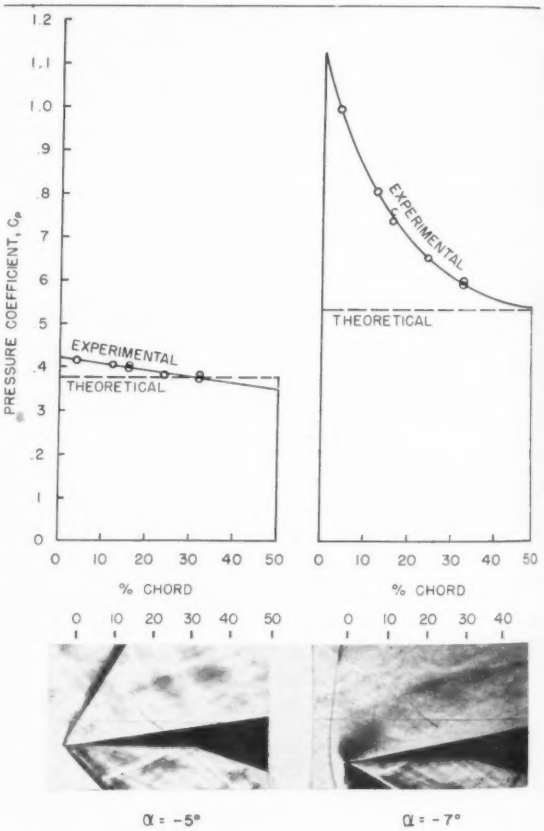

FIG. 4. Detached bow shock effect at $M = 1.48$ on airfoil of 7 per cent thickness.

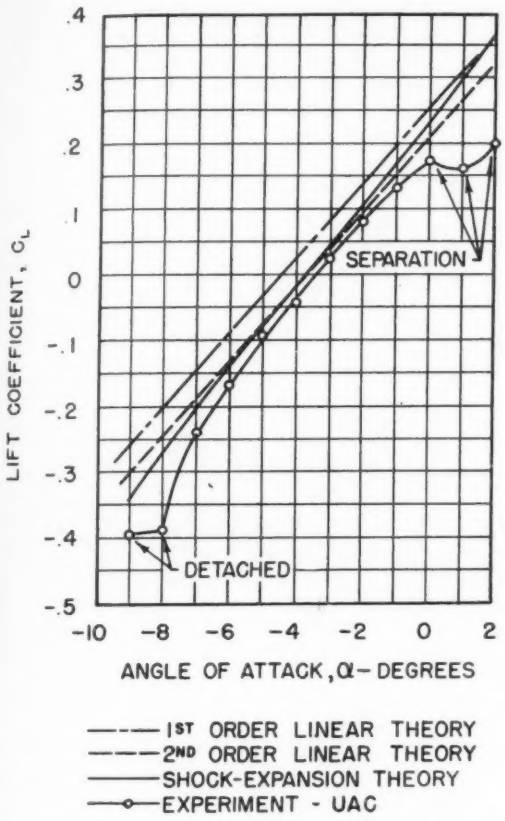

FIG. 5. Experiment vs. theory at $M = 1.58$ on airfoil with 30 per cent chord flap deflected 15°.

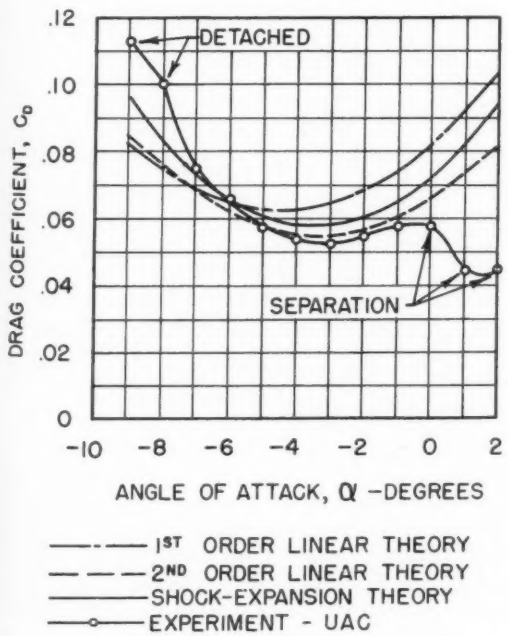

FIG. 6. Experiment vs. theory at $M = 1.58$ on airfoil with 30 per cent chord flap deflected 15°.

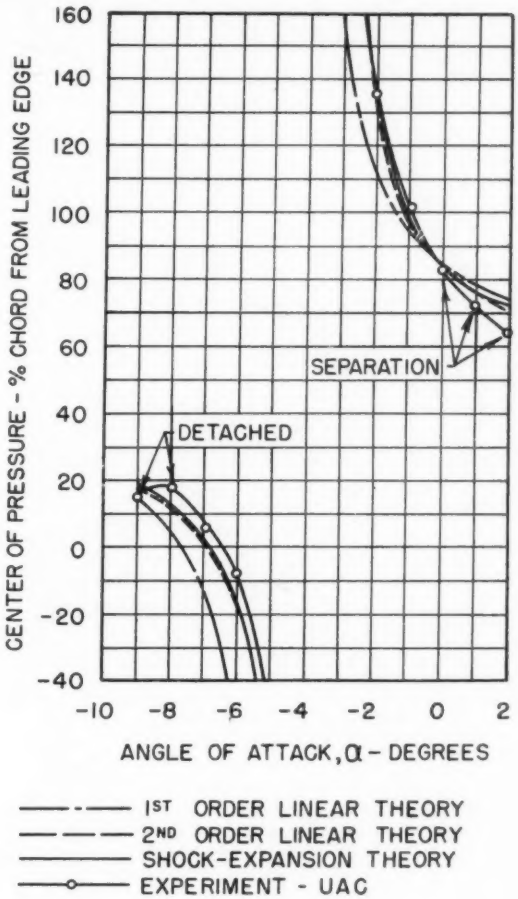

FIG. 7. Experiment vs. theory at $M = 1.58$ on airfoil with 30 per cent chord flap deflected 15°.

respectively. In the region of zero lift, the experimental curve of lift coefficient is practically linear. However, when separation occurs, a loss in lift results. In passing from an attached to a detached bow shock condition, the slope of the lift coefficient curve increases rapidly. However, once the shock is detached, the coefficient increases slowly.

Drag Coefficient

Fig. 6 shows the drag coefficient, C_D, curves obtained by experiment and theory. The experimental curve follows the familiar parabolic shape for angles at which the lift coefficient curve is linear. Agreement with the second-order theory is good in this region. However, when irregularities occur, deviations from the parabola exist. In the case of separation, the drag coefficient decreases, while with a detached bow shock the opposite is true. These drag coefficient values represent pressure drag only, and friction drag may alter the shape of the curve, especially in the region of separation.

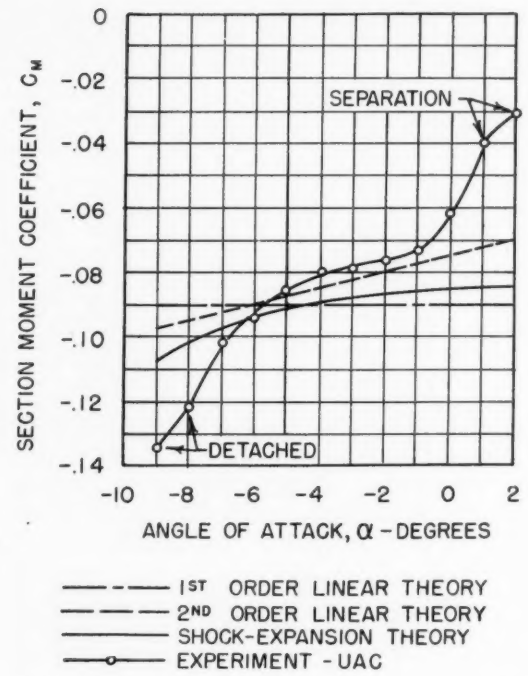

FIG. 8. Experiment vs. theory at $M = 1.58$ on airfoil with 30 per cent chord flap deflected 15°.

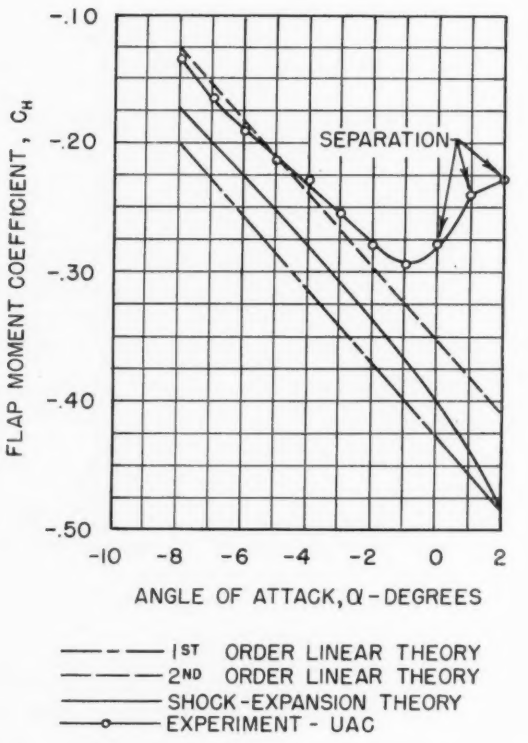

FIG. 9 Experiment vs. theory at $M = 1.58$ on airfoil with 30 per cent chord flap deflected 15°.

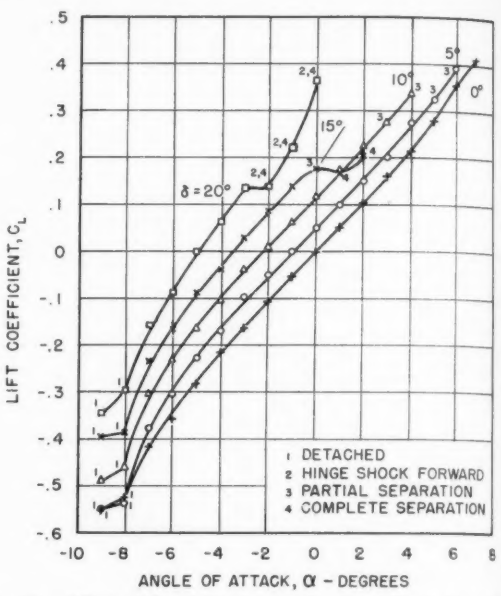

FIG. 10. Effect of flap deflection angle, δ, on C_L at $M = 1.58$ with 30 per cent chord flap.

Center of Pressure

The center-of-pressure results are shown in Fig. 7 in terms of the per cent chord from the leading edge. Agreement of the second-order linear and shock-expansion theories with experiment is again good. At the angle of zero lift, the center of pressure is at infinity. As the angle of attack is changed in either direction from the zero lift angle, the center of pressure approaches the mid-chord position.

Section Moment Coefficient

Fig. 8 shows the section moment coefficient, C_M, curves. These moment coefficients were obtained by integrating the elemental moments about the 50 per cent chord position. A positive moment was taken as that tending to raise the leading edge of the airfoil. Agreement of the experimental results is best with the second-order linear theory. The effect of irregularities in the flow pattern was to increase the slope of the moment coefficient curve.

Flap Moment Coefficient

The curves of flap moment coefficient, C_H, are shown in Fig. 9. These coefficients are for the flap section about the hinge point and are useful in determining control loading. The second-order linear theory approximates these loads accurately up to a point where separation on the flap occurs. Since separation tends to increase the pressure on the upper flap surface, the flap hinge moments decrease.

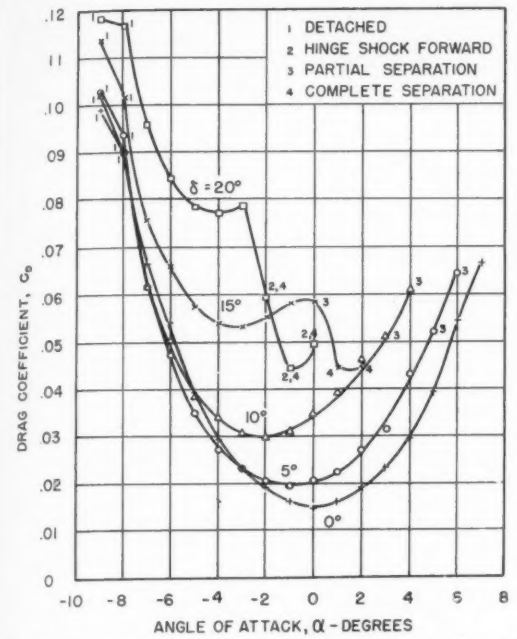

FIG. 11. Effect of flap deflection angle, δ, on C_D at $M = 1.58$ with 30 per cent chord flap.

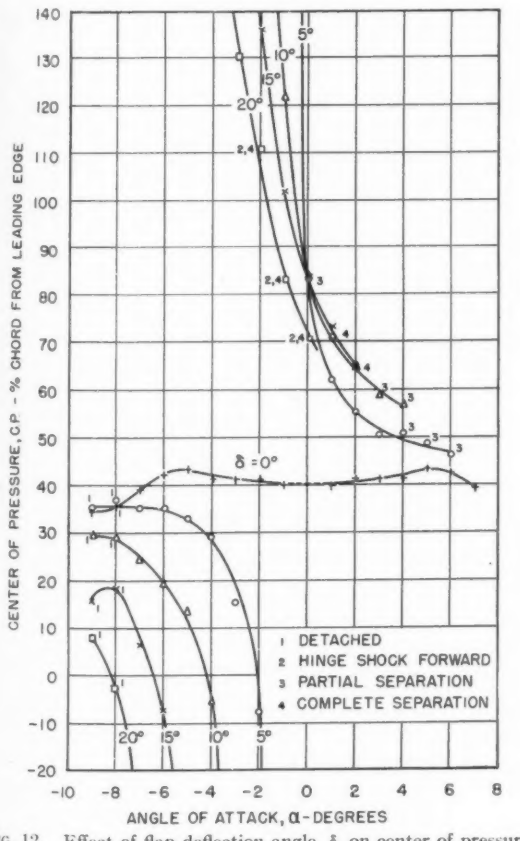

FIG. 12. Effect of flap deflection angle, δ, on center of pressure at $M = 1.58$ with 30 per cent chord flap.

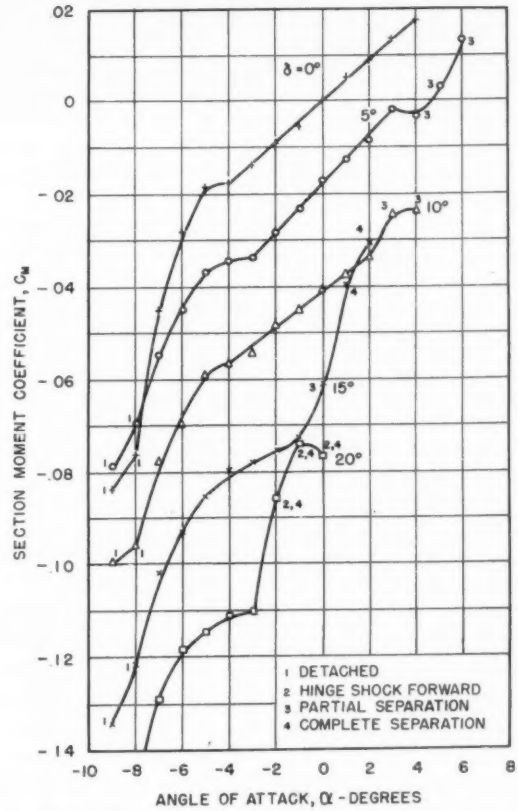

FIG. 13. Effect of flap deflection angle, δ, on C_M at $M = 1.58$ with 30 per cent chord flap.

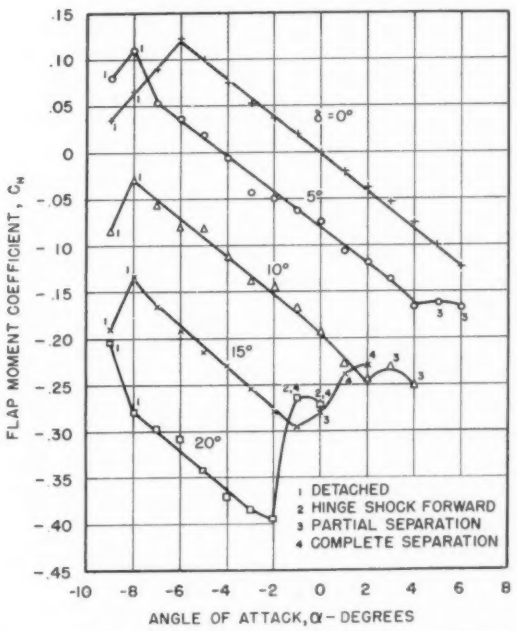

FIG. 14. Effect of flap deflection angle, δ, on C_H at $M = 1.58$ with 30 per cent chord flap.

Summary Curves

Figs. 10 through 14 show the effect of flap deflection angle, δ, on the displacement of the characteristic curves. The plots were made from experimental data of runs at Mach Number 1.58 on the 30 per cent chord flaps which include the run compared with theory above. The displacement of the curves is consistent in regions where no irregularities exist. However, where irregular conditions are present, the curves deviate in accordance with the irregularity as discussed previously. The deviations at angles of attack of $-8°$ to $-9°$ are caused by a detached bow shock in all runs. Partial separation has little effect on all but the flap moment coefficients. Complete separation has an appreciable effect on all characteristics as shown by the plots of the 15° and 20° deflection runs at the high angles of attack. These effects are canceled somewhat on the 20° run by the existence of the hinge shock forward condition. Similar trends are obtained with either 15 or 30 per cent chord flaps at other Mach Numbers, although the displacements of the curves are less with the shorter flap.

Fig. 15, a cross-plot of Fig. 10, shows the effect of flap deflection angle, δ, on the lift coefficient at constant angles of attack. Theoretical curves computed by the shock-expansion method are included to indicate the effectiveness of the flaps. At any constant angle of attack, the lift coefficient increases with an increase in flap deflection angle. However, the experimental results indicate less increase than the theoretical, since the experimental pressure distributions on the flap are slightly lower than those predicted.

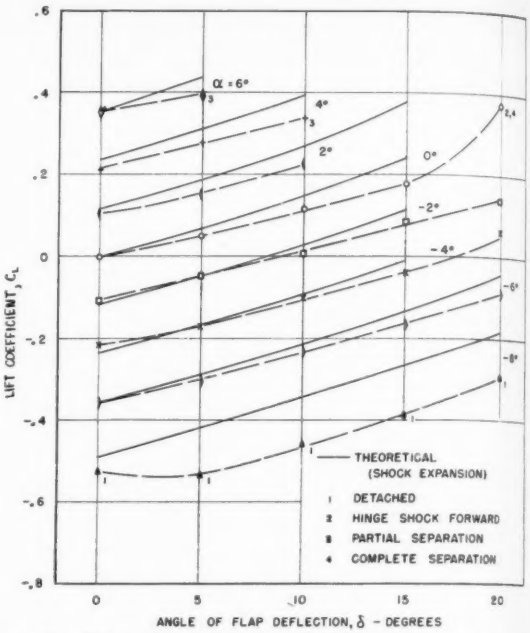

FIG. 15. Effect of flap deflection angle, δ, on C_L at constant angle of attack, α, and $M = 1.58$ with 30 per cent chord flap.

References

[1] Collar, A. R., *Theoretical Forces and Moments on a Thin Airfoil with Hinged Flap at Supersonic Speeds*, R. and M. 2004, November, 1943.

[2] Lock, C. N. H., *Examples of the Application of Busemann's Formula to Evaluate the Aerodynamic Force Coefficients on Supersonic Aerofoils*, R. and M. 2101, September, 1944.

[3] Ivey, H. R., Stickle, G. W., and Schuettler, A., *Charts for Determining the Characteristics of Sharp-Nose Airfoils in Two-Dimensional Flow at Supersonic Speeds*, N.A.C.A. T.N. No. 1143, January, 1947.

Minimum Weight of Stiffened Cylindrical Shells in Pure Bending

W. R. MICKS*
The RAND Corporation

SUMMARY

Methods previously developed for determining minimum weight of stiffened cylindrical shells in bending[1] are extended to include the weight of the circumferential frames. For a specified diameter and bending moment it is possible to minimize the total weight of shell and frames. Curves are presented showing the variation of frame weight, panel weight, and total weight with variations in structural index and frame spacing. These curves may be used to indicate the weight penalty incurred by using nonoptimum design.

DERIVATION

THE TOTAL WEIGHT of the stiffened shell is considered to be composed of two parts: the weight of the circumferential frames and the weight of the sheet-stringer combination that comprises the panel structure between frames.

The total average weight per inch length of shell may be written

$$W_T' = W_P' + W_F' \tag{1}$$

where

W_P' = average panel weight per inch length (prime indicates "per inch")
W_F' = average frame weight per inch length

Assuming that the cross section is circular and that the panel proportions are the same all around the circumference, the panel weight is given by

$$W_P' = \pi D t w_p \tag{2}$$

where

D = diameter of shell
t = average thickness of panel
w_p = density of panel material

The weight of frames (per inch length of shell) is

$$W_F' = \pi D A_F w_F / L \tag{3}$$

where

A_F = cross-sectional area of the frame
L = frame spacing
w_F = density of frame material

It is shown in reference 2 that the stiffness required of the frame cross section, in order to prevent general instability, can be expressed by

$$E_F I_F = C_f M D^2 / L \tag{4}$$

where

E_F = modulus of elasticity of frame material
I_F = moment of inertia of the frame cross section
C_f = a dimensionless coefficient[2]

An analysis of test data has shown that a stiffened cylinder having a value of C_f above a critical value (actually a critical range) will exhibit a panel type of failure wherein the shell buckles between frames, leaving the frames undistorted. As the present analysis is based on the assumption of designing to prevent a general instability failure, the value of C_f will be chosen accordingly.

Assuming that the value of E is known, the required moment of inertia, I_F, must be related to the weight (or cross-sectional area) of the frame. This will be accomplished by use of the dimensionless shape parameter[1] k_4, where $k_4 = I_F/A_F^2$.

This parameter may be thought of as an "efficiency factor" for the frame cross section in bending.

Transposing,

$$I_F = k_4 A_F^2 \tag{5}$$

Substituting Eq. (5) in Eq. (4), the required cross-sectional area of the frame is

$$A_F^2 = C_f M D^2 / k_4 L E_F \tag{6}$$

This may be written

$$A_F = (D M^{1/2} / L^{1/2})(C_f / k_4 E_F)^{1/2} \tag{6a}$$

Substituting Eq. (6a) in Eq. (3), the average frame weight per inch becomes

$$W_F' = (\pi D^2 M^{1/2} w_F / L^{3/2})(C_f / k_4 E_F)^{1/2} \tag{7}$$

It can be seen from Eq. (7) that, as C_f decreases, the frame weight will decrease. However, a lower limit is fixed for C_f by the stipulation of a panel-type failure. For any value of C_f above this limit, the frames will obviously be overweight, as far as general instability is concerned.

It should be noted that Eq. (7) shows the frame weight to be proportional to the factor $w_F/\sqrt{E_F}$, which is density divided by the *square root* of the modulus of elasticity. This indicates that, with other factors remaining the same, the use of some material other than aluminum alloy may effect a saving in frame

Received July 11, 1949.
* Engineer.

weight. For example, the factor $w_F/\sqrt{E_F}$ is 2.55×10^{-5} for magnesium alloy as compared with 3.09×10^{-5} for aluminum alloy. Therefore, the ratio of the weight of a magnesium-alloy frame to the weight of an aluminum-alloy frame having the same cross-section proportions and the same value of EI is approximately 0.826. It should be pointed out, however, that, although the above figures show that a lighter frame could be made from magnesium, the magnesium frame will be larger in cross section. In order to have the same EI as the aluminum frame, all dimensions of the magnesium frame cross section will be multiplied by the factor $[E(\text{Al})/E(\text{Mg})]^{1/4}$, which equals 1.13. Therefore, the amount of weight that can be saved is dependent on any size restrictions that might be imposed on frame depth or other frame dimensions.

Eqs. (7) and (2) are added to give the total average weight per inch length.

$$W_T' = \pi D\bar{t}w_p + \frac{\pi D^2 M^{1/2} w_F}{L^{3/2}}\left(\frac{C_f}{k_4 E_F}\right)^{1/2} \qquad (8)$$

Assuming that the frames and panel are made from materials of the same density, $w_p = w_F$.

Also let

$$C_2 = (C_f/k_4 E_F)^{1/2} \qquad (9)$$

Eq. (8) may be expressed in terms of total average cross-sectional area. (NOTE: The term "total average area" will be used to denote average volume of panel and frames per unit length of cylinder.)

$$A = \pi D\bar{t} + (\pi C_2 D^2 M^{1/2}/L^{3/2}) \qquad (10)$$

The average panel thickness $\bar{t}$ may be expressed as

$$\bar{t} = q_{max.}/f_c = 4M/\pi D^2 f_c \qquad (11)$$

where

$q_{max.}$ = maximum compressive load per inch width
f_c = allowable compressive stress (average) in the panel

Substituting Eq. (11) in Eq. (10)

$$A = (4M/Df_c) + (\pi C_2 D^2 M^{1/2}/L^{3/2}) \qquad (12)$$

In order to compare different configurations (different ratios of L/D or different types of panel construction) of stiffened cylinders at different intensities of loading, Eq. (12) will be expressed in terms of the structural index M/D^3 for members in bending and the nondimensional frame spacing L/D.

By algebraic manipulation, Eq. (12) is put in the form

$$\frac{A}{M^{2/3}} = \frac{4(M/D^3)^{1/3}}{f_c} + \frac{\pi C_2}{(M/D^3)^{1/6}(L/D)^{3/2}} \qquad (13)$$

In this form, the equation eliminates all effects of size and considers only proportions and stresses.

When any two geometrically similar cylinders composed of the same material are loaded in bending to equal values of M/D^3, they will develop equal values of $A/M^{2/3}$, regardless of their relative sizes. If M represents the ultimate moment, then A is the total average area of cross section required to carry this value of moment. Therefore, $A/M^{2/3}$ is a direct measure of the weight of cylinder required to carry a given value of moment at a specified value of M/D^3. (NOTE: This neglects possible second-order effects caused by change of stress gradient with size and changes of the stress-strain curve with variation in size.)

Another advantage of expressing Eq. (13) in terms of the structural index is that M/D^3, together with L/D, can be converted into the structural index q/L_0 for axially loaded compression panels. As there are available curves of allowable average stress f_c vs. q/L_0 for many types of sheet-stiffener panels,[1] data from these curves may be used directly in estimating the weight of a stiffened cylindrical shell. The value of q/L_0 is determined as follows:

The load per inch width q is taken as the maximum value for the cylinder in bending.

$$q = q_{max.} = 4M/\pi D^2$$

Assuming end restraint to be zero, the effective panel length L_0 is equal to the frame spacing L. Therefore,

$$q/L_0 = 4M/\pi D^2 L \qquad (14)$$

Expressed in terms of the structural index,

$$q/L_0 = 4(M/D^3)/\pi(L/D)$$

After q/L_0 is calculated, the value for f_c in Eq. (13) is read from a curve of f_c vs. q/L_0 corresponding to the type of panel used in construction of the shell. Such a curve is shown in Fig. 5.

EXAMPLE

To illustrate the methods outlined above, Eq. (13) will be plotted for an example case, as shown in Figs. 1–3.

The following assumptions are made:

(1) The lower limit of C_f is 1/16,000.[2]

(2) The value of the coefficient C_2 remains constant. This implies that, after a frame material is specified and a value is chosen for C_f, the cross sections of all frames are geometrically similar (or, more generally, have equal values of k_4).

(3) The panel is constructed of 24ST sheet with formed stiffeners designed to optimum proportions. Values for the allowable compressive stress f_c will be read from the curve of f_c vs. q/L_0 shown in Fig. 5. This curve, reproduced from reference 1, is an envelope curve representing the upper limit of stress which has been attained in tests of 24ST sheet-stiffener panels having formed stiffeners.

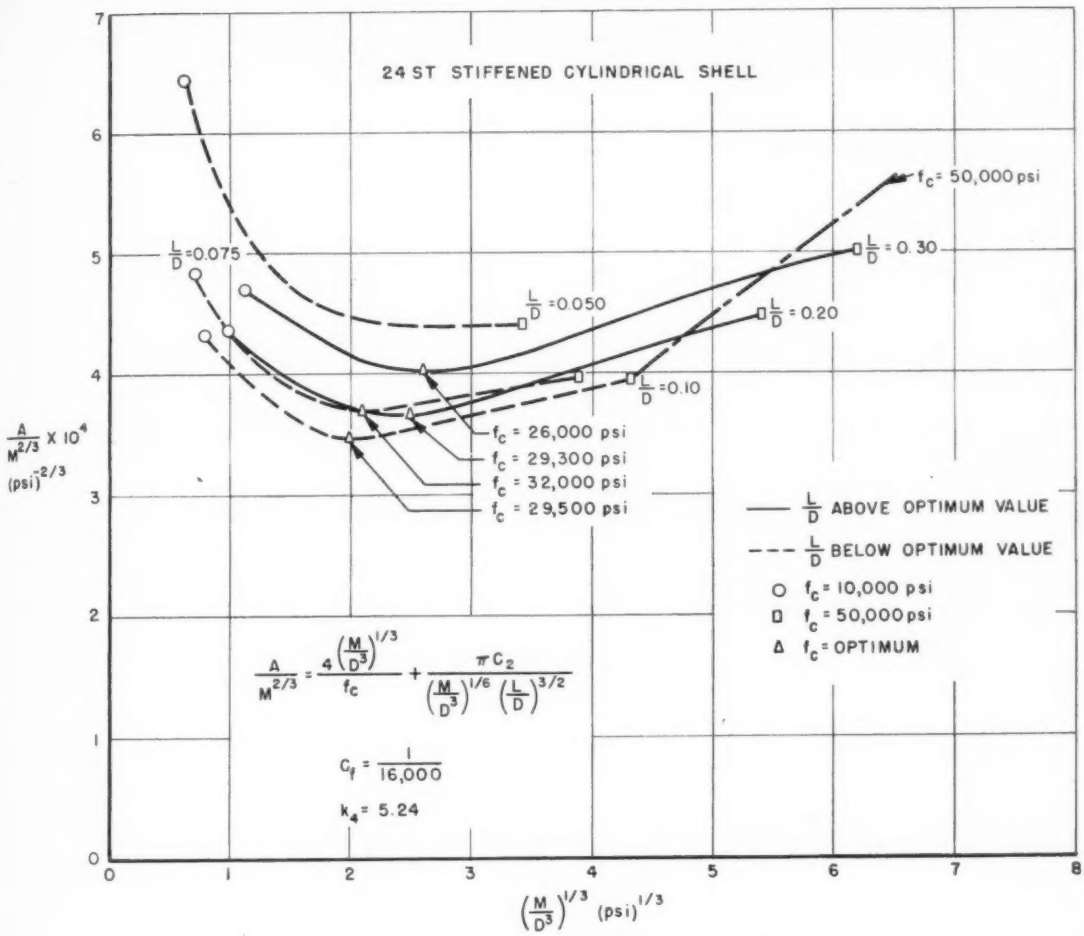

FIG. 1 TOTAL AVERAGE CROSS-SECTIONAL AREA

The value of the shape factor k_4 is based on the proportions of the frame cross section shown below.

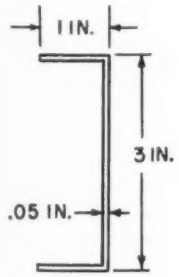

AREA = .25 IN.^{2}
I_F = .328 IN.^{4}
k_4 = 5.24

SHAPE OF FRAME CROSS SECTION

Assuming $E_F = 10^7$ lbs. per sq.in. and substituting the above value of k_4 in Eq. (9), C_2 is found to be 1.09×10^{-6}.

In evaluating $A/M^{2/3}$ from Eq. (13), the ratio L/D is held constant as M/D^3 is varied. A value of q/L_0

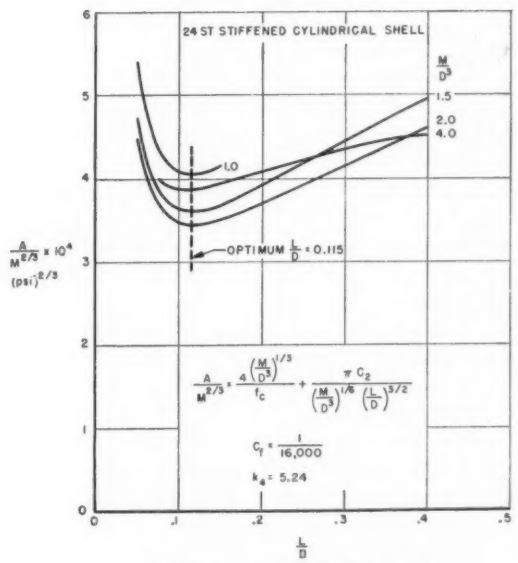

FIG. 2 OPTIMUM FRAME SPACING

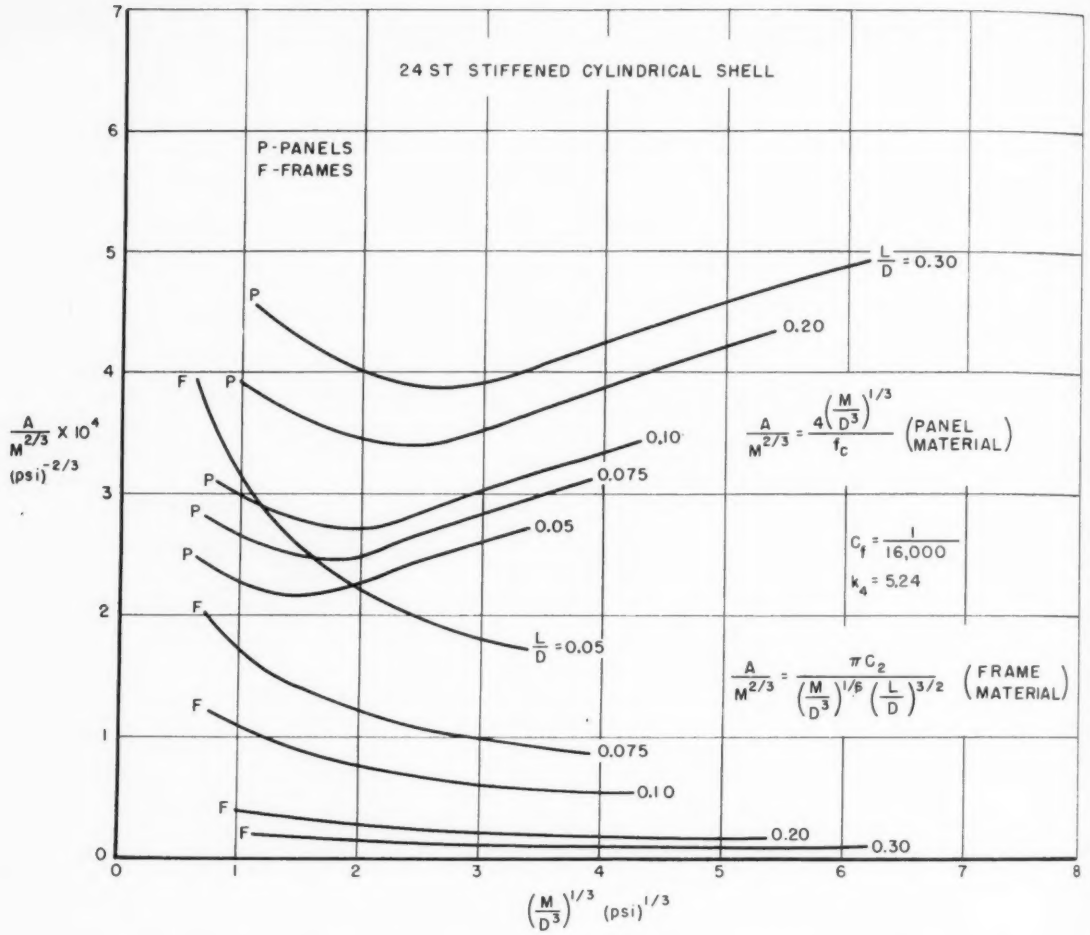

FIG. 3 AREA OF FRAMES AND PANEL PLOTTED SEPARATELY

is calculated from Eq. (14a) for each combination of L/D and M/D^3, and the corresponding value of f_c is read from Fig. 5. Then $A/M^{2/3}$ is evaluated, and the point is plotted on the curve of $A/M^{2/3}$ vs. M/D^3. This procedure is carried out for the values of L/D shown in Fig. 1, the range of values being chosen so as to include the optimum value of frame spacing. The curves of Fig. 1 show directly the variation in total average area for different values of structural index and frame spacing. The cube root of the structural index was used for purposes of contracting the horizontal scale.

It is probable that in the design of a fuselage both the diameter and ultimate moment will be specified, thus fixing the value of M/D^3. It remains then to determine the optimum value of L/D for the specified value of M/D^3. For the case represented in Fig. 1, there appears to be one optimum value of L/D for the entire range of M/D^3—namely, a value of about 0.10.

To determine more accurately the optimum value of L/D, the curves of Fig. 1 are cross-plotted as shown in Fig. 2. The optimum value of L/D is seen to be approximately 0.115 for the range of M/D^3 shown. As the value of L/D is decreased from 0.4 to the optimum value, the curves of Fig. 2 show a gradual decrease in $A/M^{2/3}$. However, any further decrease in L/D results in a sharp rise in $A/M^{2/3}$, indicating that, if nonoptimum frame spacing is used, the greatest weight penalty is likely to be on the side of closer-than-optimum frame spacing.

The range of panel compressive stress f_c for the curves of Fig. 1 is from 10,000 (left end) to 50,000 lbs. per sq.in. (right end). It is interesting to note that the stress corresponding to the optimum M/D^3 for nearly all values of L/D lies in a range of from 26,000 to 32,000 lbs. per sq.in., indicating that the stress for optimum design is considerably lower than the maximum allowable stress for the material used.

Assuming that 50,000 lbs. per sq.in. is the maximum allowable stress for the 24ST panel, the dot-dash portion of the curve for $L/D = 0.10$ (Fig. 1) shows the effect of holding the stress constant at 50,000 lbs. per sq.in. while increasing M/D^3.

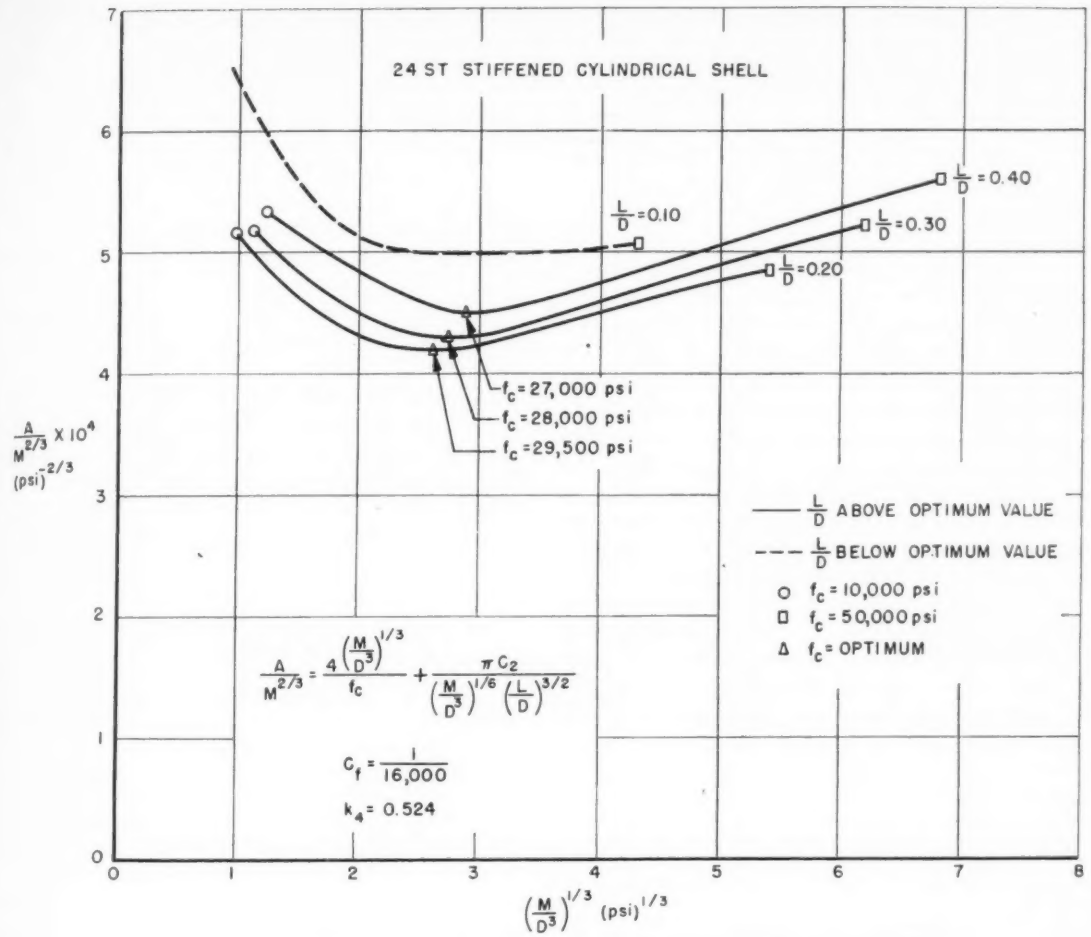

FIG. 4 TOTAL AVERAGE CROSS-SECTIONAL AREA

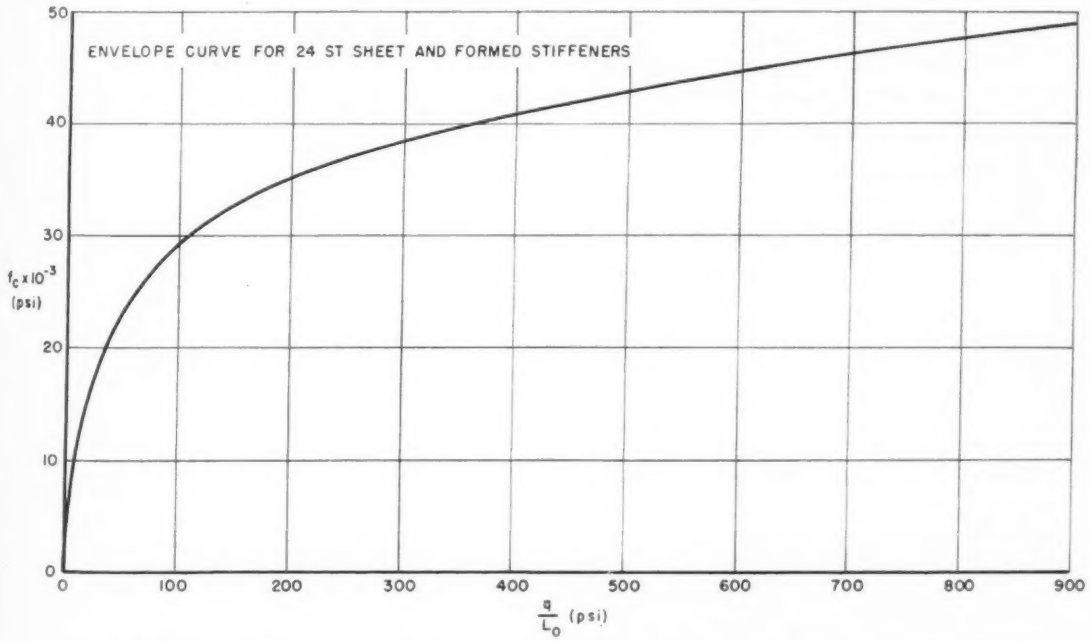

FIG. 5 OPTIMUM (MAXIMUM) STRESS FOR WIDE COLUMNS (SHEET-STIFFENER TYPE)

The first and second terms of Eq. (13) represent, respectively, the amount of panel material and the amount of frame material. Although it is the sum of these terms which must be minimized to give minimum weight, it is desirable to know the relative amount of weight in the panel material and in the frames. Fig. 3 shows the values of $A/M^{2/3}$ plotted separately for the panels and frames. For the near-optimum value of $L/D = 0.10$, it can be seen that the amount of material in the panel is roughly from three to six times that in the frames, depending on the value of M/D^3. However, as the frames are spaced closer than optimum, the ratio of frame material to panel material rises sharply.

Fig. 4 shows the result of using a less efficient frame cross section, the value of I_F/A_F^2 being one-tenth that of the first example. As might be expected, the use of heavier (for a given value of EI) frames causes the optimum spacing to increase over that indicated for the first case, and the total area required is likewise increased. As the same panel construction was used, the values of the first term of Eq. (13) remain the same as for the first example. It was necessary to calculate new values only for the second term of Eq. (13) in order to plot the new set of curves of $A/M^{2/3}$ vs. M/D^3.

Conclusions

As this analysis considers only stresses and proportions, it does not include possible effects of size limitations such as minimum gages, minimum size of stringers and frames, etc. These limitations must, of course, be considered in any actual design, since it is likely that optimum proportions could not be maintained throughout the structure.

The value of C_f chosen for the example is for a circular cross section. A different value would be needed for other shapes.

It should be noted that the frames in the above analysis are designed to prevent general instability when the shell is subjected to pure bending. Other design conditions—such as transverse shear, local loadings, and pressure loads—may be critical for the frames in an actual design.

References

[1] Shanely, F. R., *Principles of Structural Design for Minimum Weight*, Journal of the Aeronautical Sciences, Vol. 16, No. 3, p. 133, March, 1949.

[2] Shanley, F. R., *Simplified Analysis of General Instability of Stiffened Shells in Pure Bending*, Journal of the Aeronautical Sciences, Vol. 16, No. 10, p. 590, October, 1949.

Changes of Address

Since the Post Office Department does not as a rule forward magazines to forwarding addresses it is important that the Institute be notified of changes in address 30 days in advance of publishing date to ensure receipt of every issue of the JOURNAL and REVIEW.

Notices should be sent directly to:

Institute of the Aeronautical Sciences, Inc.
2 East 64th Street, New York 21, New York

Analysis and Design of Stiffened Shear Webs

PAUL H. DENKE*

Douglas Aircraft Company, Inc.

ABSTRACT

A simplified graphical solution of a previously published elastic energy analysis of shear panels is presented. Comparison is made between the results of the analysis and experimental data, and satisfactory agreement is found. A qualitative description of the failure of flat and curved shear panels is given, together with an example of the stress analysis of flat panels. It is concluded that a rational, easily applied, and satisfactorily accurate method has been developed for determining the stress distribution in stiffened shear webs. It is expected that future development, some of which has already taken place, will permit the prediction of ultimate loads not only for thin web beams but also for curved panels typical of wing and fuselage structure.

INTRODUCTION

THE PRESENT PAPER provides a simplified graphical solution of a previously published shear panel analysis.[1] It also gives a comparison with test data and shows some of the applications in stress analysis and design. The previous paper presented a mathematical solution of the problem, but the results were not in a form suitable for practical calculation. This difficulty has been remedied through the discovery of a means of graphical presentation of the important variables.

The experimental comparison is with the N.A.C.A. data on diagonal tension beams.[2] Other experimental studies of the stress distribution in shear panels are available, but time did not permit a critical comparison with all. Agreement with test data is satisfactory in most cases, and such discrepancies as exist can probably be explained on the basis of difficulties involved in the testing technique.

The section on engineering applications is necessarily limited for lack of space, but it is hoped that the discussion given will serve as the basis for further development. It is deemed advisable, at present, to avoid particularizing too much with regard to the estimation of ultimate shear loads, because these depend on the detail design of the panel which varies a great deal among the various air-frame manufacturers. Greatest emphasis is therefore laid on the determination of the stresses existing in various portions of the panel for a given shear load. Whether or not these stresses will cause failure in any of the panel components requires additional correlation between analysis and test results.

Presented at the Structures Session, Annual Summer Meeting, I.A.S., Los Angeles, July 21–22, 1949.

* Structures Engineer.

Historical Survey

The following brief outline is not meant to be exhaustive but is intended only to trace the growth of the principal methods of shear panel analysis so far proposed.

Immediately after the publication of Wagner's classical treatise on the pure tension field,[3] it became clear that the assumption of zero diagonal compressive stress was entirely too conservative, even though it did provide a clear qualitative understanding of the behavior of thin-web beams in shear. In order to avoid this difficulty, three principal methods of analysis or design arose, of which the first was the purely experimental approach whereby components such as spar webs, wing panels, or fuselage panels were tested to destruction. This is the soundest means of determining the strength of a shear panel, provided suitable testing methods are employed. However, it is expensive and time-consuming and is not well adapted to certain purposes, such as the systematic search for optimum panel proportions, because of the large number of variables involved. Moreover, the experimental inaccuracies that inevitably creep in make it advisable to have on hand an analysis method that can serve as the basis for interpreting test results.

The second approach was through the modification of the Wagner equations. This was accomplished most simply by assuming that the principal diagonal compressive stress was not zero but constant and equal to its value at the critical buckling load. Analyses of this type have been developed by Langhaar,[4] Sechler and Dunn,[5] Niles and Newell,[6] Bruhn,[7] and others. These methods also tend to be conservative because many webs buckle at a negligible fraction of their ultimate strengths, and the computed diagonal compressive stresses, assumed constant after buckling, are therefore too small.

A more realistic modification of the Wagner equations was proposed by Kuhn.[8] In his analysis, the fraction of the shear load carried in diagonal tension is assumed to be given by an empirically determined function of the shear stress. The remainder of the load is carried as in a shear-resistant web. Since the various empirical constants have been evaluated to fit experimental results, the analysis can be expected to be reliable in the range covered by the test data, provided suitable testing techniques have been employed. The method is not well adapted to the analysis of heavy webs, since it provides

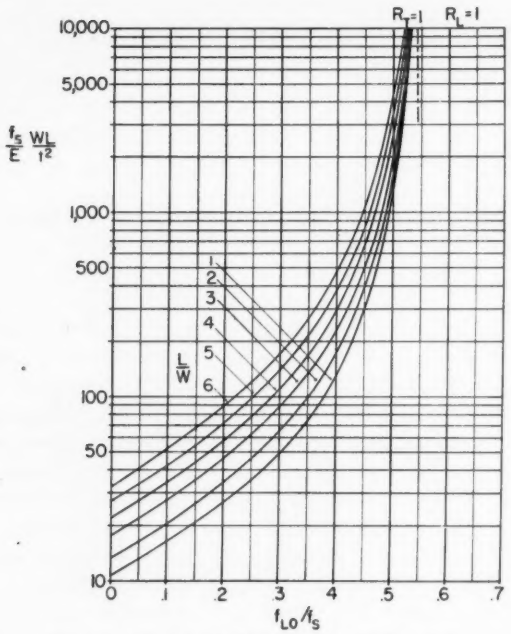

FIG. 1. Average web longitudinal tensile stress.

no means of computing the bending loads imposed on the stiffeners by the buckled sheet.

The third approach to the shear panel problem was simply to make use of established mathematical procedures to determine a reasonably close approximation to the true distribution of stress existing in the web and its stiffening elements. The mathematical instrument usually employed was the principle of virtual displacements, or minimum potential energy, various forms of which were developed by Rayleigh, Ritz, and Galerkin. These methods make use of the well-known expression for the strain energy stored in the buckled web.[10] The first analysis of this type appears to have been that of Kromm and Marguerre,[9] who applied the energy principle to the problem of the infinitely long shear panel subjected to stresses greater than critical, for the two cases of infinite and negligible transverse and longitudinal stiffening. The mathematical basis of the present paper, first presented in 1943, derives from the work of Kromm and Marguerre, although certain points of procedure are quite different. Recently, Levy and others have published analyses employing the energy method or the equivalent differential equations of von Kármán.

Besides the shear panel analysis, the writer has on hand certain unpublished investigations into the behavior of long, flat, and curved panels subjected to combined shear and compression.

Nomenclature

In the following discussion, "longitudinal" and "transverse" refer, respectively, to the long and short dimensions of the panel. Thus, web stiffeners on a thin-web beam are longitudinal stiffeners if they are closer together than the flanges; otherwise, they are transverse. On a fuselage panel the longerons are ordinarily closer together than the frames. The longerons are therefore longitudinal stiffeners, and the frames are transverse stiffeners.

NOTATION

The notation of reference 1 has been revised as follows:

W = panel width free to buckle, in.
L = panel length free to buckle, in.
t = web thickness, in.
f_s = average web shear stress, lbs. per sq.in.
E = effective web modulus of elasticity, lbs. per sq.in.
E_L = effective longitudinal stiffener modulus of elasticity, lbs. per sq.in.
E_T = effective transverse stiffener modulus of elasticity, lbs. per sq.in.
A_L = longitudinal stiffener cross-sectional area, sq.in.
A_T = transverse stiffener cross-sectional area, sq.in.
I_L = longitudinal stiffener moment of inertia, in.^{4}
I_T = transverse stiffener moment of inertia, in.^{4}
R_L = longitudinal stiffening ratio
R_T = transverse stiffening ratio
f_L = web average longitudinal tensile stress, lbs. per sq.in.
f_T = web average transverse tensile stress, lbs. per sq.in.
$\bar{\sigma}_1$ = web average diagonal tensile stress, lbs. per sq.in.
$\bar{\sigma}_2$ = web average diagonal compressive stress, lbs. per sq.in.
W_L = longitudinal stiffener local bending load, lbs. per in.
W_T = transverse stiffener local bending load, lbs. per in.
M_L = longitudinal stiffener local bending moment, in.lbs.
M_T = transverse stiffener local bending moment, in.lbs.
G_s = panel secant shear modulus = f_s/γ_0, lbs. per sq.in.
γ_0 = average panel shear strain

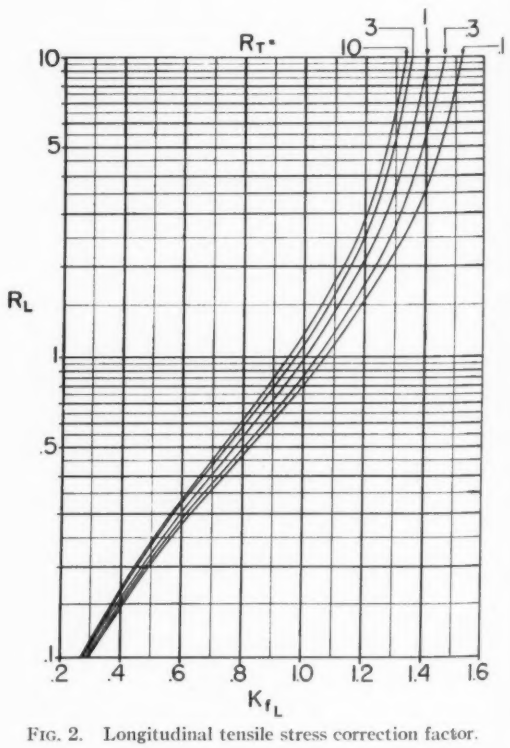

FIG. 2. Longitudinal tensile stress correction factor.

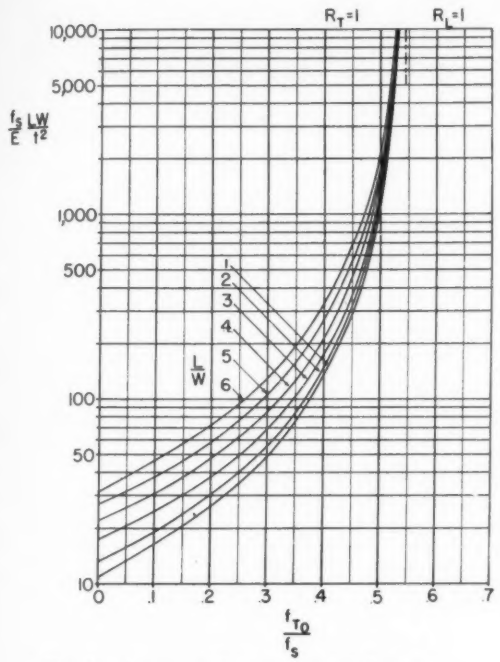

FIG. 3. Average web transverse tensile stress.

A_{L_e} = effective longitudinal stiffener area, sq.in.
ρ = stiffener radius of gyration, in.

GRAPHICAL PRESENTATION OF THE SHEAR PANEL ANALYSIS

The graphical method discussed in this section was developed in collaboration with D. M. Conner, of Douglas Aircraft. Mr. Connor also contributed to the section on the qualitative behavior of shear panels. Acknowledgment is likewise made to S. Noskoff from whose computations the design charts were constructed.

The four basic independent dimensionless groups involved in the analysis are the stress ratio $f_sWL/(Et^2)$, the panel aspect ratio L/W, and the transverse and longitudinal stiffening ratios R_T and R_L. The effect of the quantity R_Q of reference 1, which relates to the bending flexibility of beam flanges, is accounted for in a later paragraph by modifying R_T and R_L in order to avoid introducing a fifth or sixth independent variable. It is therefore necessary to plot the important panel stresses, such as the diagonal tensile stress σ_1, as functions of four independent variables. In general, these are too many to plot, and the mathematics gives no clue as to how matters can be simplified.

However, it is found by calculation that the various panel stresses can be plotted as functions of the stress ratio and the panel aspect ratio for $R_T = 1$ and $R_L = 1$. The effect of the actual panel stiffening can then be accounted for by means of a multiplicative factor K, which is a function of R_T and R_L. In all cases, the ratio of the desired stress to some power of the shear stress is plotted rather than the stress itself, in order that the curves shall have asymptotes (see Figs. 1 to 17). As a result, it is possible to estimate values closely, even when they run off the curve sheet, and this happens only rarely because of the logarithmic scale for $f_sWL/(Et^2)$. The associated K factor is simply the ratio of the asymptotic value of the function for the given stiffening ratios R_T and R_L to its asymptotic value for $R_T = 1$ and $R_L = 1$. An example of the use of these charts is given in a later section.

The following quantities are presented graphically: f_L, f_T, σ_1, W_L, W_T, M_L, M_T, and G_e. Most of the important panel loads and stresses are thus represented, and the remaining ones can be obtained by straightforward calculation. It was not found possible to plot the depth, length, and angle of the web buckles in simple fashion, but these are not ordinarily required in analysis. However, further investigation may disclose a means of plotting these quantities also.

The charts are based on a value of Poisson's ratio equal to 0.33.

It has been found that, by comparison with calculations made from the original analysis, the panel stresses obtained graphically are given to slide-rule accuracy. The charts therefore comprise a solution of the mathematical analysis complete and accurate enough for engineering purposes.

COMPARISON WITH TEST DATA

The stiffener stresses for the beams of series I, II, and III of reference 2 were computed and compared with

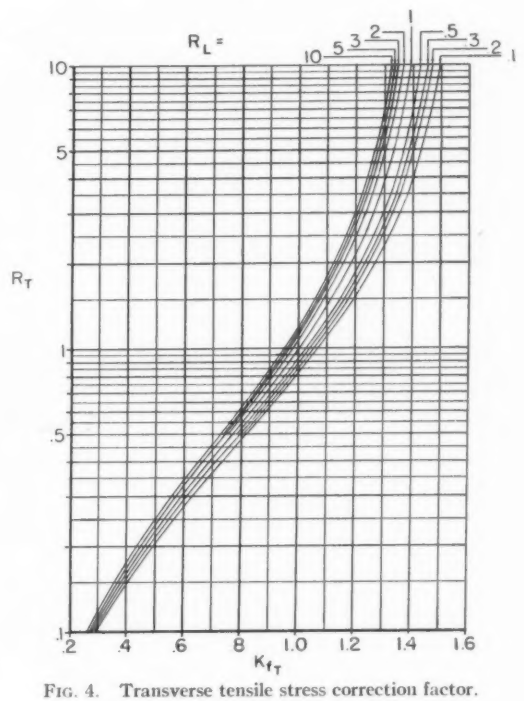

FIG. 4. Transverse tensile stress correction factor.

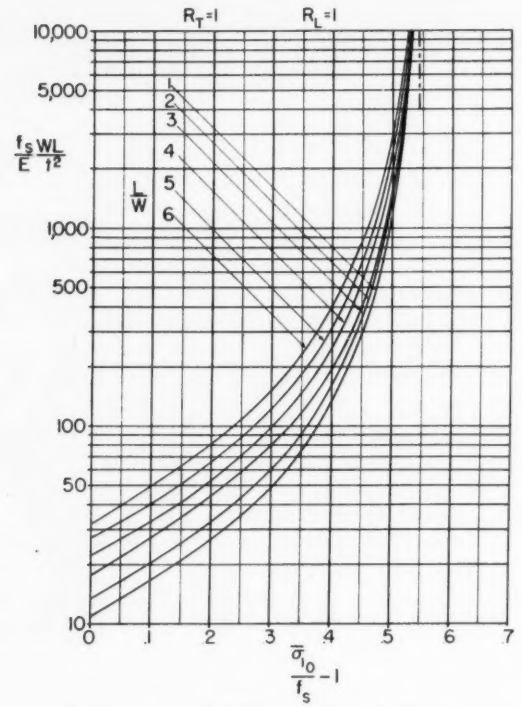

FIG. 5. Average web diagonal tensile stress.

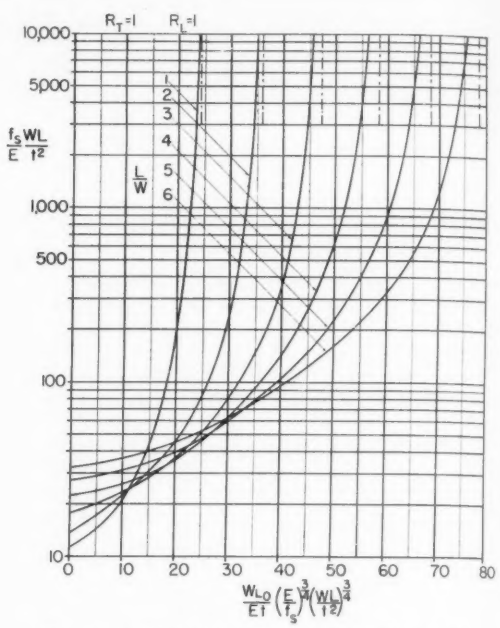

FIG. 7. Longitudinal stiffener local bending load.

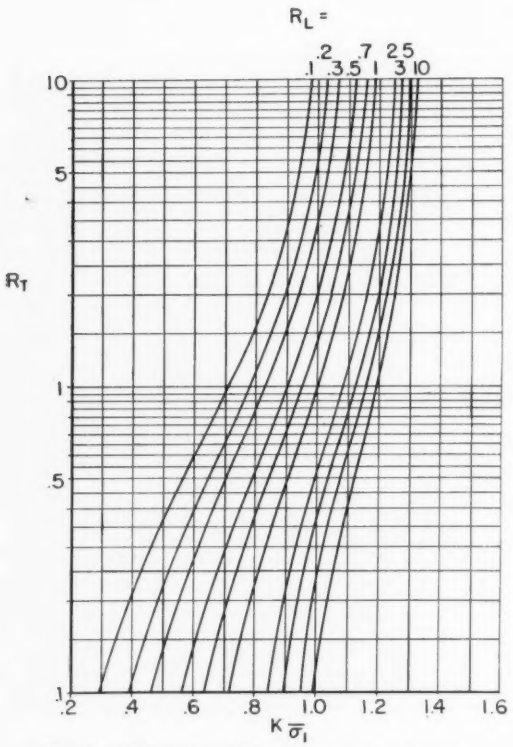

FIG. 6. Diagonal tensile stress correction factor.

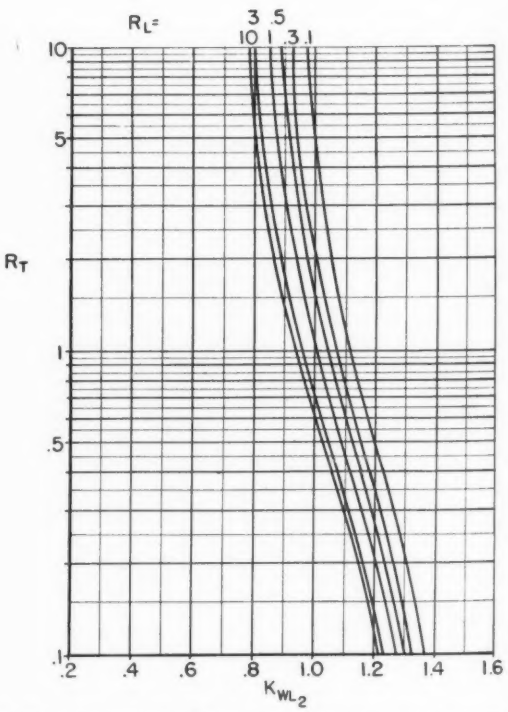

FIG. 8. Longitudinal stiffener local bending load correction factor.

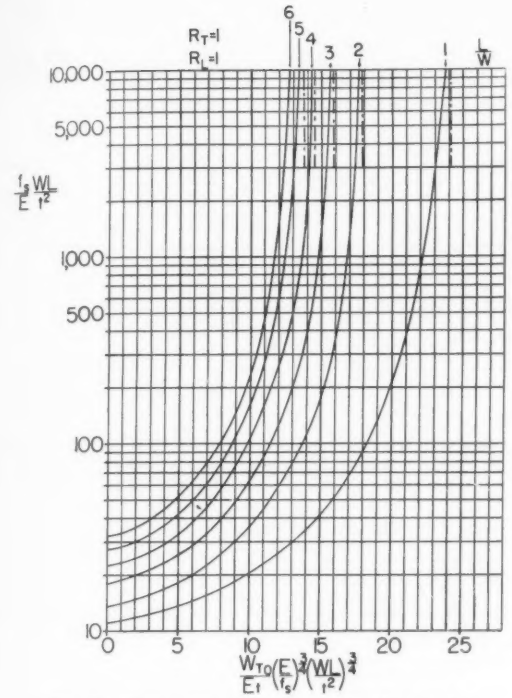

FIG. 9. Transverse stiffener local bending load.

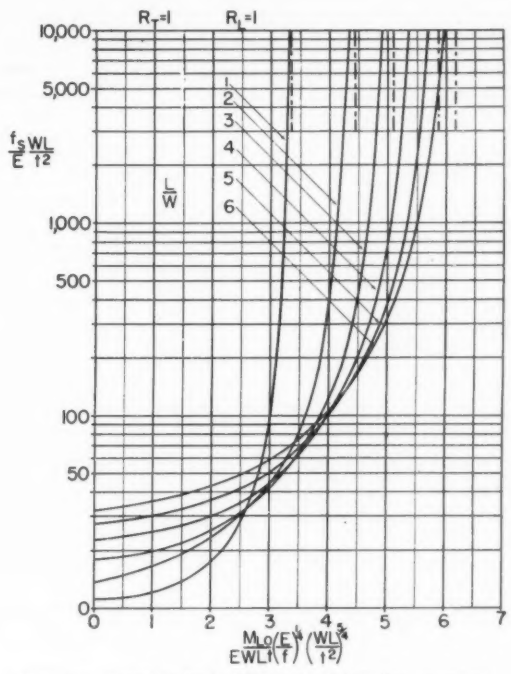

FIG. 11. Longitudinal stiffener local bending moment.

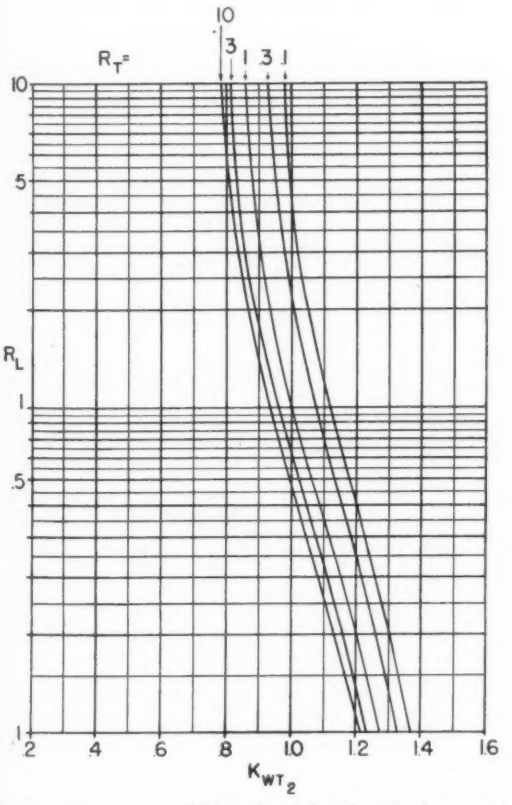

FIG. 10. Transverse stiffener local bending load correction factor.

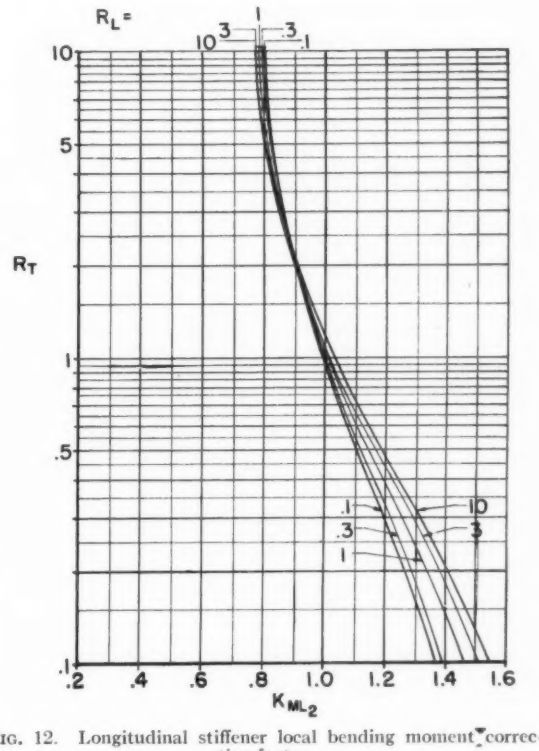

FIG. 12. Longitudinal stiffener local bending moment correction factor.

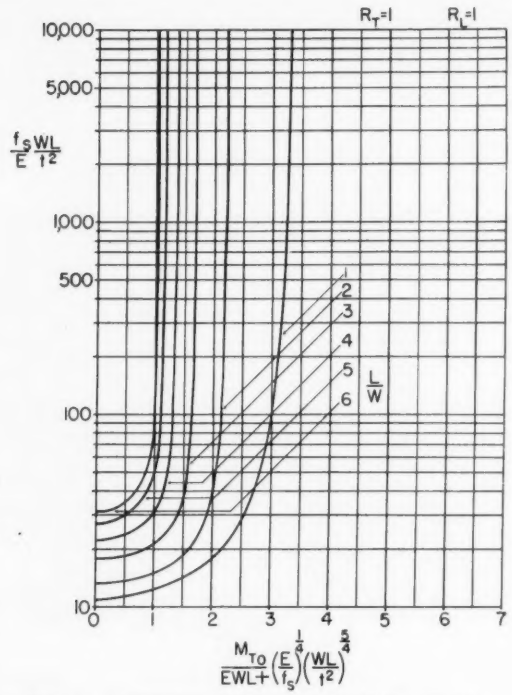

FIG. 13. Transverse stiffener local bending moment.

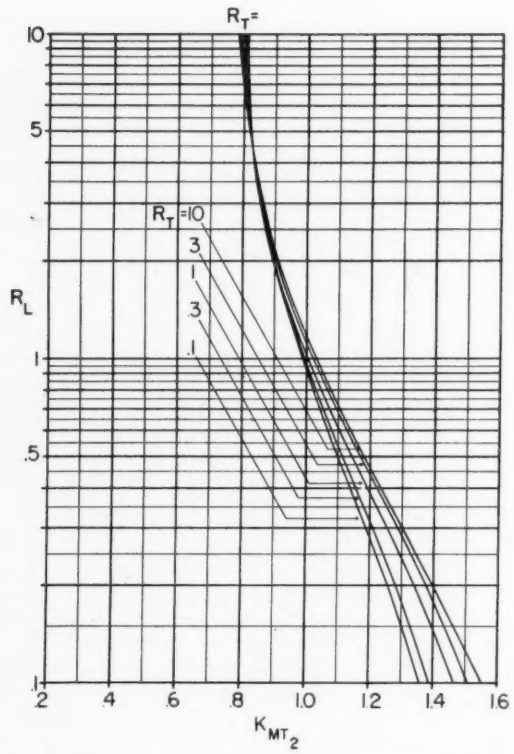

FIG. 14. Transverse stiffener local bending moment correction factor.

the test results, as shown in Figs. 18, 19, and 20. The method of computation is similar to the example given in a later paragraph. However, in the case of beams having stiffeners on one side of the sheet only (these are denoted by "S" in the beam code number), it was necessary to account for the fact that test stresses were measured only on the leg of the stiffener attached to the sheet, so that bending stresses were not eliminated. The correction was made according to the simple theory of flexure.

It should be noted that the computed stiffener stress is due only to the axial load introduced by the buckled web plus the bending due to the fact that the web is eccentric with respect to the stiffener. However, the range of test scatter indicates that extraneous stresses have affected the measurements. These additional stresses may be due to stiffener column action, stiffener torsional instability, or lateral loads imposed on the stiffener by the buckled web. However, the method of the present paper indicates that the web wrinkles produce small bending moments in the stiffener. If it be assumed that these moments are resisted only by the leg of the stiffener attached to the web, it is still only possible to account for a portion of the observed scatter.

In an effort to eliminate the extraneous stresses, the strain gage readings were averaged up and down the length of the stiffener.[2] But it does not follow that the resulting average would represent the sum of the compressive plus eccentric bending stress, as supposed. Thus, it is not surprising that the largest discrepancies between computed and test results occur for beams with single web stiffeners. (Beams having stiffeners on both sides of the sheet are denoted by "D" in the code number.)

It should be kept in mind in examining Figs. 18, 19, and 20 that no empirically determined functions have entered the analysis at this point, except the experimentally determined variation of effective web modulus with shear stress discussed later.

Analysis and Design

Failure of Flat and Curved Shear Panels

This section is a qualitative description of the behavior of both flat and curved shear panels at failure. It is believed that the present analysis may be applied, with suitable modifications, to curved panels in any case where the stiffening elements are sufficiently close together so that the sheet bounded by them is, for all practical purposes, flat. For example, a fuselage panel having a radius of curvature of 60 in., with longerons 6 in. on center, should come under this classification.

Web Failure

Shear panel webs normally fail through diagonal tension. Although basically simple, the mechanism of

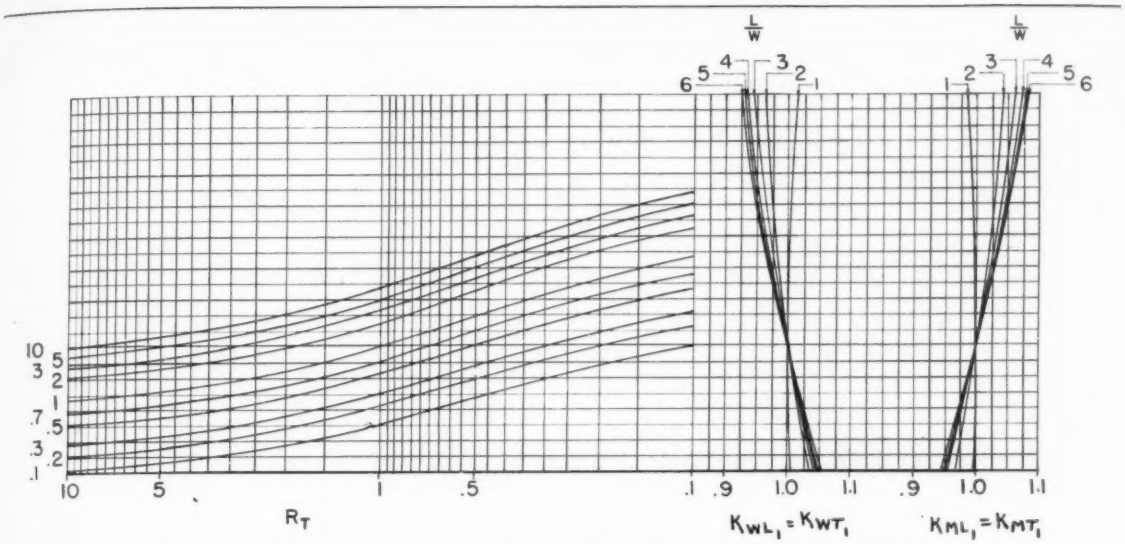

FIG. 15. Longitudinal and transverse local bending load and moment correction factors.

diagonal tension is complicated by the following factors: (1) The diagonal tensile stress is not uniform but, in the ideal web, tends to be maximum at the center and minimum at the edges. (2) The effect of wrinkling is to introduce bending stresses that add to the diagonal tension. These stresses likewise vary throughout the web and, in the ideal case, tend to a maximum at the center. (3) In the actual case, the riveted attachment of web to stiffeners produces stress concentrations that cause failure to start at the panel edges. Fig. 21 shows a diagonal tension failure.

Stiffener Failure

The term "stiffener" is here used in a general sense and may denote the stiffeners or flanges of a tension field beam, the stringers or ribs of a wing panel, or the longerons or frames of a fuselage panel. The following types of loads contribute to stiffener failure:

(*1*) *Axial Loads.*—In the case of a beam, the longitudinal tensile stress f_L is transmitted into the stiffener,

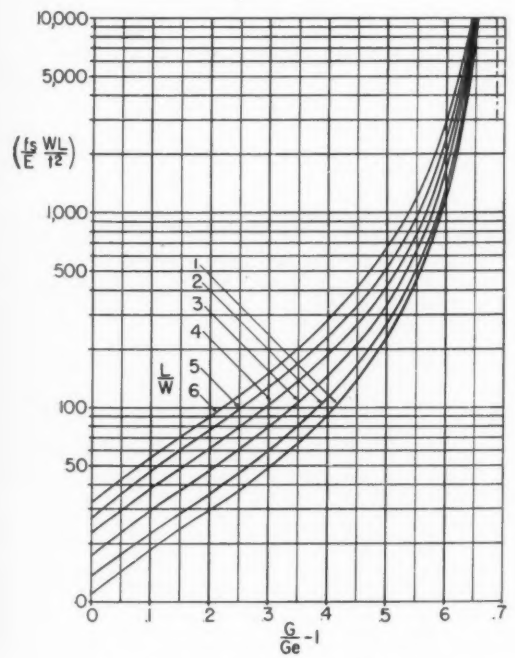

FIG. 16. Panel secant shear modulus.

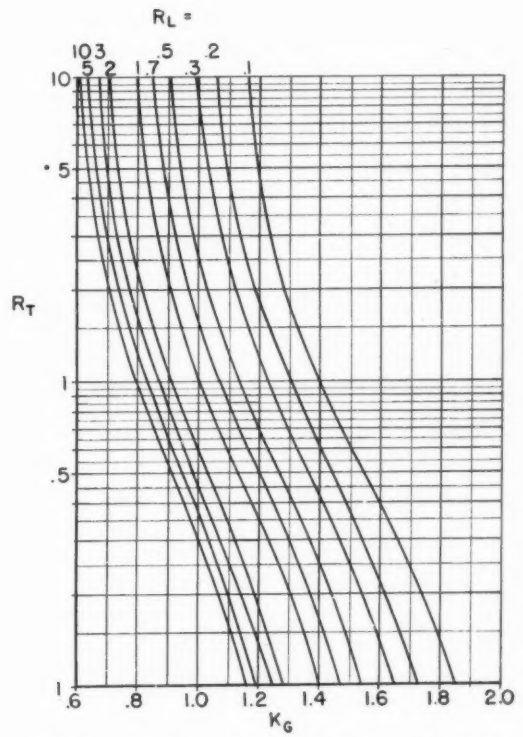

FIG. 17. Panel secant shear modulus correction factor.

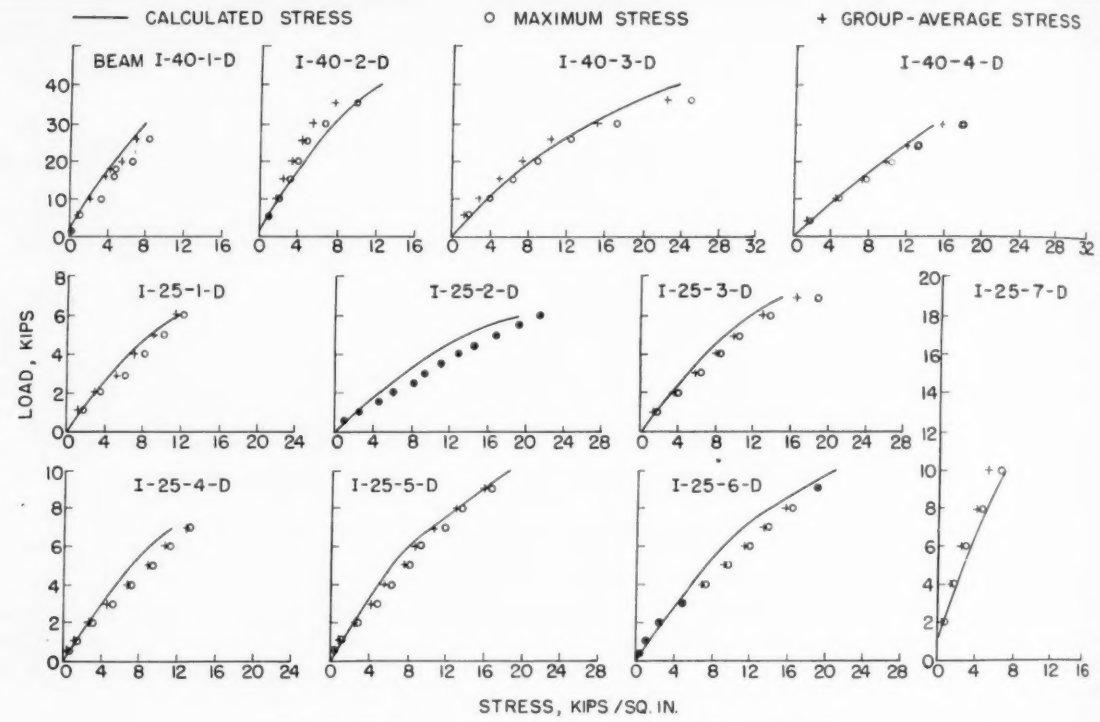

FIG. 18. Stiffener stress vs. shear load. N.A.C.A. beams series I.

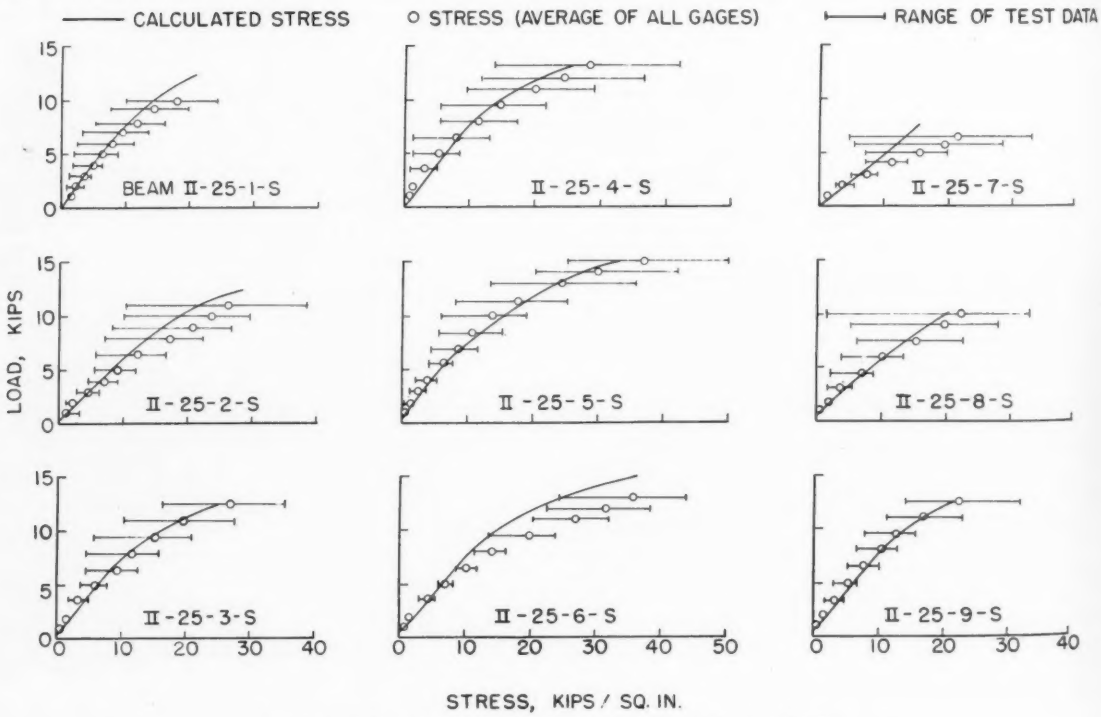

FIG. 19. Stiffener stress vs. shear load. N.A.C.A. beams series II.

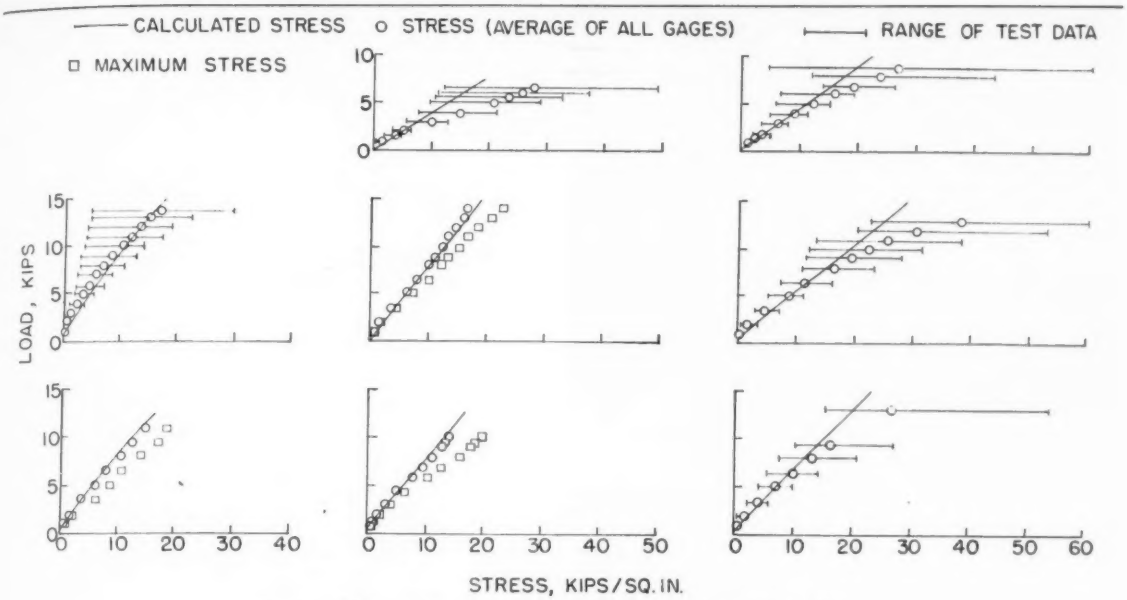

FIG. 20. Stiffener stress vs. shear load. N.A.C.A. beams series III.

producing the compression load P_L, as shown in Fig. 22. A stiffener that failed locally in axial compression is shown in Fig. 23. The transverse tensile stress f_T produces similar loads P_T in the flanges. In the case of a fuselage panel, the transverse tensile stress f_T has an inward component because of curvature, as a result of which radial loads per inch W_G are produced on the stringers (see Figs. 24 and 25), which in turn introduce compressive loads P_f in the frame.

(2) *Eccentric Bending Load.*—Besides producing compressive stress in the stiffener, the load P_L mentioned in reference 1 also introduces bending if the centroid of the stiffener does not lie on the skin line. Thus, in Fig. 26, the stiffener bending moment is $P_L z$.

(3) *Column Action and Torsional Instability.*—Beam stiffeners may have a tendency to fail as columns under the action of the stiffener axial loads. However, there are certain characteristics of shear panel behavior tending to minimize the likelihood of column failure, as is demonstrated by the following argument, which is thought to be valid in the case where the stiffeners are much closer together than the flanges.

Consider the curved stiffener shown in Fig. 27. The curvature may either be built in or be due to the bending effect of the various bending loads, discussed elsewhere, which are imposed upon the stiffener. The curve AB shown in the figure represents the mean deflection of the wrinkled skin, assumed to be the same as the deflection of the stiffener. Assuming that the length of the stiffener is sufficient so that the skin will act as a membrane over the distance AB, it follows that there must be certain distributed loads W_c, as shown, such

FIG. 21. Web diagonal tension failure.

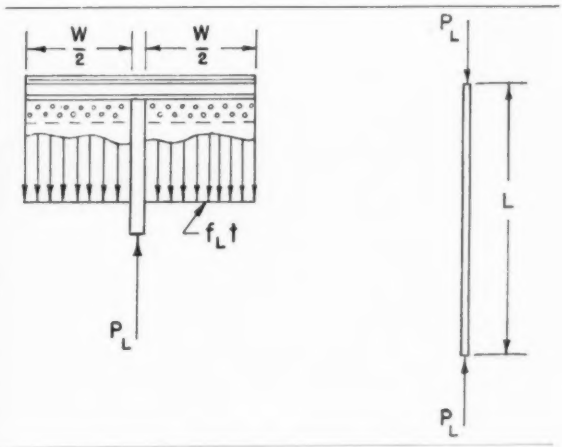

FIG. 22. Stiffener axial load.

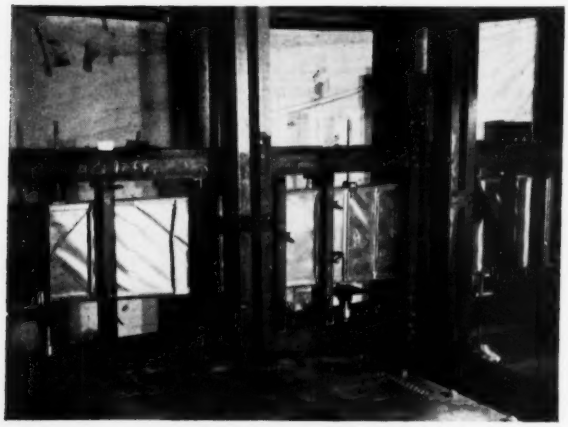

FIG. 23. Stiffener axial load failure.

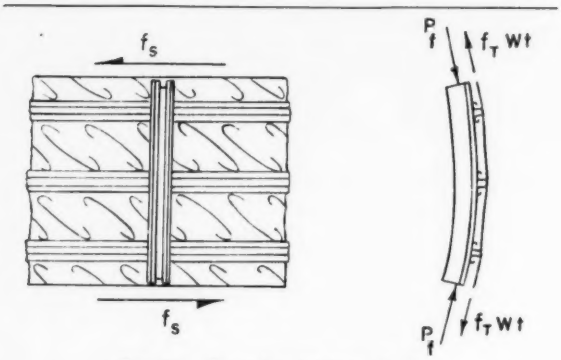

FIG. 24. Curved panel frame loads.

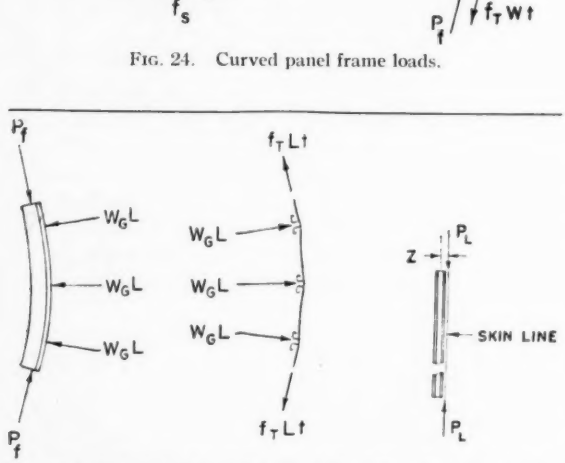

FIG. 25 (*left*). Curved panel frame loads. FIG. 26 (*right*). Stiffener eccentric bending moment.

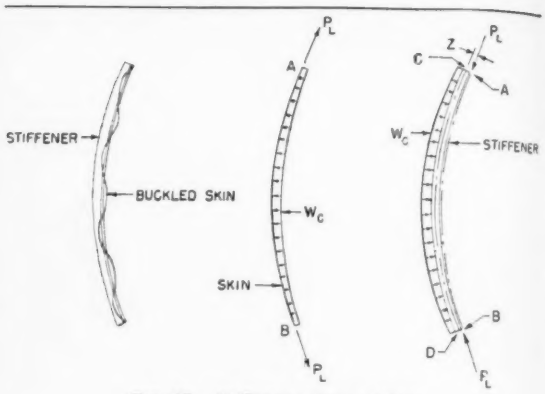

FIG. 27. Stiffener column action.

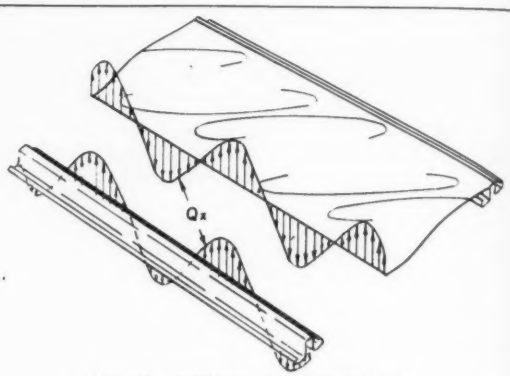

FIG. 28. Stiffener local bending loads.

that the combined bending moment of W_c and P_L about any point of AB is zero. Furthermore, the resultant at any point must be tangent to AB and equal to P_L. In the free-body diagram of the stiffener, CD is the centroidal axis. In this diagram also, the resultant load at any section of the stiffener is tangent to AB and equal to P_L. Consequently the moment about any point of CD due to the load P_L is equal to, but no greater than, $P_L z$. The column effect is therefore negligible.

In the case where the stiffeners are far enough apart to invalidate partially the above argument, because the web no longer bends with the stiffener near the panel center, the transverse tensile stress f_T begins to acquire a component tending to oppose lateral deflection so that the possibility of column failure is again inhibited.

The effect of the tension field in partially supporting the stiffener was first pointed out by Wagner,[3] who accounted for it by using a reduced column length in computing the strength of the upright.

Open section stiffeners on beam webs show a tendency to fail by torsional instability. Whether or not this type of failure is opposed by action of the web is not clear.

(*4*) *Stiffener Secondary Bending.*—The longitudinal and transverse tensile stresses f_L and f_T produce secondary bending stresses in the flanges and end stiffeners of beams. These stresses are of particular importance in the flanges of beams having widely spaced stiffeners.

(*5*) *Local Bending Loads.*—This is the term here used to denote the bending loads imposed on the stringer by the buckling of the web. The effect is illustrated in Fig. 28. The loads per inch Q_z produced on the stiffener are localized and sinusoidal in character. The maxima occur at points where the wrinkle crests intersect the

stiffener. The bending moments produced in the stiffener are in phase with the load. The loading shown in Fig. 28 is due to one panel only. If there are two adjacent panels, then the total stiffener load is the sum of the loads contributed by both panels. The resulting load on the stiffener is designated W_L. The stiffener moments are larger if the two loads are in phase than if they are out of phase. In particular, if the two adjacent panels are identical and equally stressed, then the stiffener moments are maximum if the loads are in phase and identically zero if they are 180° out of phase. Fig. 29 shows a stiffener failure apparently due largely to local bending moments induced by the buckled web.

(6) *General Bending Loads.*—These are the loads imposed on the longerons or curved fuselage panels as a result of the curvature of the tension field and are, in fact, identical with the loads W_G shown in Fig. 25. Reactions are provided by the frames as shown in Fig. 30. The stringer is thus a uniformly loaded continuous beam, with the maximum bending moments occurring at the frames. Fig. 31 shows a curved panel in which the longitudinal stiffeners failed under the action of the general bending load.

(7) *Torsional Loads.*—The local loads imposed on a stringer by two adjacent panels may combine to produce torsion instead of bending. This effect is particularly pronounced where the panels are identical and equally stressed, provided they buckle 180° out of phase as in Fig. 32. Fig. 32 also shows the resulting torsional loads on the stiffener.

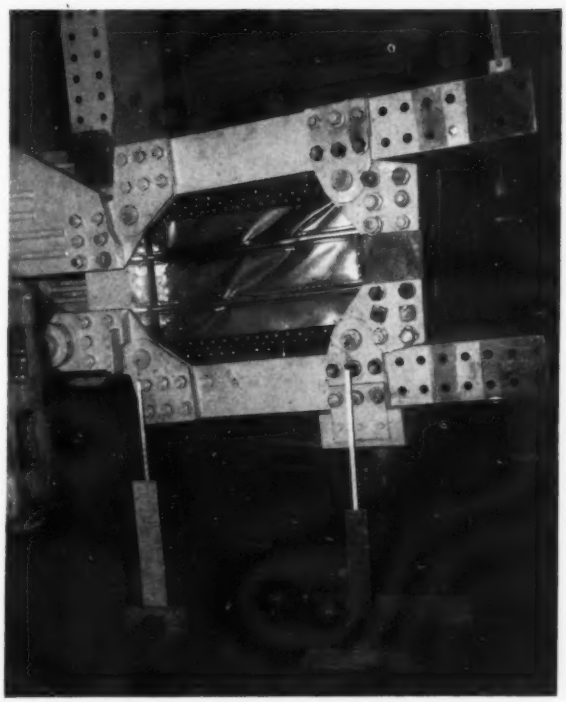

FIG. 29. Stiffener local bending failure.

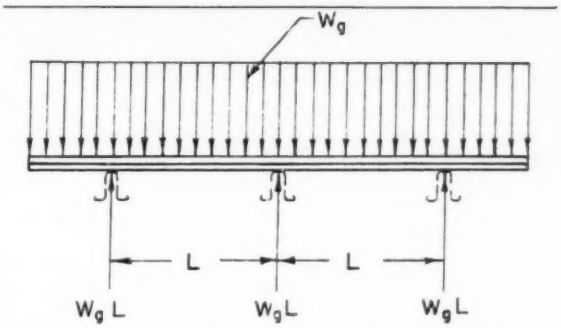

FIG. 30. Curved panel stiffener general bending loads.

Rivet Failure

The following loads contribute to rivet failure:

(1) *Shear Loads.*—The total shear on a transverse riveted seam or attachment is found by vectorially adding the stresses f_s and f_L. On a longitudinal seam or attachment, the total stress is the vector sum of f_s and f_T. In the panel shown in Fig. 33, the riveted attachment along the lower (transverse) edge failed in shear.

(2) *Tensile Loads.*—The same loads that produce stringer bending also tend to cause failure of skin-to-stringer rivets in tension (see Fig. 34). Actually, the general load W_G always acts radially inward; consequently, it always reduces the rivet tensile load. It is the local load W_L which is primarily responsible for panel failure by rivet tension. The total rivet load is equal to $(W_L - W_G)S_R$. However, it should be noted that, in curved panel tests, the panel frequently flattens out, thus reducing the load W_G and causing rivet tensile failure to occur under the action of W_L. Fig. 35 shows a rivet tension failure.

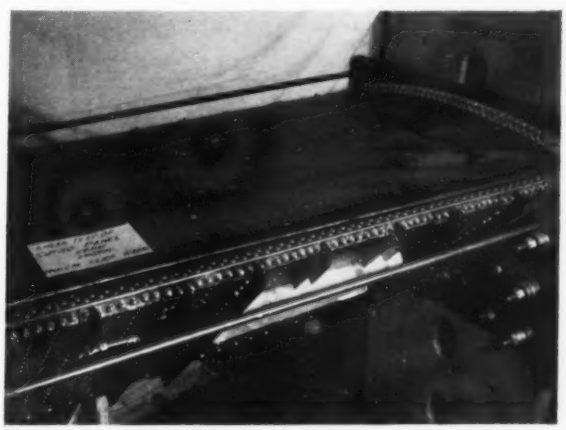

FIG. 31. Curved panel stiffener general bending failure.

Stress Computation

It is believed that the various effects discussed above can be adequately evaluated on the basis of the present method. No example is given in what follows of the computation of loads in curved panels, but the flat panel

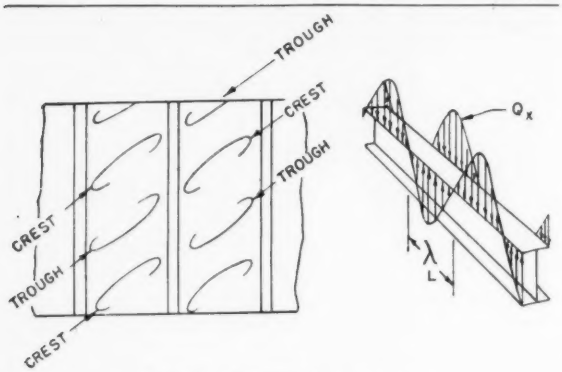

FIG. 32. Stiffener torsion loads.

FIG. 33. Rivet shear failure.

example should serve to indicate the type of calculation required in curved panel analysis.

Analysis of Flat Panels

In flat panel analysis, the basic geometric data and loading are determined, values of the panel stresses are read from the charts for $R_L = 1$ and $R_T = 1$, these readings are multiplied by the correction factors corresponding to the true stiffening ratios, and the final stresses and loads are obtained by simple calculation.

Panel Dimensions

Fig. 36 shows the basic geometric data. The panel length L is the length of sheet free to buckle. Similarly, W is the buckled width. The longer dimension is always denoted L. In the case of single web stiffeners with a single row of rivets, the web buckles all the way to the rivet line, and W (or L) is measured from rivet row to rivet row. If the web stiffeners are double, the strip of skin between stiffeners should be considered unbuckled, and W is measured to the stiffener edges.

Shear Stress

In the case of a beam, the shear stress is taken as the total load divided by the distance between the centroids of the upper and lower riveted attachments times the sheet thickness.

Effective Modulus

Fig. 37 gives the effective web modulus of elasticity as a function of the shear stress for 24STAL and 75STAL materials. This empirical relation is based on load-deflection data derived from a large number of shear panel tests made at Douglas Aircraft. The use of these curves to account for panel behavior above the elastic limit of the web is justified by the agreement found in the previous section between test and analysis for the two kinds of material.

It is logical also to use some sort of effective modulus for the stiffening elements, but this would require a solution by successive approximations, since stiffener stresses are not known in advance. However, such a procedure can normally be avoided, since stiffeners, being in compression, are usually not so highly stressed as webs.

Stiffening Ratios

Basically, the stiffening ratios are given by

$$R_L = \frac{A_L}{Wt}\frac{E_L}{E}, \qquad R_T = \frac{A_T}{Lt}\frac{E_T}{E}$$

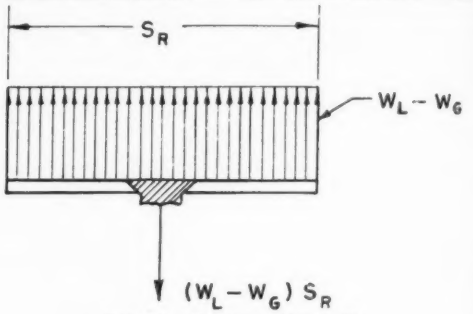

FIG. 34. Rivet tension loads.

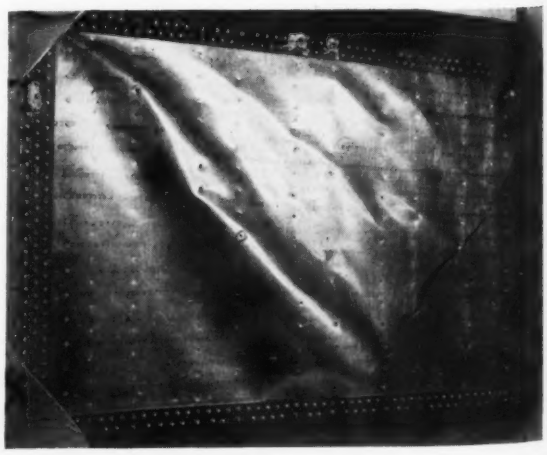

FIG. 35. Rivet tension failure.

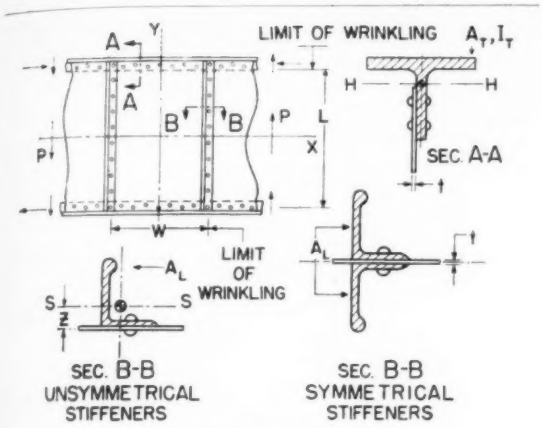

FIG. 36. Basic geometric data.

In these expressions, A_L is the amount of longitudinal stiffening associated with the area Wt of a transverse web section. Similarly, A_T is the transverse stiffener area associated with the area Lt of a longitudinal web section.

In the case of an interior panel of a beam (e.g., not the end panel), A_L is the area of one stiffener where there are single stiffeners or is the area of two stiffeners where there is double stiffening (see section BB, Fig. 36). A_T is the total area of both flanges.

In determining the longitudinal stiffening ratio for a beam, the bending flexibility of the flanges should be accounted for. This may be done by modifying the expression for R_L as follows:

$$R_L = \frac{(A_L/Wt)(E_L/E)}{\frac{W^3 A_L}{720L}\left(\frac{1}{I_{TU}} + \frac{1}{I_{TL}}\right)\frac{E_L}{E_T} + 1}$$

where I_{TU} and I_{TL} are the moments of inertia of the upper and lower flanges. This equation was derived by finding the area of an effective stiffener which, when combined with infinitely rigid flanges, gives the same average strain as the actual stiffener-flange combination under the same loading.

Where there are stiffeners on one side of the sheet only, the longitudinal stiffener area should be replaced by an effective value given by

$$A_{Le} = \frac{A_L}{[1 + (Z/\rho)^2]}$$

where Z is the distance from the stiffener centroid to the centerline of the web (see Fig. 36). This expression is due to Kuhn.[2] A similar correction may also be applied to transverse stiffeners. Where the stiffeners are double, no correction of this kind is required, but A_L should include the area of the strip of web between stiffeners.

Note that the value of E used in the stiffening ratios should be the effective value of the web modulus.

Example of Flat Panel Analysis

Determine the stress distribution in the beam shown schematically in Fig. 38. The design moment is 13,500 in.lbs. (compression on top), and the design shear is 1,225 lbs. per in.

$$f_s = 1{,}225/0.051 = 24{,}000 \text{ lbs. per sq.in.}$$

From Fig. 37,

$$E/E_0 = 0.487$$

$$E = 0.487 \times 10.6 \times 10^6 = 5.16 \times 10^6 \text{ lbs. per sq.in.}$$

$$\frac{f_s}{E}\frac{W_L}{t^2} = \frac{24{,}000 \times 8 \times 13.5}{5.16 \times 10^6 \times 0.051^2} = 193.0$$

$$L/W = 13.5/8 = 1.69$$

$$A_{Le} = \frac{0.127}{1 + (0.423/0.363)^2} = 0.0538 \text{ sq.in.}$$

$$\frac{A_{Le}E_L}{WtE} = \frac{0.538 \times 10.6 \times 10^6}{8 \times 0.051 \times 5.16 \times 10^6} = 0.271$$

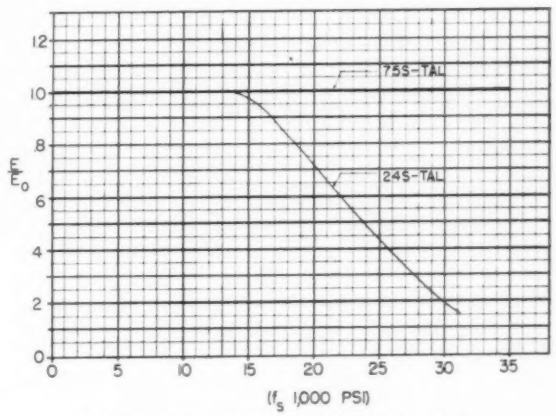

FIG. 37. Effective web modulus of elasticity.

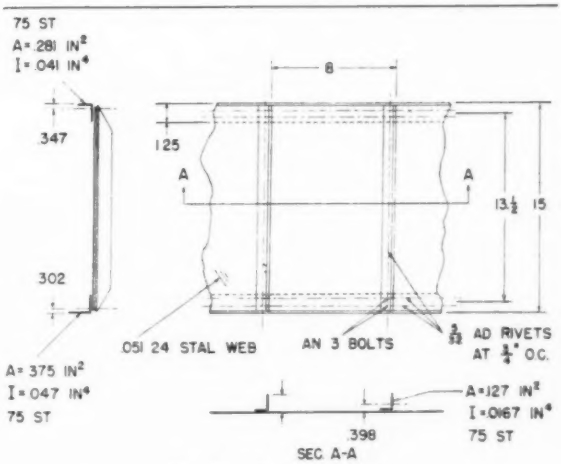

FIG. 38. Beam example.

$$\frac{W^3 A_{Le}}{720L}\left(\frac{1}{I_{TU}}+\frac{1}{I_{TL}}\right)\frac{E_L}{E_T}+1=\frac{8^3\times 0.0538}{720\times 13.5}\times\left(\frac{1}{0.041}+\frac{1}{0.047}\right)+1=1.130$$

$$R_L = 0.271/1.130 = 0.240$$

$$R_T = \frac{(0.281+0.375)\times 10.6\times 10^6}{13.5\times 0.051\times 5.16\times 16\times 10^6} = 1.960$$

(See Table 1.)

TABLE 1

Type of Stress	Uncorrected Value	K	Corrected Value
$(\bar{\sigma}_1/f_s)-1$	0.417	0.910	0.380
L/f_s	0.415	0.515	0.214
T/f_s	0.422	1.235	0.522
$\frac{W_L}{Et}\left(\frac{E}{f_s}\right)^{3/4}\left(\frac{WL}{t^2}\right)^{3/4}$	26.5	1.015×1.025	27.6
$\frac{M_L}{EWLt}\left(\frac{E}{f_s}\right)^{1/4}\left(\frac{WL}{t^2}\right)^{5/4}$	3.63	0.985×0.905	3.24

Web

$\bar{\sigma}_1 = (0.380+1)24{,}000 = 33{,}100$ lbs. per sq.in.

This figure should be multiplied by a factor to account for stress concentrations at the riveted attachment. A suggested correction is

$$\bar{\sigma}_{1_{design}} = \bar{\sigma}_1\left(\frac{S_R}{S_R-\sqrt{2}D}\right)K$$

where S_R = rivet spacing, D = rivet diameter, and K = concentration factor $\cong 1.1$ for round-head rivets.

Stiffeners

$P_L = f_{L_1} t_w W = 2{,}100$ lbs.

$M_L = 3.24\, EWLt/(E/f_s)^{1/4}(WL/t^2)^{5/4} = 40.6$ in.lb.

$E/f_s = 5.16\times 10^6/24{,}000 = 215$

$WL/t^2 = 8\times 13.5/(0.051)^2 = 41{,}500$

$A_L = 127$ sq.in., $\quad I_L = 0.0167$ in.^{4}

$Z = 0.398 + (0.051/2) = 0.423$ in.

$C = 0.398$ or 0.602

Stress in leg attached to web:

$$f_b = -\frac{2{,}100}{0.127}\pm\frac{40.6\times 0.398}{0.0167}-\frac{2{,}100\times 0.423\times 0.398}{0.0167}$$
$$= -38{,}710 \text{ lbs. per sq.in. (compression)}$$

Caps

Compressive load due to transverse stress:

$P_T = f_t tL = 8{,}630$ lbs.

$P_T/cap = 8{,}630/2 = 4{,}315$ lbs.

Load due to design moment:

$P_M = 13{,}500/14.351 = 940$ lbs. (compression top cap)

The upper cap is critical.

Compressive stress:

$f_c = (4.315+940)/0.281 = 18{,}700$ lbs. per sq.in.

Bending stress at stiffener:

$f_b = F_L W^2 C/12I$

$F_L = 24{,}000\times 0.214\times 0.051 = 262$ lbs. per in.

$f_b = \frac{262\ (8)^2\ 0.903}{12\times 0.041} = 30{,}800$ lbs. per sq.in. (compression)

$f_{max.} = 18{,}700 + 30{,}800 = 49{,}500$ lbs. per sq.in. (compression)

Web-Stiffener Attachment

$W_L = 27.6Et/(E/f_s)^{3}/_{4}(WL/t^2)^{3}/_{4} = 44.2$ lbs. per in.

tension/rivet $= 44.2\times 0.75 = 33.2$ lbs. per rivet

Web-Cap Attachment

$f_L = 0.214\times 24{,}000 = 5{,}140$ lbs. per sq.in.

$f_{RT} = \sqrt{f_s^2+f_L^2} = 24{,}600$ lbs. per sq.in.

$F_{RT} = 24{,}600\times 0.051 = 1{,}252$ lbs. per in.

rivet load $= (1{,}252/2)\,0.75 = 470$ lbs. per rivet

Stiffener-Cap Attachment

$P_L = 2{,}100$ lbs.

If the load P_L is assumed to be transmitted entirely through the two bolts, then the load per bolt is 1,050 lbs. However, it appears to be good practice to consider that one of the stiffener rivets just below the cap helps to transmit the load, on the assumption that a small piece of web in the corner of the panel acts as a gusset.

Note in the above example that the depth of panel, L, was taken as the distance between the centroids of the upper and lower riveted attachments, assuming that these marked the limits of web buckling. In Table 1 the correction factor for W_L is given by $K_{WL} = K_{WL_1}K_{WL_2}$.

CONCLUSION

A graphical method of applying the previously developed shear panel equations has been presented, and a comparison has been made between experimentally determined stiffener stresses and chart values. Reasonable agreement was found, and, where discrepancies appeared, it was possible that extraneous influences may have affected the test data. Since all of the aspects of panel behavior treated by the present method are part of a unified mathematical structure, it seems reasonable to suppose that verification of the predicted stiffener stress is at least a partial verification of the remainder of the analysis.

There is need for additional experimental investigation with regard to both the distribution of stress and the determination of allowable loads for the various panel components. In particular, the bending loads produced on the stiffener by the buckled sheet should be measured and compared with analysis values. In this connection, it should be mentioned that the charts for W_L and M_L give loads acting at the center of the stiffener, assuming conservatively that the crest of a web buckle intersects the stiffener at its midpoint. The same is true for the quantities W_T and M_T.

Besides the loads W_L and W_T, there are torsional stresses in the web itself, and these may have some effect on the stiffener. No explicit expression was given in reference 1 for web torsion, although one could be derived, and the energy of warping was accounted for in the analysis.

Although the loads W_L and M_L were small in the example analysis, their importance should not be discounted, because they increase rapidly with sheet thickness, for constant panel dimensions and shear stress.

It is concluded that a practical method of shear panel analysis has been developed. This method has a rational mathematical basis, is readily and easily applicable to engineering problems, and is capable of giving satisfactorily accurate results through the plastic range to failure of the panel. Although only the stress analysis of panels has actually been demonstrated, it is anticipated that additional investigation and refinement will establish the validity of the method as a means of predicting ultimate loads. It is further expected that the method will prove to be applicable not only to thin web beams but also to curved wing and fuselage panels. Some degree of success has, in fact, already been achieved in predicting ultimate loads for curved fuselage panels, although the results were not in a form suitable for publication at the time of preparation of the paper.

References

[1] Denke, P. H., *Strain Energy Analysis of Incomplete Tension Field Web-Stiffener Combinations*, Journal of the Aeronautical Sciences, Vol. 11 No. 1, pp. 25–40, January, 1944.

[2] Kuhn, P., and Peterson, J. P., *Strength Analysis of Beam Webs*, N.A.C.A. T.N. No. 1364, 1947.

[3] Wagner, H., *Flat Sheet Metal Girders with Very Thin Metal Webs*, N.A.C.A. T.M. Nos. 604, 605, and 606, 1931.

[4] Langhaar, H. L., *Theoretical and Experimental Investigations of Thin-Webbed, Plate Girder Beams*, Trans. A.S.M.E., Vol. 65, pp. 799–802, October, 1943.

[5] Sechler, E. E., and Dunn, L. G., *Airplane Structural Analysis and Design*, pp. 234–258; John Wiley & Sons, Inc., New York, 1942.

[6] Niles, A. S., and Newell, J. S., *Airplane Structures*, 3rd Ed., Vol. II, pp. 156–178; John Wiley & Sons, Inc., New York, 1947.

[7] Bruhn, E. F., *Analysis and Design of Airplane Structures*, 1949 Ed., pp. C7.1–C7.12; Photo-Offset Company, Cincinnati, 1949.

[8] Kuhn, P., *Investigations on the Incompletely Developed Plane Diagonal-Tension Field*, N.A.C.A. Report No. 697, 1940.

[9] Kromm, A., and Marguerre, K., *Behavior of a Plate Strip under Shear and Compressive Stresses Beyond the Buckling Limit*, N.A.C.A. T.M. No. 870, 1938.

[10] Timoshenko, S., *Theory of Elastic Stability*, 1st Ed., pp. 307 and 391; McGraw-Hill Book Company, Inc., New York, 1936.

Midwestern Conference on Fluid Dynamics

A Midwestern Conference on Fluid Dynamics, together with a meeting of the American Physics Society, Fluid Dynamics Division, is announced by the Department of Mechanical Engineering of the University of Illinois. This conference is to be held on Friday and Saturday, May 12 and 13, 1950, concurrently with the dedication of a new Mechanical Engineering Building at the University.

The Institute of the Aeronautical Sciences is one of the sponsoring societies, and its members are cordially invited to attend.

Sessions on the following subjects are being planned: Aerodynamics—External Flow; Mechanical Engineering—Internal Flow; Symposium on Hypersonic and Low-Density Flow Techniques; Turbulence and Aero-Physics; Astro-Physics, Computing Machines, Multiple Theory of Fluid Dynamics, and Meteorology; Chemical Engineering; and Hydrodynamics and Continuation of External and Internal Flow.

Reservations for accommodations and for the various banquets must be made before May 1. Reservation forms may be obtained from Prof. J. R. Carroll, Jr., Mechanical Engineering Building, University of Illinois, Urbana, Ill.

Dynamic Stability at High Speeds from Unsteady Flow Theory*

I. C. STATLER†

Cornell Aeronautical Laboratory, Inc.

ABSTRACT

A study is made of the longitudinal dynamic response characteristics of a typical fighter-type jet-propelled airplane based upon unsteady flow theory. The 14 longitudinal dynamic stability derivatives are evaluated as complex functions of reduced frequency and Mach Number and used to determine the frequency response curves of normal acceleration and pitching velocity. The results are compared to the corresponding responses computed on the basis of the "quasi-steady" theory, which neglects the effects of frequency and the higher order derivatives and includes the classical "time-lag" of downwash in the form of an $M_{\dot{\alpha}}$ term. It is shown that the discrepancies between the two can be accounted for by using the actual phase lag of the downwash, as determined by nonstationary flow theory, instead of the "time-lag." However, the differences between the simple and the exact results are so small that the inaccuracies of using $M_{\dot{\alpha}}$ are probably no greater than those of the original theoretical assumptions or the experimental data.

INTRODUCTION

THE PROBLEM OF DYNAMIC STABILITY has been greatly simplified, in the past, by assuming that the significant stability derivatives were independent of the frequency of oscillations. This assumption, plus the condition that the speed remains constant, reduced the solution of the longitudinal equations of motion of the airplane (except for phugoid motion) to a simple linear second-order differential equation with constant coefficients. However, a flight-test method for determining the dynamic stability of airplanes, which is being developed by the Cornell Aeronautical Laboratory, Flight Research Department, under a contract with the Aerodynamics Branch, Aircraft Laboratory, Wright-Patterson Air Force Base, involves sinusoidal oscillations of the airplane and its control surfaces or an equivalent analysis of the transient response. Although the frequencies of these oscillations are much lower than flutter frequencies, the question remains whether they are high enough to require that the nonuniform motion of the airplane be considered. Hence, in an endeavor to answer this question, an analysis of the longitudinal response characteristics of an airplane to a sinusoidal oscillation of its elevators is made which depends upon a knowledge of the aerodynamic forces acting on an oscillating surface.

The analysis in this paper is based upon a modification of Dietze's[1, 2] solution for the lift distribution over a harmonically oscillating thin airfoil in subsonic compressible flow. In addition, the effect of the oscillating wing wake upon the horizontal tail surfaces is considered. The stability derivatives are found to be complex functions of frequency and Mach Number. These results are then used to obtain the response curves for a recent U.S.A.F. fighter-type jet-propelled airplane and are compared to the results of the simplified theory. A study of these results enables us to answer the following questions:

(1) Are the effects of frequency in the range in which we are interested—i.e., $0 \leq \omega \leq 8$—rad. per sec.—of sufficient magnitude to justify the additional complications of their inclusion?

(2) Are the higher order derivatives important? These include such terms as angular acceleration, translational acceleration, elevator velocity, and elevator acceleration, which are usually neglected in the simplified theory.

(3) Is the assumption of a "time-lag" term sufficiently accurate for determining the effect of the wing wake upon the horizontal tail?

The present paper is an abbreviated version of the final report published recently by the Cornell Aeronautical Laboratory under a similar title. This report presents not only the detailed derivations but also graphical representations of the results so that applications can be made without an extensive knowledge of the theory.

SYMBOLS AND CONVENTIONS

Conventions

Axes.—Stability axes are used throughout. These axes are fixed in the airplane and therefore move with it during a maneuver. The origin 0 lies at the center of gravity of the airplane. 0X and 0Z lie in the plane of symmetry, and 0Y is perpendicular to it. 0X lies parallel to the free-stream wind vector (or parallel to the flight path) in trimmed level flight.

X-axis—positive forward.

Y-axis—positive along the right wing.

Z-axis—positive downward.

Linear Displacements.—A linear displacement along a positive reference axis is considered to be positive.

Angular Displacements and Moments.—An angular displacement or moment that is clockwise when viewed from the origin looking along a positive reference axis is considered to be positive.

Presented at the Session on Transonic and Supersonic Aerodynamics, Seventeenth Annual Meeting, I.A.S., New York, January 24–27, 1949. Received December 2, 1949.

* The author wishes to acknowledge the assistance of W. O. Breuhaus, D. W. Rhoads, Miss Marjorie Easterbrook, and Mrs. Jane Rouzer, of the Cornell Aeronautical Laboratory, Flight Research Staff, in the preparation of this report.

† Aerodynamicist, Flight Research Department.

Velocities and Accelerations.—Velocities and accelerations, either linear or angular, are considered positive in the same sense as the corresponding displacements.

Control Surface Deflections.—Positive elevator angle is associated with a downward movement of the elevator trailing edge.

Symbols

U = true air speed, ft. per sec.
w = incremental velocity along Z, ft. per sec.
$\dot{w}$ = incremental acceleration along Z due to a change in w, ft. per sec.^{2}
q = pitching velocity, rad. per sec.
$\dot{q}$ = pitching acceleration due to change in q, rad. per sec.^{2}
δ_e = elevator deflection, deg. or rad.
$\dot{\delta}_e$ = elevator velocity, $d\delta_e/dt$, deg. or rad. per sec.
$\ddot{\delta}_e$ = elevator acceleration, $d^2\delta_e/dt^2$, deg. or rad. per sec.^{2}
D = differential operator = d/dt
g = acceleration of gravity, ft. per sec.^{2}
I_y = moment of inertia about principal Y-axis, slug-ft.^{2}
m = mass of airplane, slugs
S = wing area, sq.ft.
c = mean aerodynamic chord, ft.
l = length of fuselage, ft.
ω = angular frequency, rad. per sec.
ρ = mass density of air, slugs per cu.ft.
Φ = phase angle, general—phase relations indicated by subscripts—i.e., Φ_{m_n} = phase of m with respect to n
k = reduced frequency = $\omega c/2U$, nondimensional
F_T = transverse force, lbs.
r = fuselage radius, ft.
n_z = normal acceleration per g, nondimensional
Z = force along Z, lbs.
M = pitching moment, ft.lbs.

$$Z_w = \frac{1}{m}\frac{\partial Z}{\partial w}, \quad Z_q = \frac{1}{m}\frac{\partial Z}{\partial q}, \quad \text{etc.}$$

$$M_w = \frac{1}{I_y}\frac{\partial M}{\partial w}, \quad M_q = \frac{1}{I_y}\frac{\partial M}{\partial q}, \quad \text{etc.}$$

$$dC_L/d\alpha = -(2m/\rho US)Z_w$$
$$dC_L/d\delta_e = -(2m/\rho U^2S)Z_{\delta_e}$$
$$dC_m/d\alpha = (2I_y/\rho USc)M_w$$
$$dC_m/d\delta_e = (2I_y/\rho U^2Sc)M_{\delta_e}$$

A bar placed over a variable indicates the maximum value of that variable during an oscillation.

The Problem

The problem, then, is to obtain theoretical expressions for the responses of an airplane in longitudinal sinusoidal motion at high subsonic speeds from unsteady flow theory. The total aerodynamic forces and moments are obtained by summing the effects of the five component parts of the overall problem. These are: (A) the oscillating wing, (B) the oscillating horizontal tail, (C) the horizontal tail in the wake of an oscillating wing, (D) the oscillating fuselage, and (E) the jet. Each of these problems will be discussed individually.

(A) *The Oscillating Wing*

The first attempt to calculate the air forces on an oscillating airfoil in subsonic compressible flow was undertaken by Possio[3] and resulted in approximate values for the lift and moment on a wing without a control surface. Possio's two-dimensional derivative theory applies for coupled simple-harmonic normal and pitching oscillations of an infinite, thin airfoil moving at subsonic speeds without shock waves. The flow is assumed to be adiabatic, and the Kutta-Joukowsky condition is satisfied at all times. From the linearized equation of motion for two-dimensional unsteady compressible flow and with the additional assumption of small disturbances, a simple differential equation is obtained in terms of an acceleration potential. The solution is then represented by a special system of doublets with a chordwise distribution of intensity such that the correct normal velocity is obtained at all points on the profile. Since the lift distribution is directly proportional to the dipole strength distribution, the resultant integral equation also determines the lift distribution. However, in order to determine this distribution, it is necessary to resolve a singular integral equation with such a highly complex nucleus that the difficulties entailed are insurmountable. Possio's approximate solution is obtained by satisfying the boundary conditions only at a finite number of points along the airfoil.

Another solution, devised by Dietze,[1, 2] is an iterative procedure based on the assumption that the lift distribution is composed of the incompressible lift and a small additional lift caused by the influence of compressibility. Küssner[4] has solved the integral equation for the incompressible case, and the additional term is obtained by repeatedly solving an integral equation with a kernal of the incompressible problem. In this manner, the lift distribution is obtained in terms of reduced frequency, Mach Number, and the motion of the profile. The accuracy of this solution depends not only upon the number of steps for which the process is carried out but also upon the reduced frequency and Mach Number. The convergence becomes worse with increasing reduced frequency and Mach Number. However, since we are interested only in extremely small values of reduced frequency, $0 \leq k \leq 0.1$, and since the reduced frequency decreases with increasing Mach Number, for a given angular frequency, the lifts and moments for the oscillating wing with flap used in this paper are reasonably accurate.

The two-dimensional results are corrected for three-dimensionality by a function corresponding to Reissner's[5] finite span correction factor in the incompressible case. This is justifiable since, in effect, we are correcting the sectional lift for compressibility and then modifying for finite aspect ratio as Reissner has done for the incompressible problem.

The linearization of this problem makes it possible to divide complicated motions of the wing into so-called degrees of freedom from which the final solution is obtained by superposition. Accordingly, the simple case of harmonic oscillations of a rigid wing can be built up from: (a) translation of the wing as a whole, which

corresponds to flight along a straight path with changing angle of attack; and (b) rotation of the wing about some reference axis, which corresponds to flight along a curved path at constant angle of attack.

(*B*) *The Oscillating Horizontal Tail*

The aerodynamic forces derived in the preceding section for an oscillating wing can also be applied to the horizontal tail after introducing the proper area, chord length, reduced frequencies, and efficiency factor. Since the longitudinal oscillation of the airplane is obtained through a sinusoidal motion of the elevators, it is also necessary to consider the forces and moments due to the deflection, velocity, and acceleration of the elevator. In addition, it must be remembered that the empennage moves in a nonuniform stream.

(*C*) *The Horizontal Tail in the Wake of an Oscillating Wing*

During unsteady motions of the airplane, the wing leaves a sheet of vortices of varying strength in its wake. The velocity induced by these vortices has a pronounced effect on the direction of the flow of air in the vicinity of the tail. Influencing the downwash at any point in the wake are the bound vortices, the shed vortices, and the trailing vortices. Given the strength distribution for each of these, the induced velocity at any point can be determined. The incremental velocity due to a single vortex is found by the Biot-Savart rule, and the total downwash is obtained by integrating over the proper regions using the Cauchy residue theorem at the singular points. By this method, we find the downwash angle at the tail as a function of angle of attack; pitching velocity; angular and translational accelerations; aspect ratio; and frequency of oscillation of the wing, of tail length, and of Mach Number. The additional force on the tail due to the oscillating wing can then be obtained.

(*D*) *The Oscillating Fuselage*

Thus far we have considered the components of the airplane which contribute the major portion of the total aerodynamic forces and moments. In addition to the wing and empennage, however, we should determine the influence of the fuselage upon the dynamic stability.

Consider that the fuselage, at any moment of the oscillation, is in uniform circular flight. Munk[6] found that, for an elongated airship turning with an angle of attack, α, the transverse force and moment in curvilinear flight are the same as in straight flight with the same angle of attack α. The theoretical conclusion that the damping due to pitching is zero has been experimentally verified, for all practical purposes, in a series of tests conducted by Cotter.[7] With this assumption, calculations of the stability derivatives for the body alone become simple.

Laitone[8] and Tsien[9] have found that, for an extremely slender body of revolution, the loading was unaffected by compressibility.

Therefore, the transverse force distribution on a body of revolution moving at subsonic velocity is obtained by using the exact expression for the incompressible potential flow about a prolate spheroid:

$$\frac{F_T}{(1/2)\rho U^2} = \int_0^l \frac{4\pi\alpha r(dr/dx)}{1 + (dr/dx)^2}\, dx$$

(*E*) *The Jet*

Since this method of obtaining dynamic stability characteristics from unsteady flow theory is applied to a typical jet-propelled airplane as an illustrative example, we should consider the effect of the jet. An aerojet, such as is used on this type of airplane, always damps the oscillations of an airplane, provided the distance of the air intake from the center of gravity of the airplane is less than the distance of the exhaust from the center of gravity. Since the influence of the jet is derived from a Coriolis effect, the result is an increment in the moment due to pitching velocity. Using the relationships derived by Braun,[10] it can be shown that this damping influence is negligible in computing the response characteristics in this example, although it may have considerable effect on faster airplanes.

Thus, by summing the effects discussed in the preceding sections, the 14 longitudinal dynamic stability derivatives of the airplane are obtained. These include the lifts and moments due to angle of attack; pitching velocity; vertical and pitching accelerations; and deflection, velocity, and acceleration of the elevator. The derivatives found by this method are complex functions of Mach Number and reduced frequency.

With these stability derivatives determined and with the assumption that the forward velocity remains approximately constant, the basic dynamic longitudinal equations of motion may be written in operational form as is shown in Table 1. Solving simultaneously and substituting $i\omega$ for the operator D, since simple harmonic oscillations are being considered, expressions for the pitching velocity and the normal acceleration per degree elevator deflection and for their phases are obtained. By introducing the values of the complex derivatives into these equations, we are able to plot the responses and their phase angles against the frequency of elevator oscillation for each condition of Mach Number, altitude, and center-of-gravity position.

A comparison of the stability derivatives considered in the exact theory, the simple theory, and a modified simple theory, which is discussed below, is also presented in Table 1. The exact theory contains all 14 of the dynamic longitudinal stability derivatives as complex functions of frequency.

Table I

EQUATIONS OF MOTION

$$\left(1 - Z_{\dot{w}}\frac{1}{D} - Z_w\frac{1}{D}\right)\eta_e - \left(Z_q + Z_{\dot{q}}D + UZ_{\dot{w}} + Z_w\frac{U}{D}\right)q = \left(Z_{\ddot{\delta}_e}D^2 + Z_{\dot{\delta}_e}D + Z_{\delta_e}\right)\delta_e$$

$$-\left(M_{\dot{w}} + M_w\frac{1}{D}\right)\eta_e + \left(D - M_{\dot{q}}D - M_q - UM_{\dot{w}} - M_w\frac{U}{D}\right)q = \left(M_{\ddot{\delta}_e}D^2 + M_{\dot{\delta}_e}D + M_{\delta_e}\right)\delta_e$$

STABILITY DERIVATIVES USED IN:

(A) – EXACT THEORY

$Z_w, Z_{\dot{w}}, Z_q, Z_{\dot{q}}, Z_{\delta_e}, Z_{\dot{\delta}_e}, Z_{\ddot{\delta}_e}$

$M_w, M_{\dot{w}}, M_q, M_{\dot{q}}, M_{\delta_e}, M_{\dot{\delta}_e}, M_{\ddot{\delta}_e}$

} COMPLEX FUNCTIONS OF FREQUENCY

(B) – SIMPLE THEORY

Z_w, Z_{δ_e}; M_w, M_q, M_{δ_e}

$M_{\dot{w}}$ (CLASSICAL "TIME LAG" OF DOWNWASH)

} REAL AND INDEPENDENT OF FREQUENCY

(C) – MODIFIED SIMPLE THEORY

Z_w, Z_{δ_e}; M_w, M_q, M_{δ_e}

$\frac{d\epsilon}{d\alpha}$ — — COMPLEX FUNCTION OF FREQUENCY

The Simplified Theory

In the past, the following assumptions were made which greatly simplified response calculations:

(1) The stability derivatives are real and independent of frequency.

(2) The higher order aerodynamic derivatives, $Z_{\dot{w}}, Z_{\dot{q}}, Z_{\dot{\delta}_e}, Z_{\ddot{\delta}_e}, M_{\dot{q}}, M_{\dot{\delta}_e}$, and $M_{\ddot{\delta}_e}$, are negligible.

(3) The downwash lag can be approximated by the time required for the flow to travel from the wing to the tail. The downwash lag terms as derived by Cowley and Glauert[11] depend on the translational acceleration dw/dt and are therefore contained in the acceleration derivatives $M_{\dot{w}}$ and $Z_{\dot{w}}$. It is important to note, however, that they arise from a different cause than that usually associated with the acceleration derivatives. Hence, although an $M_{\dot{w}}$ term is included in the simplified theory, it is not comparable to the $M_{\dot{w}}$ derivative obtained from unsteady flow theory, which is due solely to apparent mass effects resulting from the translational acceleration.

With these simplifications, the equations of motion can be written in a form corresponding to a simple spring-mass system with damping, where the equivalent spring and damping constants are functions of the stability derivatives. Laitone[12] has shown that a knowledge of these constants allows the prediction of the airplane motion for any arbitrary control surface motion. Furthermore, a simple evaluation of relative dynamic stability is provided by a comparison of the spring and damping constants for different airplanes.

The Supersonic Case

The basic theory for stability and control at supersonic speed is exactly the same as for the subsonic case—i.e., the equations of motion as shown in Table 1 are valid if the correct values for the stability derivatives are introduced. Hence, the problem is to determine the 14 stability derivatives for an airplane that is pitching sinusoidally at supersonic velocity.

The evaluation of the forces and moments on an oscillating airfoil in a supersonic stream has been ade-

quately covered by several authors[13–15] for the two-dimensional case. Since we are interested in extremely low values of frequency, a first-order approximation is valid and provides simple expressions. Furthermore, we are able to assume that the wing attitude changes slowly relative to the rate at which a disturbance is transferred downstream in the Mach cone. This permits the use of Evvard's[16] method as an approximate three-dimensionality correction for the unsteady case.

With the forces and moments on the wing known, those on the horizontal tail can be found in the same manner as in the subsonic case, except for the determination of the effect of the oscillating wing wake. Theoretically, for a conventional airplane configuration, only that portion of the horizontal tail which lies within the wing Mach cone is affected by a downwash. This downwash has been determined by Lagerstrom and Graham[17] for the steady case. The same approach is utilized for the case of nonuniform motion.

Quantitative results were not available at the time of writing; however, it can be stated that, to a first-order approximation, the stability derivatives are complex functions with real parts independent of and imaginary parts proportional to the frequency.

This problem of dynamic stability at supersonic velocity is treated in more detail in the forthcoming Cornell Aeronautical Laboratory report.

Discussion of Results

The method of determining dynamic stability at high speeds from unsteady flow theory is applied in an illustrative example. The stability derivatives obtained in this manner are plotted against reduced frequency for several Mach Numbers in Figs. 1–14. The curves show the effects of frequency and Mach Number upon the longitudinal dynamic stability derivatives of a typical jet-propelled fighter-type airplane. Wind-tunnel values for the static aerodynamic derivatives are corrected by the theoretical frequency effects.

It would seem from these curves that the influence of frequency becomes increasingly more important with increasing Mach Number. This problem, however, is not so critical as it seems to be at first glance. It must be remembered that the reduced frequency is inversely proportional to the velocity. Therefore, for a given frequency, the reduced frequency diminishes by the ratio of velocities for increasing Mach Number.

In Figs. 15–22, the response curves* of angular velocity and normal acceleration per degree elevator deflection and their phases are plotted against frequency for Mach Numbers of 0.30, 0.50, 0.70, and 0.75. Comparison of the results of simple theory with exact theory shows excellent agreement in both phase and amplitude except at maximum amplitude or resonance frequency. Since the two theories check at the high frequencies, the contributions of nonstationary flow and the higher order derivatives, which are expected to be greatest at the highest frequencies, cannot be important in the range $0 \leq \omega \leq 8$ rad. per sec. Therefore, the differences that appear at resonance frequencies can only be explained by such a term as the downwash lag which has its major effect when the change and rate of change of lift are greatest. This supposition was verified by further calculations based on a procedure referred to in the preceding sections as the modified simple theory. The responses were recomputed using only those derivatives considered in the simple theory with the exception of the downwash lag term. Instead of $M_{\dot{w}}$, the complex form of $d\epsilon/d\alpha$ as obtained from unsteady flow theory was used. The agreement with the so-called exact results is excellent. This is shown by the comparison between the circled points and the solid lines in Figs. 15–22.

Conclusions

In the introduction of this paper, three questions in the problem of dynamic stability at high speeds were raised. Consider the first two: (1) Should the effects of frequency upon the stability derivatives be included and (2) should the higher order derivatives be included?

It has been shown that, at the highest frequencies investigated when these two effects would be maximum, there is excellent agreement between the simple and exact theories. Therefore, the contributions due to both are not important for accurate theoretical responses at subsonic speeds, either because these terms themselves are negligible or because their effects are compensating.

An explanation of the differences between the simple and exact theories must, therefore, lie in the answer to the third question:

(3) Is the simple "time-lag" assumption sufficiently accurate? In answering this question, it is important to consider the degree of accuracy desired. Undoubtedly, the complex form of the downwash as obtained from oscillating airfoil theory is the more correct, since the transient effects of the wing lift are included. The responses obtained by the exact theory have been duplicated merely by using the complex downwash instead of the classical "time-lag" term, $M_{\dot{w}}$. However, the differences between the simple and the exact results are so small, even at the resonance frequencies, that the inaccuracies of using $M_{\dot{w}}$ are probably no greater than those of the original theoretical assumptions or the experimental data.

In conclusion, it can be stated that the quasi-steady method of computing response characteristics at subsonic speeds is reasonably accurate, at least for longi-

* The response curves have been faired into the zero frequency values, although they are not correct in the phugoid frequency range, which is well below 0.5 rad. per sec. At these low frequencies, the speed change is greatest, and its effect becomes extremely important.

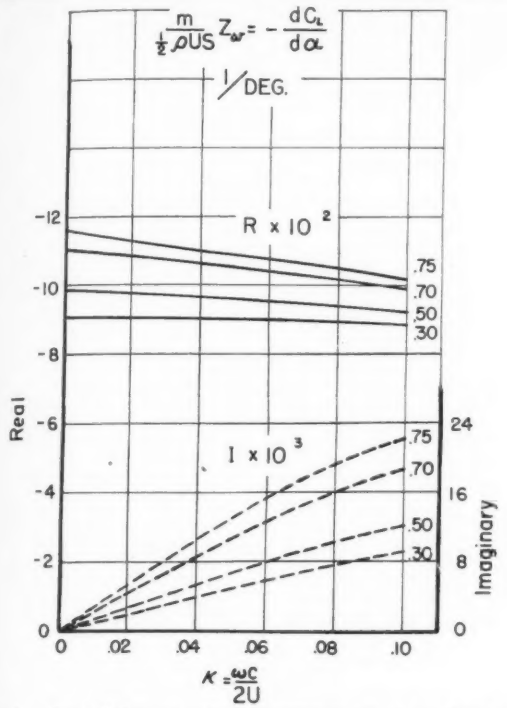

FIG. 1. $(2m/\rho US)Z_w$ vs. reduced frequency for Mach Numbers 0.30, 0.50, 0.70, and 0.75.

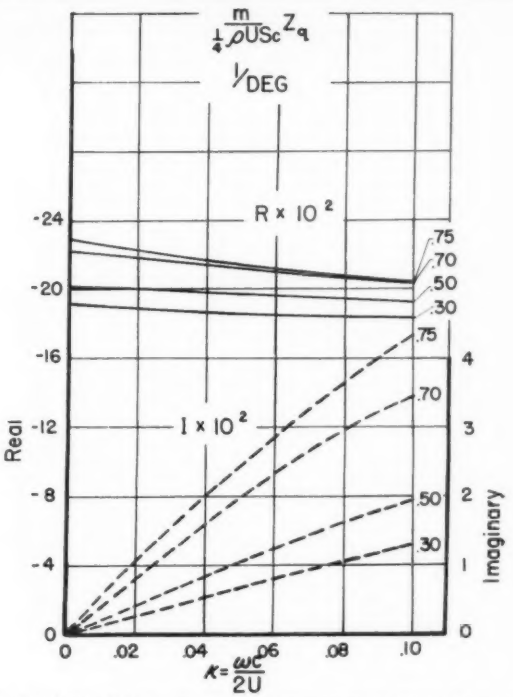

FIG. 3. $(4m/\rho USc)Z_q$ vs. reduced frequency for Mach Numbers 0.30, 0.50, 0.70, and 0.75.

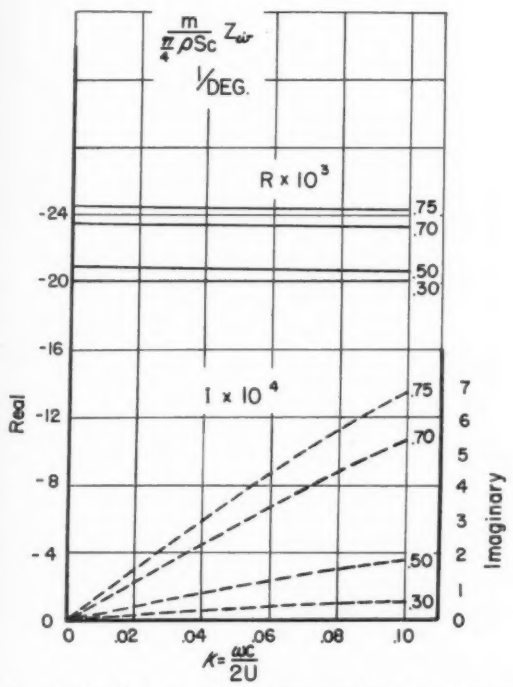

FIG. 2. $(4m/\pi\rho Sc)Z_{\dot{w}}$ vs. reduced frequency for Mach Numbers 0.30, 0.50, 0.70, and 0.75.

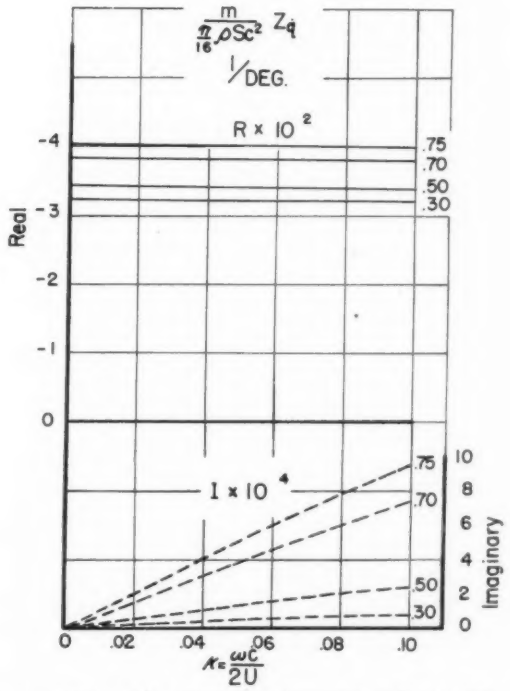

FIG. 4. $(16m/\pi\rho Sc^2)Z_{\dot{q}}$ vs. reduced frequency for Mach Numbers 0.30, 0.50, 0.70, and 0.75.

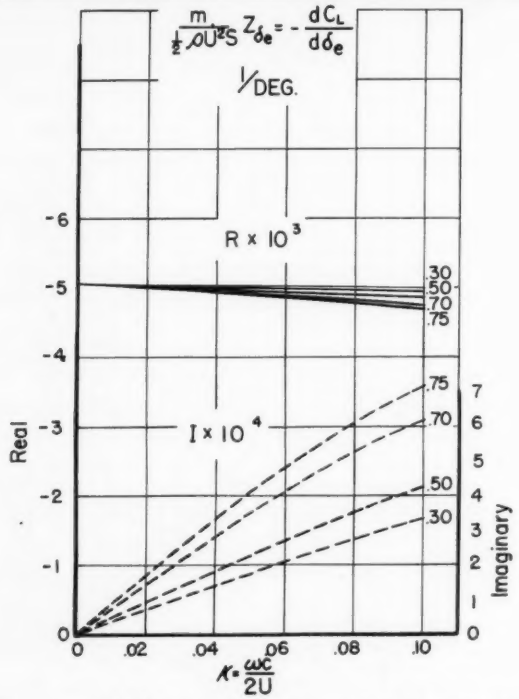

FIG. 5. $(2m/\rho U^2 S)Z_{\delta_e}$ vs. reduced frequency for Mach Numbers 0.30, 0.50, 0.70, and 0.75.

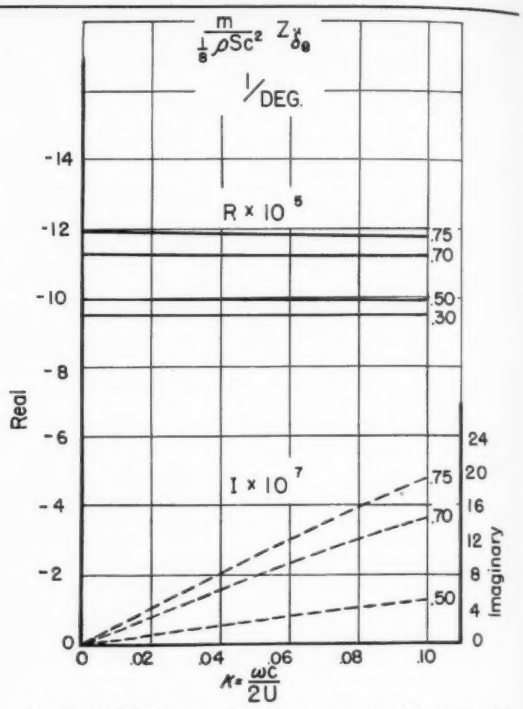

FIG. 7. $(8m/\rho Sc^2)Z_{\dot{\delta}_e}$ vs. reduced frequency for Mach Numbers 0.30, 0.50, 0.70, and 0.75.

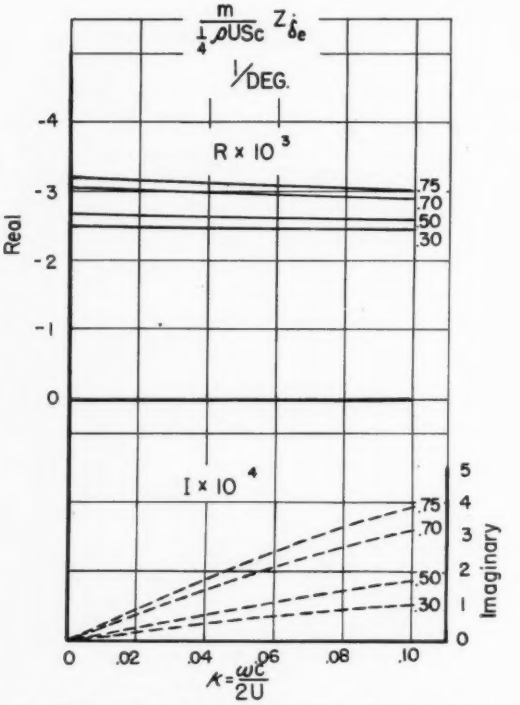

FIG. 6. $(4m/\rho USc)Z_{\dot{\delta}_e}$ vs. reduced frequency for Mach Numbers 0.30, 0.50, 0.70, and 0.75.

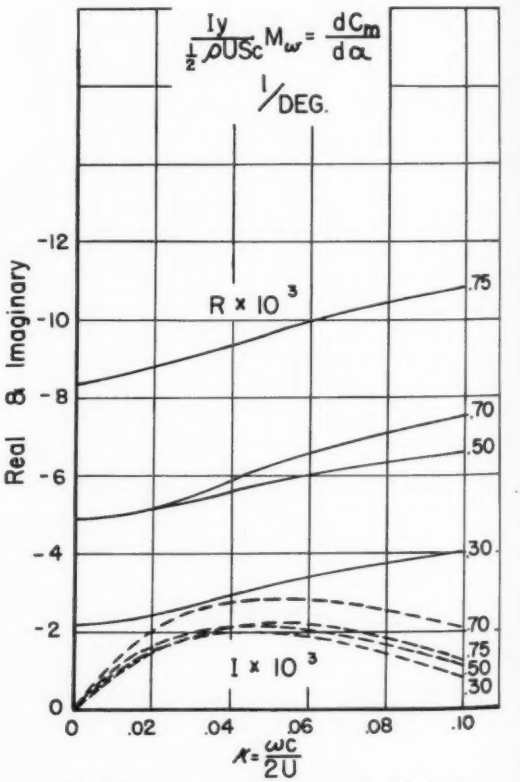

FIG. 8. $(2I_y/\rho USc)M_w$ vs. reduced frequency for Mach Numbers 0.30, 0.50, 0.70, and 0.75.

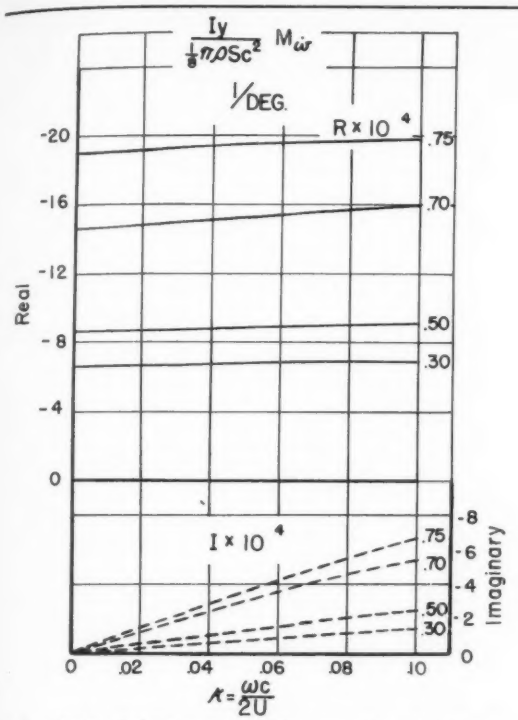

FIG. 9. $(8I_y/\pi\rho Sc^2)M_{\dot{w}}$ vs. reduced frequency for Mach Numbers 0.30, 0.50, 0.70, and 0.75.

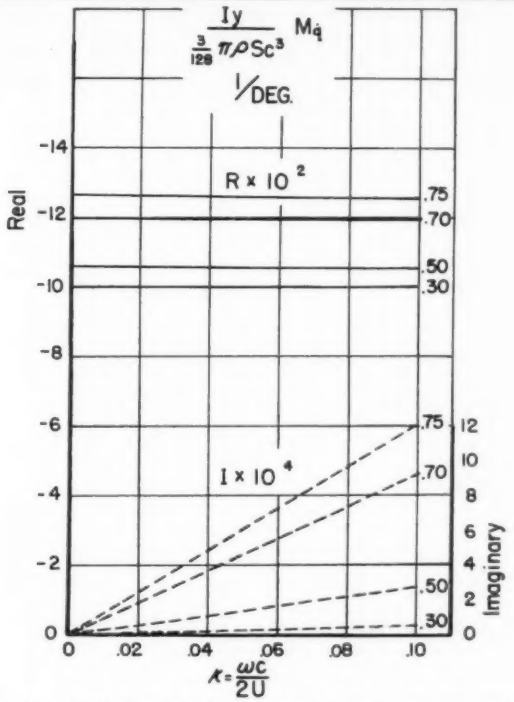

FIG. 11. $(128I_y/3\pi\rho Sc^3)M_{\dot{q}}$ vs. reduced frequency for Mach Numbers 0.30, 0.50, 0.70, and 0.75.

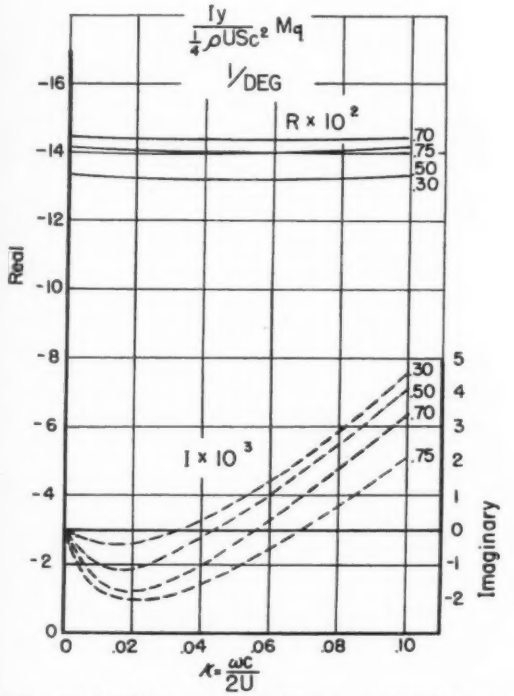

FIG. 10. $(4I_y/\rho USc^2)M_q$ vs. reduced frequency for Mach Numbers 0.30, 0.50, 0.70, and 0.75.

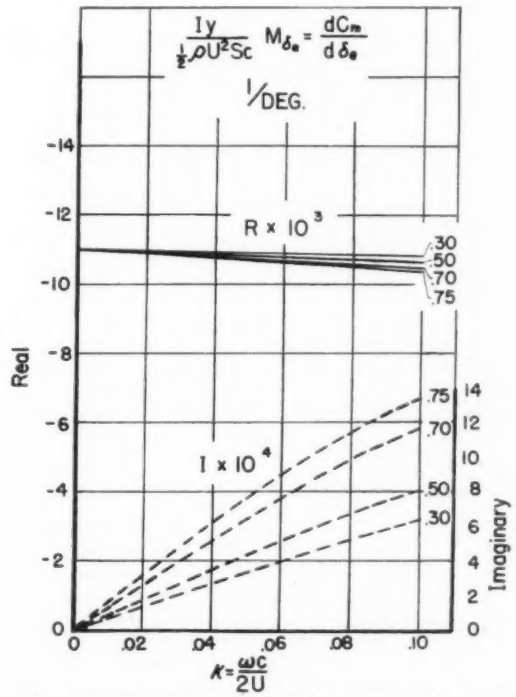

FIG. 12. $(2I_y/\rho U^2Sc)M_{\delta_e}$ vs. reduced frequency for Mach Numbers 0.30, 0.50, 0.70, and 0.75.

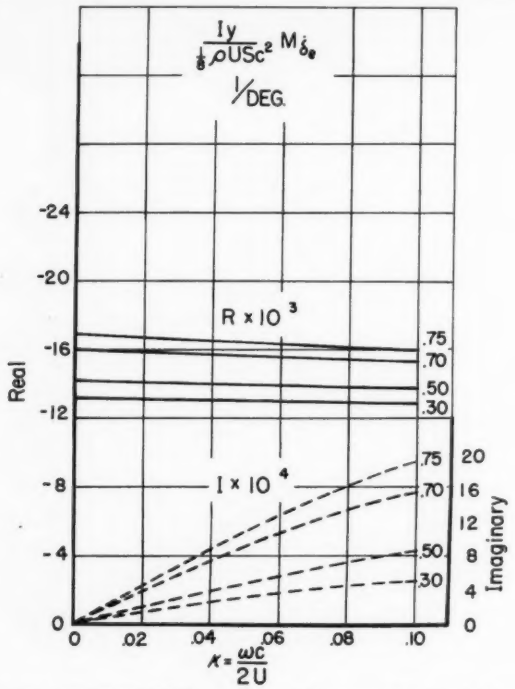

FIG. 13. $(8I_y/\rho USc^2)M_{\dot{\delta}_e}$ vs. reduced frequency for Mach Numbers 0.30, 0.50, 0.70, and 0.75.

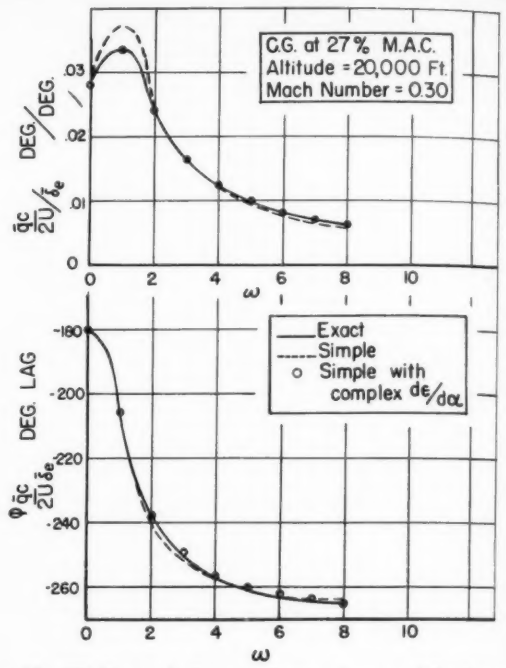

FIG. 15. Pitching velocity per degree elevator deflection vs. frequency.

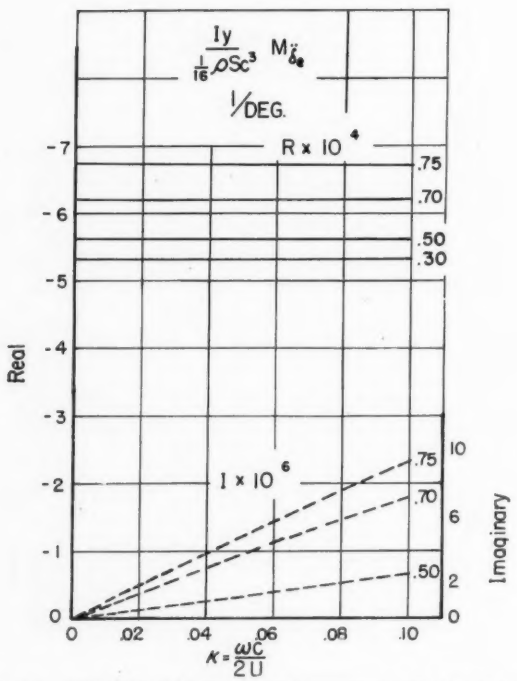

FIG. 14. $(16I_y/\rho Sc^3)M_{\ddot{\delta}_e}$ vs. reduced frequency for Mach Numbers 0.300, 0, 0.70, and 0.75 .5

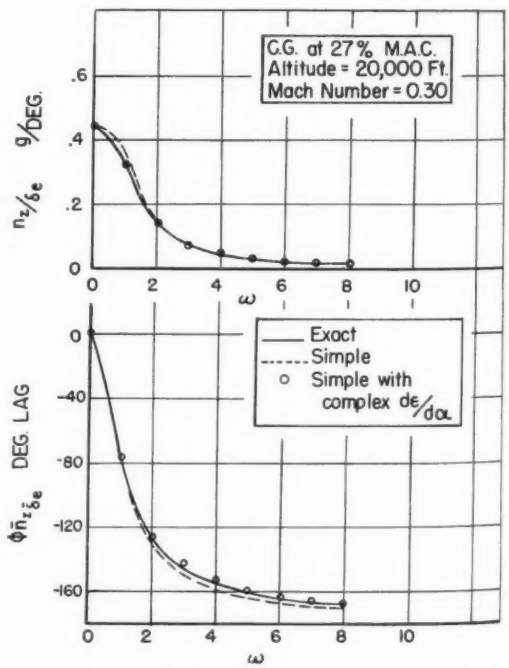

FIG. 16. Normal acceleration per degree elevator deflection vs. frequency.

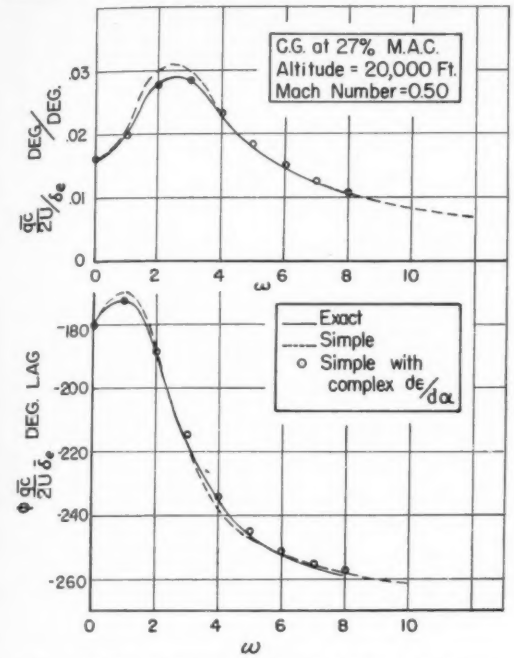

FIG. 17. Pitching velocity per degree elevator deflection vs. frequency.

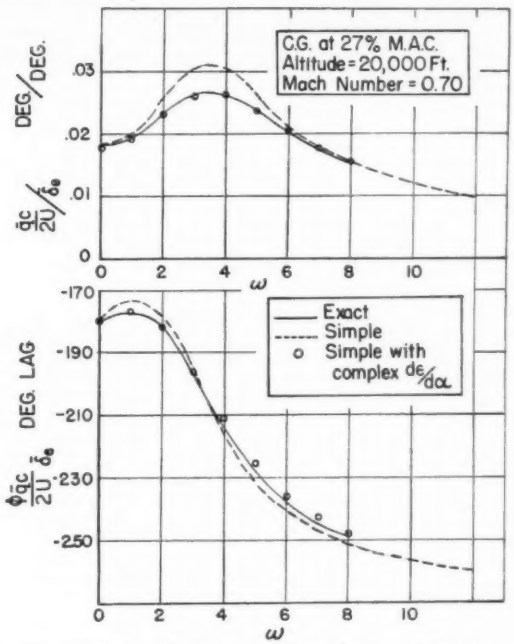

FIG. 19. Pitching velocity per degree elevator deflection vs. frequency.

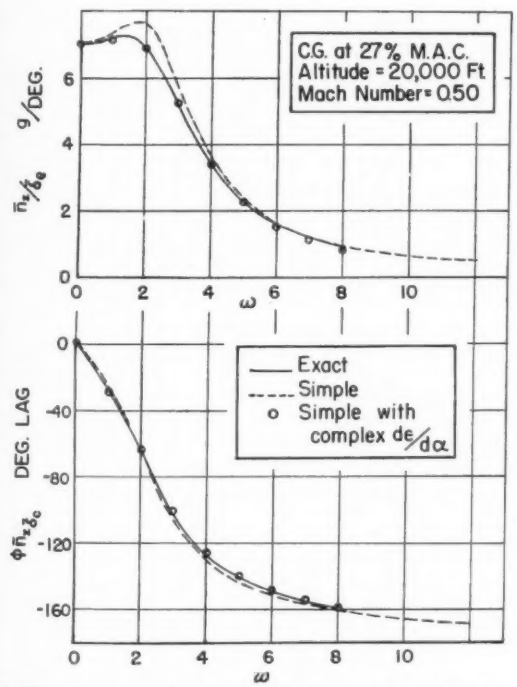

FIG. 18. Normal acceleration per degree elevator deflection vs. frequency.

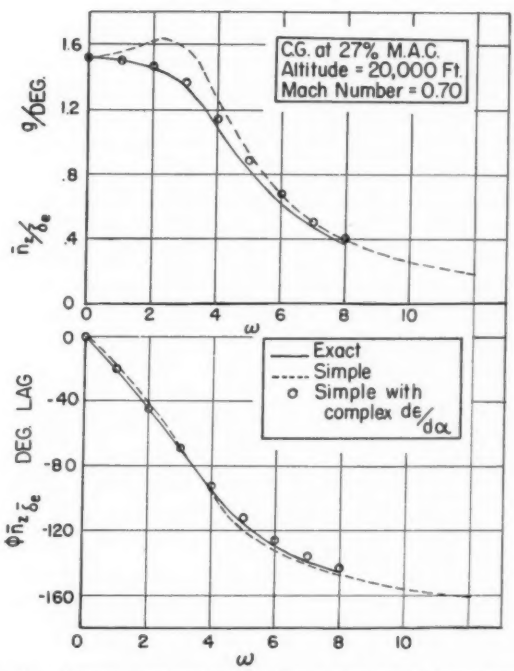

FIG. 20. Normal acceleration per degree elevator deflection vs. frequency.

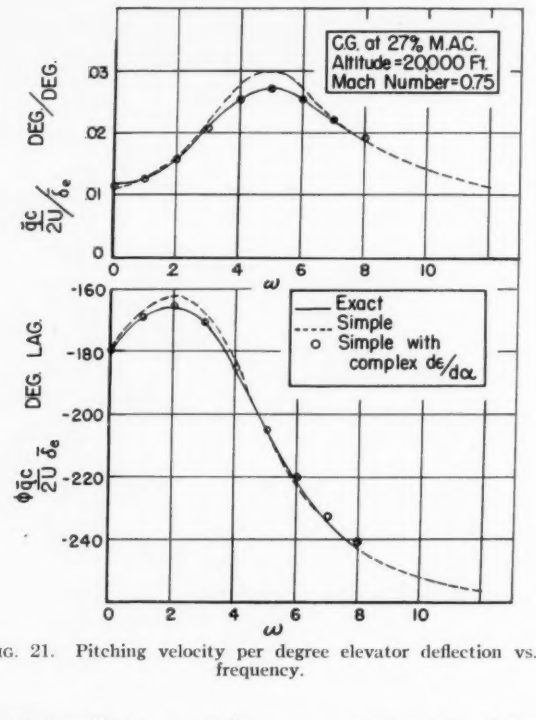

FIG. 21. Pitching velocity per degree elevator deflection vs. frequency.

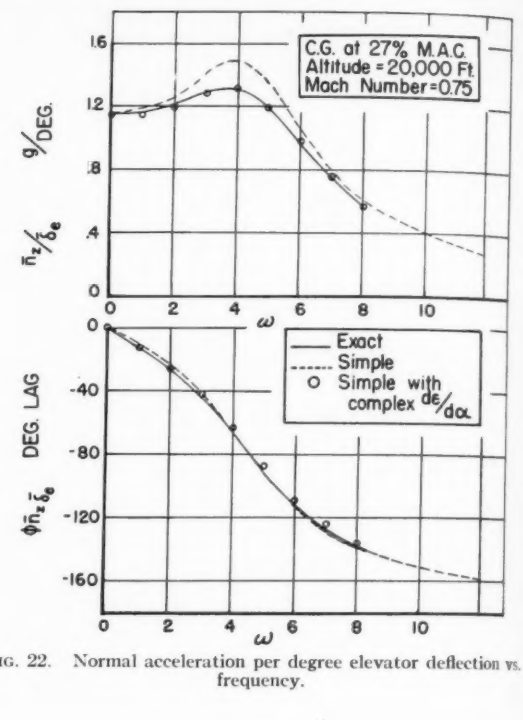

FIG. 22. Normal acceleration per degree elevator deflection vs. frequency.

tudinal oscillations. If the more correct values of the downwash as obtained from unsteady theory are to be used instead of the "time-lag" $M_{\dot{w}}$ term, they can be obtained easily from general charts as functions of reduced frequency, Mach Number, and tail position with respect to the wing, which will be contained in a forthcoming Cornell Aeronautical Laboratory report. Hence, the determination of the longitudinal dynamic stability of a conventional airplane in subsonic compressible flow is no more difficult than the equivalent incompressible problem.

The possibility of unsteady flow effects upon the lateral dynamic stability characteristics of an airplane is still open to question. In particular, the problem of lateral "snaking" oscillations *may* be clarified by further investigation based on nonstationary flow theory. A preliminary study, however, reveals no obvious reasons for the author to suspect greater effects in the lateral case than were presented in the longitudinal case.

REFERENCES

[1] Dietze, *The Air Forces on the Harmonically Vibrating Wing Compressible Medium at Subsonic Velocity* (Plane Problem), AAF Translation F-TS-506-RE, November, 1946.

[2] Dietze, *Part II: Numerical Tables and Curves*, AAF Translation F-TS-948-RE, March, 1947.

[3] Possio, C., *The Aerodynamic Forces on an Oscillating Profile in Compressible Fluid at Subsonic Speed*, Aerotecnica, Vol. 18, No. 4, pp. 441–458, April, 1948 (R. T. P. Translation No. 987).

[4] Küssner, H. C., *Zusammenfassender Bericht uber den instationaren Auftrieb von Flugeln* (summary report on the nonstationary lift on wings), Luftfahrtforschung, Vol. 13, No. 12, pp. 410–424, December, 1936.

[5] Reissner, E., *Effect of Finite Span on the Airload Distributions for Oscillating Wings. I—Aerodynamic Theory of Oscillating Wings of Finite Span*, N.A.C.A. T.N. No. 1194, March, 1947.

[6] Munk, M., *The Aerodynamic Forces on Airship Hulls*, N.A.C.A. Report No. 184, 1924.

[7] Cotter, W. E., Jr., *Summary and Analysis of Data on Damping in Yaw and Pitch for a Number of Airplane Models*, N.A.C.A. T.N. No. 1080, May, 1946.

[8] Laitone, E. V., *The Linearized Subsonic and Supersonic Flow About Inclined Slender Bodies of Revolution*, Journal of the Aeronautical Sciences, Vol. 14, No. 11, pp. 631–642, November, 1947.

[9] Tsien, H., *Supersonic Flow over an Inclined Body of Revolution*, Journal of the Aeronautical Sciences, Vol. 5, No. 12, pp. 480–483, October, 1938.

[10] Braun, G. W., *Damping Influence of an Aero-Jet Duct*, ATSC-(T-2), IRE-22, December, 1945.

[11] Cowley, W. L., and Glauert, H., *The Effect of Lag of the Downwash on the Longitudinal Stability of an Airplane*, R. & M. No. 718, February, 1921.

[12] Laitone, E. V., *A New Approach to the Analysis of Airplane Motions*, Comptes Rendus du Sixieme Congress International de Mecanique Appliquée, September, 1946.

[13] Possio, C., *The Aerodynamic Action on an Oscillating Aerofoil at Supersonic Speed*, Acta Pontif. Acad. Sci., Vol. 1, No. 11, pp. 93–105, 1937 (A.R.C. Translation No. 7668).

[14] von Borbely, S., *Aerodynamic Forces on an Harmonically Oscillating Wing at Supersonic Velocity (2-Dimensional Case)*, Z.A.M.M., Vol. 22, No. 4, pp. 190–205, August, 1942 (R.T.P. Translation No. 2019).

[15] Garrick, I. E., and Rubinow, S. I., *Theoretical Study of Air-Forces on an Oscillating or Steady Thin Wing in a Supersonic Main Stream*, N.A.C.A. T.N. No. 1383, July, 1947.

[16] Evvard, J. C., *Distribution of Wave Drag and Lift in the Vicinity of Wing Tips at Supersonic Speeds*, N.A.C.A. T.N. No. 1382, July, 1947.

(*Continued on page 255*)

Some Exact Solutions of the Flow Through Annular Cascade Actuator Discs*

STEPHEN L. BRAGG† AND WILLIAM R. HAWTHORNE‡
Massachusetts Institute of Technology

SUMMARY

Exact solutions are presented for two types of flow of an incompressible inviscid fluid through an annular passage with a discontinuity in tangential velocity at one section, as would occur at a cascade of airfoil blades of negligible chord. When stagnation conditions are constant throughout the flow region, it is shown that the product of the tangential vorticity component (η) and the radius (r) is constant along a stream line. The particular case when this product is a linear multiple of the stream function (ψ) is solved by dividing ψ into persistent and perturbation components and separating the variables. A second exact solution is obtained when the product (ηr) is a function of radius alone and when the stagnation conditions are allowed to vary. Two solutions of either of the above kinds can be exactly matched at the discontinuity section, thus determining the complete flow pattern for arbitrarily selected conditions at infinity. The axial velocity at this section is almost exactly the mean of upstream and downstream values at the same radius. The family of exact solutions may be of use in estimating the accuracy of approximate solutions and, as shown in a numerical example, may match some desired flow conditions sufficiently closely to be of interest in design.

INTRODUCTION

THE ESSENTIAL FEATURE of axial compressors and turbines is the arrangement of alternate stationary and rotating cascades of airfoils; these alter the angular momentum of the working fluid as it passes so that work is done on or by it, thus raising or lowering its pressure and energy levels. In designing such turbomachinery, the required work distribution is known, and it is necessary to find the blade profiles that will produce it.

An analysis of the flow through a single annular cascade is a first step in the study of this problem. This cannot be done by the classical two-dimensional methods because of the radial pressure gradients and velocities induced by the fluid rotation, although attempts may be made to correlate data with results from two-dimensional cascades. The radial pressure gradient is associated with centrifugal effects due to the tangential velocities produced by the blades. Conservation of angular momentum demands that, in the absence of fluid shear, these persist as the fluid flows downstream to infinity after a cascade. The radial velocities, however, are purely local phenomena caused by the adjustment in mass flow distribution associated with the different velocity profiles on either side of the cascade. We may then regard the flow as divided into two parts—upstream and downstream. In each, the flow conditions are basically those that would obtain at infinity, but, in the region of the cascade, perturbation components are introduced to smooth out the transition from one region to another.

Various authors have suggested analytical approaches to the determination of the flow through cascades in order to obtain the blade profiles for a given duty. Meyer[1] has studied the flow through free vortex blades. Marble[2] has presented a general solution, but this involves some mathematical approximation in order to linearize the equation of motion.

This paper describes two physically possible types of incompressible nonviscous flow for which exact solutions of the equations of motion are found and applied directly to the limiting case of a cascade of negligible chord width. This is a special case of the actuator disc of propeller theory. The flow is assumed to be steady and uninfluenced by external forces, except the normal forces at the parallel walls of the annulus. At one particular section, the actuator disc, there is a discontinuity in the tangential—though not in the other velocity components. Rotational symmetry is assumed—that is, there is no variation in flow conditions at a given radius with angular position. The disc is, in effect, the limiting case of a cascade containing an infinite number of blades of infinitesimal chord which exert an impulse on the fluid in the tangential direction. The basic equations employed are Euler's Equation of Motion, the equation of continuity, and the thermodynamic entropy and energy equation. Heat transfer to the fluid is neglected, and it is assumed that the fluid flows isentropically from a region where it is all at the same entropy.

BASIC EQUATIONS OF ANNULAR FLOW

In the absence of body forces, Euler's equations of motion for rotationally symmetric steady flow of a nonviscous fluid referred to cylindrical polar coordinates r, θ, and z (Fig. 1) may be written:

$$c_r \frac{\partial c_r}{\partial r} + c_z \frac{\partial c_r}{\partial z} - \frac{c_\theta^2}{r} = -\frac{1}{\rho}\frac{\partial p}{\partial r} \quad \text{(radially)} \qquad (1)$$

$$c_r \frac{\partial c_\theta}{\partial r} + c_z \frac{\partial c_\theta}{\partial z} + \frac{c_r c_\theta}{r} = 0 \quad \text{(tangentially)} \qquad (2)$$

Received August 11, 1949.

* From a thesis submitted in partial requirement for the degree of M.Sc. by Stephen L. Bragg, June, 1949.

† Commonwealth Fund Fellow.

‡ George Westinghouse Professor of Mechanical Engineering.

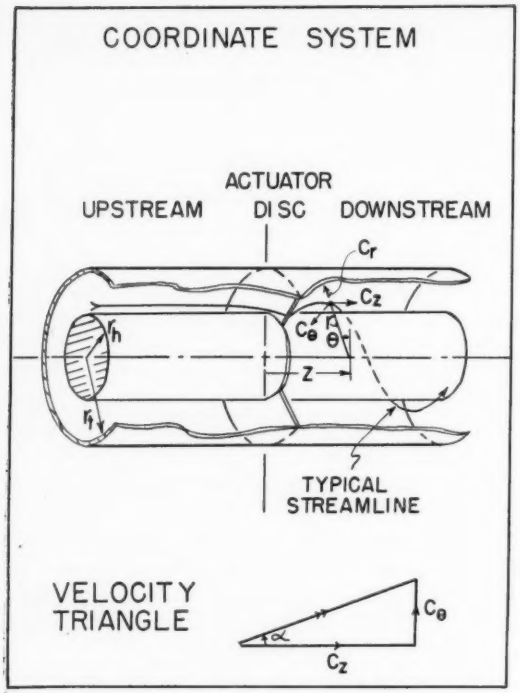

FIG. 1. Coordinate system.

$$c_r \frac{\partial c_z}{\partial r} + c_z \frac{\partial c_z}{\partial z} = -\frac{1}{\rho}\frac{\partial p}{\partial z} \quad \text{(axially)} \tag{3}$$

c_r, c_θ, and c_z represent the velocity components in the three coordinate directions.

The equation of continuity under similar conditions becomes:

$$(\partial/\partial z)\ (\rho r c_z) + (\partial/\partial r)\ (\rho r c_r) = 0 \tag{4}$$

The components of vorticity are defined by the relations:

$$\xi = -\partial c_\theta/\partial z \quad \text{(radial component)} \tag{5}$$

$$\eta = (\partial c_r/\partial z) - (\partial c_z/\partial r) \quad \text{(tangential component)} \tag{6}$$

$$\zeta = (1/r)\ (\partial/\partial r)\ (r c_\theta) \quad \text{(axial component)} \tag{7}$$

The enthalpy of the fluid at a point, h, and the stagnation enthalpy, H—i.e., the value of the enthalpy that would be reached if the fluid were brought to rest adiabatically—are connected by the steady flow energy equation:

$$H = h + (1/2)\ (c_r^2 + c_\theta^2 + c_z^2)$$

If we assume that all the fluid was initially at the same entropy and that all subsequent changes occur isentropically, the thermodynamic relation $\delta h = \delta p/\rho$ applies, and so, for all variation through the flow,

$$\delta H = (\delta p/\rho) + (1/2)\delta(c^2) \tag{8}$$

Combining Eqs. (1), (2), and (3) with Eq. (8) to eliminate pressure differentials and introducing the vorticity components from Eqs. (5), (6), and (7),

$$\xi c_\theta - \eta c_z = \partial H/\partial r \tag{9}$$

$$\zeta c_z - \xi c_r = 0 \tag{10}$$

$$\eta c_r - \zeta c_\theta = \partial H/\partial z \tag{11}$$

Eq. (4) shows that it is possible to define a "Stream Function," ψ, of r and z, such that

$$\rho r c_r = \rho_0(\partial\psi/\partial z) \tag{12}$$

$$\rho r c_z = -\rho_0(\partial\psi/\partial r) \tag{13}$$

where ρ_0 is a constant reference density.

From the tangential equation of motion, Eq. (2),

$$[c_r(\partial/\partial r) + c_z(\partial/\partial z)](r c_\theta) = 0$$

This agrees with the physical concept that in the absence of external forces angular momentum is preserved, since it shows that rc_θ is constant along a stream line. Thus, $rc_\theta = \theta$ is a function of ψ. Also, H is a function of ψ (reference 3, article 165). The relation between θ and the vorticity components is analogous to that between ψ and the corresponding velocities, for

$$r\xi = -\partial\theta/\partial z \tag{14}$$

$$r\zeta = \partial\theta/\partial r \tag{15}$$

From Eqs. (6), (12), and (13),

$$dH/d\psi = (1/r^2)[\theta(d\theta/d\psi) + (\rho_0/\rho) r\eta] \tag{16}$$

$$\eta r = \frac{\rho_0}{\rho}\left(\psi_{zz} + \psi_{rr} - \frac{1}{r}\psi_r\right) - \frac{\rho_0}{\rho^2}\left(\psi_z\frac{\partial\rho}{\partial z} + \psi_r\frac{\partial\rho}{\partial r}\right) \tag{17}$$

where ψ_r, ψ_z, etc., denote partial differentiation of ψ with respect to r and z, etc.

It is of interest to note the similarity between Eq. (16) and the relation derived by Crocco[5] for flow behind an axially symmetric shock, which is

$$\frac{dH}{d\psi} - T\frac{ds}{d\psi} = \frac{1}{r^2}\frac{\rho_0}{\rho} r\eta \tag{16a}$$

where s is the entropy and T is the absolute temperature.

Hence, Eq. (16) may be extended to a more general one allowing for entropy variation:

$$\frac{dH}{d\psi} - \frac{Tds}{d\psi} = \frac{1}{r^2}\left(\theta\frac{d\theta}{d\psi} + \frac{\rho_0}{\rho} r\eta\right) \tag{16b}$$

In incompressible flow, the relations (16) and (17) simplify to

$$dH/d\psi = (1/r^2)[\theta(d\theta/d\psi) + \eta r] \tag{18}$$

where

$$\eta r = \psi_{rr} + \psi_{zz} - (1/r)\psi_r \tag{19}$$

Features of various types of flow may be distinguished by examining Eq. (18).

(*a*) *Isentropic Flows with H = Constant.*—This implies constant stagnation pressure and includes all

isentropic flows through stationary or rotating cascades with constant circulation along the blades.

Since $dH/d\psi = 0$, ηr must be a function of ψ and constant along a stream surface. Also, from Eqs. (9), (10), and (11),

$$\xi/c_r = \eta/c_\theta = \zeta/c_z = \Omega/c \tag{20}$$

where Ω is the resultant vorticity. The vortex lines thus follow the stream lines.

(*b*) *Isentropic Flows with rc_θ Zero or Constant.*— From Eq. (18),

$$dH/d\psi = \eta/r \tag{21}$$

and, hence, η/r is constant along the stream surface.

The condition that η/r should be constant along a stream surface, mentioned by Marble[2] and in Lamb (reference 3, article 165), was applied to axially symmetric flow—that is, flow with no tangential velocity. As shown here, it also results when rc_θ is constant and, hence, when ξ and ζ are zero. It ranges from the trivial, vortex-free case when $\eta = 0$ and $H =$ constant (the so-called free vortex flow) to flow with varying H and η.

The First Exact Solution

In order to obtain the first solution, incompressible flow with constant stagnation enthalpy has been assumed. Then, from Eq. (18),

$$\eta r = f(\psi) \tag{22}$$

The perturbation concept of the flow suggests that a suitable form for the stream function is given by the relation:

$$\psi = \psi_\infty + \sum_n e^{\pm k_n z}\psi_n' \tag{23}$$

where ψ_∞ and ψ_n' are functions of r alone. k_n is assumed positive, and the sign of the index $\pm k_n z$ is such that the terms in the summation all vanish at great distances from the origin.

Substituting in Eq. (19),

$$f(\psi) = \eta r = \psi_{\infty_{rr}} - 1/r\,\psi_{\infty_r} + \sum_n e^{\pm k_n z} \times \left(k_n^2\psi_n' + \psi_{nrr}' - \frac{1}{r}\psi_{nr}'\right) \tag{24}$$

As $|z| \to \infty$, the summation terms vanish, leaving

$$f(\psi_\infty) = \psi_{\infty rr} - (1/r)\psi_{\infty r} \tag{25}$$

In the particular case where $f(\psi)$ is a linear function of ψ, it is possible to separate the variables by subtracting Eq. (25) from Eq. (24) and so solving for ψ_n' and ψ_∞. The case where $f(\psi)$ is a constant will be considered later as part of the second exact solution.

In order to nondimensionalize the equations, the reference length r_t, equal to the annulus outer radius, and the reference velocity c_m are introduced. c_m is defined as the mean axial velocity of the flow, which is constant along the annulus in incompressible flow, and is given by

$$c_m \int_{\text{hub}}^{\text{tip}} 2\pi r\,dr = \int_{\text{hub}}^{\text{tip}} 2\pi r c_z\,dr$$

whence,

$$c_m = -2[\psi]_{\text{hub}}^{\text{tip}}/(r_t^2 - r_h^2) \tag{26}$$

Then, putting $f(\psi) = -\mu^2(\psi/r_t^2)$, where μ is a constant, Eq. (25) becomes:

$$\psi_{\infty rr} - (1/r)\psi_{\infty r} + (\mu^2/r_t^2)\psi_\infty = 0 \tag{27}$$

This has as solution a first-order Bessel function:

$$\psi_\infty/r_t^2 c_m = -R(a/\mu)A_1(\mu R) \tag{28}$$

where $R = r/r_t$ and

$$A_p(\mu R) = J_p(\mu R) + (a'/a)\,Y_p(\mu R)$$

a and a' are constants, but only one is independently variable, for, eliminating c_m from Eqs. (26) and (28),

$$a = \mu(1 - R_h^2)/[A_1(\mu) - R_h A_1(\mu R_h)] \tag{29}$$

where $r_h/r_t = R_h$.

For the perturbation component, subtracting Eq. (25) from Eq. (24) and substituting for $f(\psi)$,

$$\sum e^{\pm k_n z}\left[\psi_{nrr}' - \frac{1}{r}\psi_{nr}' + \left(k_n^2 + \frac{\mu^2}{r_t^2}\right)\psi_n'\right] = 0$$

Omitting subscripts for clarity, it is seen that each term of the summation must satisfy the relation:

$$\psi_{rr}' - (1/r)\psi_r' + [k^2 + (\mu^2/r_t^2)]\psi' = 0$$

Solving and putting

$$\lambda^2 = k^2 r_t^2 + \mu^2 \tag{30}$$

another first-order Bessel function expression is obtained:

$$\psi'/r_t^2 c_m = -R(b/\lambda)B_1(\lambda R) \tag{31}$$

where

$$B_p(\lambda R) = J_p(\lambda R) + (b'/b)\,Y_p(\lambda R) \tag{32}$$

and b and b' are constants of integration. The full solution for the stream function is, therefore, from Eq. (23),

$$\frac{\psi}{r_t^2 c_m} = -\frac{a}{\mu}RA_1(\mu R) - \sum_n e^{\pm k_n z}\frac{b_n}{\lambda_n}RB_1(\lambda_n R) \tag{33}$$

Differentiating and applying Eqs. (12) and (13),

$$c_z/c_m = aA_0(\mu R) + \sum_n e^{\pm k_n z}\,b_n B_0(\lambda_n R) \tag{34}$$

$$c_r/c_m = \mp \sum_n e^{\pm k_n z}(k_n r_t/\lambda_n)b_n B_0(\lambda_n R) \tag{35}$$

From Eqs. (18) and (27),

$$\theta(d\theta/d\psi) = -\eta r = (\mu^2/r_t^2)\psi$$

Integrating,

$$\theta^2 = (\mu^2/r_t^2)\psi^2 + g r_t^2 c_m^2$$

where g is another nondimensional constant of integration. Therefore,

$$\left(\frac{c_\theta}{c_m}\right)^2 = \left(\frac{\mu}{R}\right)^2\left(\frac{\psi}{r_t^2 c_m}\right)^2 + \frac{g}{R^2} =$$

$$\left[aA_1(\mu R) + \sum_n \frac{\mu b_n}{\lambda_n} e^{\pm k_n z} B_1(\lambda_n R)\right]^2 + \frac{g}{R^2} \quad (36)$$

Matching Conditions at Infinity

Putting the perturbation components equal to zero in the Eqs. (33) to (36) for the complete solution derived in the last section, the following conditions at infinity are derived:

$$c_{z\infty}/c_m = aA_0(\mu R) \quad (37)$$

$$(c_{\theta\infty}/c_m)^2 = [(\mu/R)/(\psi_\infty/r_t^2 c_m)]^2 + (g/R^2)$$

$$\psi_\infty/r_t^2 c_m = -(a/\mu)RA_1(\mu R) \quad (38)$$

Three of the constants involved are arbitrary, the fourth being fixed by Eq. (29). It should, therefore, be possible to make a good approximation to any desired velocity distribution at infinity.

A particular case is that of free vortex flow for which c_z and rc_θ are constant—i.e., independent of radius. This condition is satisfied when $a = 1$ and $a' = \mu = 0$, and so $\lambda_n = k_n r_t$. The full solution then becomes:

$$c_z/c_m = 1 + \sum_n e^{\pm \lambda_n(z/r_t)} b_n B_0(\lambda_n R) \quad (39)$$

$$c_r/c_m = \sum_n e^{\pm \lambda_n(z/r_t)} b_n B_1(\lambda_n R) \quad (40)$$

$$(c_\theta/c_m)^2 = g/R^2 \quad \text{or} \quad (rc_\theta)^2 = g(r_t c_m)^2 \quad (41)$$

To illustrate the possibility of matching Eqs. (37) and (38) to a prescribed distribution, a flow in which c_θ varies as the square of the radius has been used, with $c_\theta = c_z$ at the tip and a hub to tip radius ratio of 0.45. The exact equations for this flow at infinity are, denoting tip axial velocity by c_{zt}:

$$c_\theta/c_{zt} = R^2 \quad (42)$$

$$c_z/c_{zt} = \sqrt{(3/2)[(5/3) - R^4]} \quad (43)$$

$$\frac{\psi}{r_t^2 c_{zt}} = -\frac{5}{12}\sqrt{\frac{3}{2}}\sin^{-1}\frac{R^2}{\sqrt{5/3}} - \frac{1}{4}R^2\sqrt{\frac{3}{2}\left(\frac{5}{3} - R^4\right)} \quad (44)$$

where, from Eq. (26),

$$\frac{c_m}{c_{zt}} = \frac{-2}{1 - (0.45)^2}\left(\frac{\psi_{\text{tip}}}{r_t^2 c_{zt}} - \frac{\psi_{\text{hub}}}{r_t^2 c_{zt}}\right) \quad (45)$$

These are plotted against radius ratio as the broken lines in Fig. 2.

Values given by Eqs. (37) and (38) have been fitted to this curve by trial and error. The solid curve shows the result of taking values for the constants of

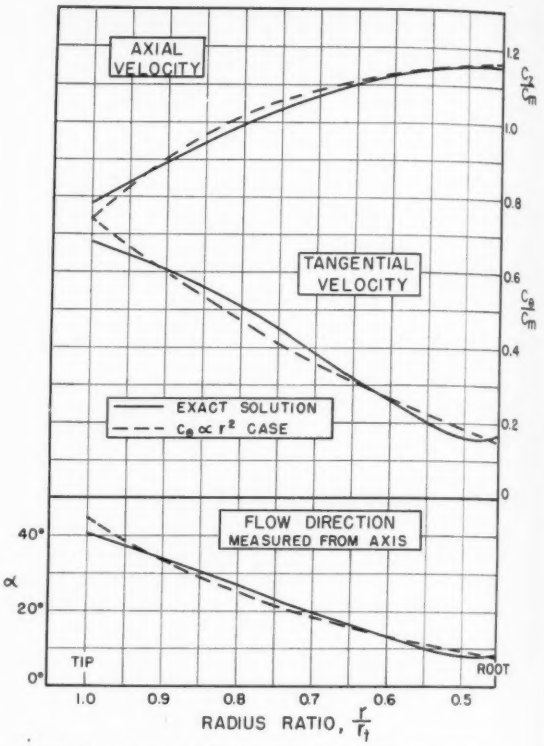

FIG. 2. Velocity distributions at infinity downstream.

$$\mu = 1.740 \qquad a = 1.415$$
$$g = 0.0055 \qquad a' = 0.551$$

There is a slight curl in the rc_θ curve at the inner radius, but agreement is otherwise close, even in such an extreme case as the one chosen.

Matching Conditions at Other Boundaries

The constants b'/b and λ are determined by the boundary conditions at the annular walls, which are assumed parallel. It is required that $c_r = 0$ for $R = R_h$ and $R = 1$ for all values of z. This condition will be satisfied if, from Eq. (35),

$$B_1(\lambda_n) = B_1(\lambda_n R_h) = 0$$

for all values of λ_n. Therefore, from Eq. (32),

$$-\frac{b_n'}{b_n} = \frac{J_1(\lambda_n)}{Y_1(\lambda_n)} = \frac{J_1(\lambda_n R_h)}{Y_1(\lambda_n R_h)} \quad (46)$$

This provides an infinite number of possible values for b'/b and λ. The first six roots may be found in Jahnke and Emde's "Tables of Functions,"[4] and higher roots, if they were required, could be worked out from the approximate formulas:

$$J_1(x) = \sqrt{2/\pi x}\cos[x - (3\pi/4)]$$
$$Y_1(x) = \sqrt{2/\pi x}\sin[x - (3\pi/4)]$$

whence,

$$\tan[\lambda_n - (3\pi/4)] = \tan[\lambda_n R_h - (3\pi/4)]$$

Therefore,

$$\lambda_n = N\pi/(1 - R_h) \tag{47}$$

where N is any integer. Note that, even for a hub:tip radius ratio as small as 0.5, the lowest value of λ_n is about 6. The corresponding values of k_n are obtained from Eq. (30).

Only the values of the constants b are now unknown, and these depend on matching at the blade rows. If upstream and downstream flows are both defined by solutions of our form, exact matching may be obtained in the limiting case of an actuator disc. At the disc, continuity in radial and axial velocities is required at all radii, but there may be discontinuities in tangential components. If the disc is situated for convenience at $z = 0$, exact matching of the c_r values will be obtained from Eq. (35) if

$$k_{nd}b_{nd} = -k_{nu}\, b_{nu} = k_{bn} \tag{48}$$

where suffixes u and d denote upstream and downstream conditions, respectively.

Matching of the axial velocities is obtained from Eqs. (34) and (37) if

$$\sum_n \left(\frac{k_{bn}}{k_{nd}} + \frac{k_{bn}}{k_{nu}}\right) B_0(\lambda_n R) = \left(\frac{c_{z\infty}}{c_m}\right)_u - \left(\frac{c_{z\infty}}{c_m}\right)_d \tag{49}$$

It is now possible to find k_b and the other coefficients by a method analogous to that employed in determining those of a Fourier series. Multiplying both sides of Eq. (49) by $RB_0(\lambda_m R)dR$ and integrating from hub to tip, we find that all terms on the left-hand side for which $m \neq n$ are zero. Performing the integration for $m = n$ and making substitutions for $c_{z\infty}$ from Eq. (37), we obtain the following expression for k_{bn}:

$$\frac{1}{2}k_{bn}\left(\frac{1}{k_{nd}} + \frac{1}{k_{nu}}\right) r_t^2\, [B_0^2(\lambda_n) - R_h^2 B_0^2(\lambda_n R_h)] =$$

$$(a_d\mu_d/k_{nd}^2)[A_1(\mu_d)B_0(\lambda_n) - R_h A_1(\mu_d R_h)B_1(\lambda_n R_h)] -$$

$$(a_u\mu_u/k_{nu}^2)\, [A_1(\mu_u)B_0(\lambda_n) - R_h A_1(\mu_u R_h)B_1\,(\lambda_n R_h)] \tag{50}$$

This fixes all the coefficients in the series expansion, and thus the flow with given conditions at infinity up- and downstream is fully determined everywhere.

One case is of special interest. If $\mu_u = \mu_d$, then $k_{nu} = k_{nd}$, $-b_{nu} = b_{nd}$, and Eq. (34) reduces to

$$\left(\frac{c_z}{c_m}\right)_{\text{disc}} = \left(\frac{c_{z\infty}}{c_m}\right)_d + \sum_n b_{nd}B_0(\lambda_n R) = \left(\frac{c_{z\infty}}{c_m}\right)_u -$$

$$\sum_n b_{nd}B_0(\lambda_n R) = \frac{1}{2}\left[\left(\frac{c_{z\infty}}{c_m}\right)_d + \left(\frac{c_{z\infty}}{c_m}\right)_u\right] \tag{51}$$

that is, the axial velocity at the disc is exactly the arithmetic mean of those at the same radius upstream and downstream at infinity.

If μ^2 is small compared with λ_1^2, it will be extremely small compared with higher order λ_n values. Thus,

$$k_{nu}r_t \simeq \lambda_n \simeq k_{nd}r_t$$

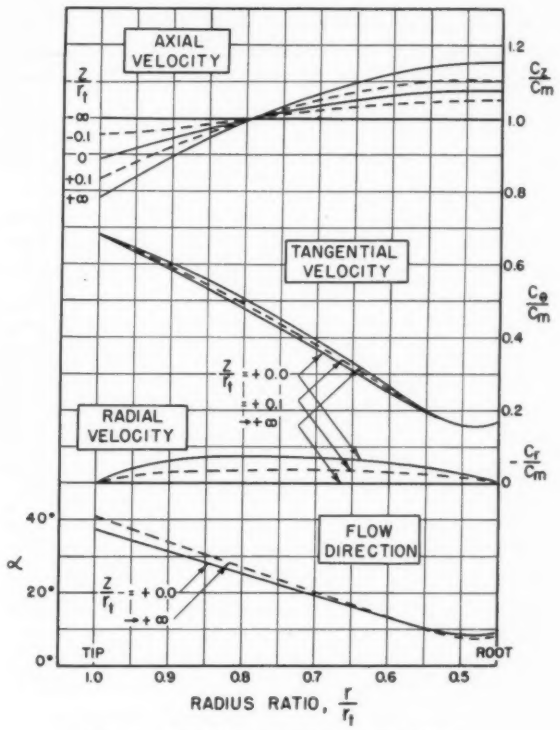

FIG. 3. Conditions near the actuator disc.

which again gives the result of Eq. (51). It seems likely that this relation will hold in many practical cases, so that, in general, the axial velocity at the disc will be almost exactly the arithmetic mean of the infinity values at the same radius.

On the other hand, $\psi = \psi_\infty$ at root and tip radii and is little different elsewhere due to the $1/\lambda_n$ factor in the coefficients of the series expansion [Eq. (33)]. Then Eq. (36) shows that there will be only a small difference at a given radius between the tangential velocity just downstream of the actuator disc and the corresponding infinity value.

To illustrate the application of the method, a flow that is axial and vortex-free upstream at infinity has been matched at the actuator disc to the approximate c_θ varying as r^2 example downstream at infinity already mentioned (shown as solid curves in Fig. 2). The first six roots of Eq. (46) for $R_h = r_h/r_t = 0.45$ are:

λ_n	5.843	11.495	17.22	22.90	28.6	34.3
b_n'/b_n	−2.31	3.86	0.89	0.126	−0.488	−1.69

and these give, with Eqs. (48) and (50),

b_{nu}	0.0818	−0.0166	−0.0230	−0.0265	−0.0155	−0.0070
b_{nd}	0.0856	−0.0167	−0.0230	−0.0265	−0.0155	−0.0070

The calculated values of c_r/c_m and c_z/c_m at the actuator disc and c_θ/c_m just downstream are shown in Fig. 3. The values of c_z/c_m at the disc are almost exactly the arithmetic mean of upstream and downstream infinity values. Because of the large difference between the axial velocity distributions at infinity on either side

of the disc, the radial velocities are high—up to 8 per cent of the mean axial velocity. Since rc_θ is constant along a stream line and the radial velocities are inflows, the tangential velocities at the disc are less than those at the same radii at infinity downstream, except at the hub and tip where, the radial velocities being zero, no change occurs in c_θ/c_m.

The angle of flow, α, is also plotted. The effects mentioned above tend, in this case, to increase the angle at the tip and reduce it at the root as the flow moves downstream. An approximation suggested for rough design work was to calculate the flow angles near the disc using the mean axial velocity of upstream and downstream flows and the downstream infinity value of the tangential velocity. This result is also shown on Fig. 4; it appears that this is a better approximation to use than the downstream infinity values of the flow angles, especially at the root and tip.

Velocity values at $z = \pm 0.1 r_t$ are also shown, and it may be seen that these are about midway between disc and infinity values. This demonstrates that the decay rate of the perturbation components is rapid as the fluid moves away from the blades.

Except in the expression for c_z/c_m, the series for the perturbation velocity components converges rapidly. Six terms were actually calculated so that c_r/c_m and c_θ/c_m might be accurately known. The values obtained by taking only two terms in the expansion are compared with the more accurate calculation on Fig. 4, and it may be seen that the added refinement is unnecessary, especially since the exponential $e^{\pm k_n z}$ soon kills high-order terms away from the disc. The error involved in using Eq. (51) to calculate c_z/c_m cannot be more than half the difference in the first series term—i.e., more than 0.002 in this case—since all the other series terms are virtually identical upstream and downstream.

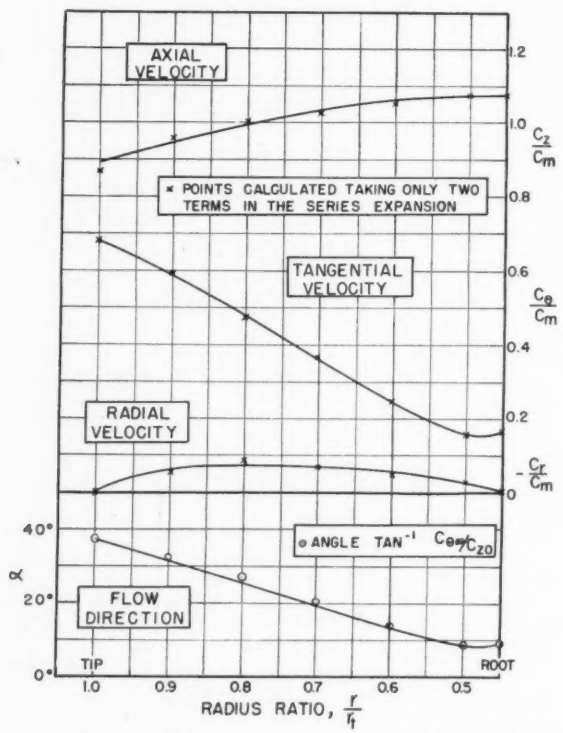

FIG. 4. Comparison of exact with approximate solutions just downstream of the actuator disc.

THE SECOND EXACT SOLUTION

Returning to the generalized equation for incompressible flow, Eq. (18),

$$dH/d\psi = (1/r^2)[\theta(d\theta/d\psi) + \eta r]$$

suppose that ηr is a function of r only. Differentiating with respect to z,

$$\frac{d^2H}{d\psi^2}\frac{\partial\psi}{\partial z} = \frac{1}{r^2}\frac{d^2[(1/2)\theta^2]}{d\psi^2}\frac{\partial\psi}{\partial z}$$

Since ψ is a function of r and z, this equation can only be satisfied everywhere if

$$d^2H/d\psi^2 = d^2(\theta^2)/d\psi^2 = 0$$

Integrating and again using nondimensional constants,

$$\frac{dH}{d\psi} = \frac{a_1 c_m}{r_t^2} \quad \therefore \quad \frac{H}{c_m^2} = a_1\frac{\psi}{c_m r_t^2} + a_3 \tag{52}$$

$$\theta\frac{d\theta}{d\psi} = a_2 c_m \quad \therefore \quad \left(\frac{rc_0}{r_t c_m}\right)^2 = 2a_2\frac{\psi}{c_m r_t^2} + a_4 \tag{53}$$

Substituting the above into Eqs. (18) and (19),

$$\psi_{zz} + \psi_{rr} - (1/r)\psi_r = \eta r = c_m(a_1 R^2 - a_2) \tag{54}$$

Suppose, as before, that

$$\psi = \psi_\infty + \sum_n e^{\pm k_n z}\psi_n' \tag{23}$$

Then

$$c_m(a_1R^2 - a_2) = \psi_{\infty rr} - (1/r)\psi_{\infty r} + \sum_n e^{\pm k_n z}[k_n^2\psi_n' + \psi_{nrr}' - (1/r)\psi_{nr}']$$

For this to be satisfied everywhere,

$$k_n^2\psi_n' + \psi_{nrr}' - \frac{1}{r}\psi_{nr}' = 0$$

Putting $\lambda_n = k_n r_t$, the solution for ψ' has exactly the same form as in the case previously considered—Eq. (31). Also,

$$c_m[a_1(R)^2 - a_2] = \psi_{\infty rr} - (1/r)\psi_{\infty r}$$

may be solved to give

$$\frac{\psi_\infty}{r_t^2 c_m} = \frac{a_1}{8}R^4 - \frac{a_2}{4}R^2(2\log_e R - 1) - \frac{a_5}{2}R^2 \tag{55}$$

a_5 is another constant of integration, but it is not independent of the others, being fixed by Eq. (26). Eqs.

(23), (31), (52), (53), and (55) comprise full solutions for the flow.

By differentiation, using the relations (12) and (13),

$$\frac{c_r}{c_m} = \sum_n \mp b_n e^{\pm \lambda_n z/r_t} B_1(\lambda_n R) \tag{56}$$

$$\frac{c_z}{c_m} = -\frac{a_1}{2} R^2 + a_5 + a_2 \log_e R + \sum_n e^{\pm \lambda_n z/r_t} b_n B_0(\lambda_n R) \tag{57}$$

The vorticity components are then given by Eq. (54) and

$$r\xi = -a_2(c_r c_m/c_\theta) \tag{58}$$

$$r\zeta = -a_2(c_z c_m/c_\theta) \tag{59}$$

We now have a second full solution, with, as before, three constants to determine the velocity distribution at infinity plus an additional constant a_1, since variation in stagnation conditions is permitted. The perturbation effects may be treated in exactly the same way as in the first case, the values of λ depending only on the hub : tip ratio and the values of b being fixed by matching at the actuator disc.

In matching two flows of this kind, the axial velocities at the disc will be exactly halfway between the infinity values at the same radii for reasons similar to those given in discussing the case of $\mu_u = \mu_d$ in the last section. This might be explained physically by considering the flow to be caused by sheets of vortices shed by the blades that constitute the disc. Only the tangential component or ring component of these vortices will affect the axial velocity at the disc, and, since the strength of the vortex ring component at a given radius is the same everywhere, the net effect at the disc must be exactly half the effect at infinity.

For constant stagnation enthalpy throughout the flow, $a_1 = 0$, and thus Eq. (54) reduces to

$$\eta r = -a_2 c_m$$

which is constant. This is a limiting case of the H = constant flows mentioned in the first section of the paper.

Types of flow with rc_θ = constant are obtained when $a_2 = 0$; then Eq. (54) becomes

$$\eta/r = a_1 c_m/r_t^2$$

which is constant, and

$$c_{z_\infty}/c_m = a_5 - (1/2)a_1 R^2 \tag{60}$$

representing a limiting case of the flows with rc_θ = constant and η/r constant along a stream line discussed earlier.

Although the tangential velocity distribution is the same as free vortex in this flow, the axial velocity is not the same because of the variation in stagnation enthalpy with radius. The vorticity at a given radius is constant, and the flow consists of trailing "smoke ring" vortices traveling along the stream surfaces, but the stream lines do not follow the vortex lines.

From Eqs. (52) and (53),

$$\frac{H}{{c_m}^2} = \left(a_3 - \frac{a_1 a_4}{2a_2}\right) + \frac{a_1}{2a_2}\left(\frac{rc_\theta}{r_t c_m}\right)^2 \tag{61}$$

Now the change in H along a stream line passing through a rotor is proportional to the change in rc_θ. Since rc_θ does not enter linearly into Eq. (61), it is not possible to use this equation for flows both upstream and downstream of a rotor. Hence, for flow through a rotor, these solutions are restricted to cases for which H = constant.

No numerical examples are shown for this second exact solution.

References

[1] Meyer, Richard E., *Beitrag zur Theorie feststehender Shaufelgitter*, Mit. Inst. Aerodynamik E.T.H. Zürich, 1946.

[2] Marble, Frank E., *Flow of a Perfect Fluid Through an Axial Turbomachine with Prescribed Blade Loading*, Journal of Aeronautical Sciences, Vol. 15, No. 8, p. 473, August, 1948.

[3] Lamb, Sir Horace, *Hydrodynamics*, 6th Ed.; Cambridge University Press, 1936.

[4] Jahnke, E., and Emde, F., *Tables of Functions*, 4th Ed.; Dover, 1945.

[5] Crocco, L., *Eine neue Stromfunction fur die Erforschung der Bewegung der Gase mit Rotation*, Zeitschrift. ang. Math. und Mech. 17, 1–7, 1937.

Readers' Forum

BRIEF REPORTS of investigations in the aeronautical sciences and discussions of papers published in the JOURNAL are presented in this special department. The publication will be completed approximately 8 weeks after receipt of the material. The Editorial Committee does not hold itself responsible for the opinions expressed by the correspondents. Contributions should not exceed 800 words in length.

Remarks on the Interaction Between Parallel Streams of Subsonic and Supersonic Velocities

Mac C. Adams
Langley Aeronautical Laboratory, N.A.C.A., Langley Air Force Base, Va.
January 3, 1950

IN A RECENT PAPER, Tsien and Finston[1] presented an elegant treatment of the interaction between parallel supersonic and subsonic streams.

For the case of the inclined wall in the subsonic region, there appears to be a possible error in the calculation of the pressure at the interface, Eqs. (54) and (55) of the reference.

One might obtain the results for the inclined wall in the following manner:

Using the notation of reference 1, the subsonic potential for the configuration shown in Fig. 1 can be written

$$\varphi_2 = \frac{\delta}{b}\frac{U_2}{\sqrt{1-M_2^2}}\frac{1}{\sigma\pi}\int_0^\infty \sinh\lambda\sqrt{1-M_2^2}(y+b)\times(\sin\lambda\sigma b\cos\lambda x)\frac{d\lambda}{\lambda^2} + U_2\int_0^\infty \cosh\lambda\sqrt{1-M_2^2}(y+b)\times[a_2(\lambda)\sin\lambda x + b_2(\lambda)\cos\lambda x]d\lambda \quad (1)$$

The inclination of the flow at the wall is then given by

$$\left(\frac{v_2}{U_2}\right)_{y=-b} = \frac{\delta}{\sigma b\pi}\int_0^\infty \sin\lambda\sigma b\cos\lambda x\,\frac{d\lambda}{\lambda} = \frac{\delta}{2\sigma b}\,[1(x+\sigma b) - 1(x-\sigma b)] \quad (2)$$

Now, if $\sigma \to 0$, Eq. 2 will give the unit impulse function—i.e., the limiting process gives a unit source on the boundary with a vertical velocity on the boundary of infinity at $x = 0$ and zero elsewhere. The condition corresponds to a step on the wall. Certainly such a boundary condition is too severe for the limitations of the linearized theory; however, distribution of these steps would lead to solutions for an arbitrary boundary shape. For the case of the inclined wall, a uniform distribution is necessary.

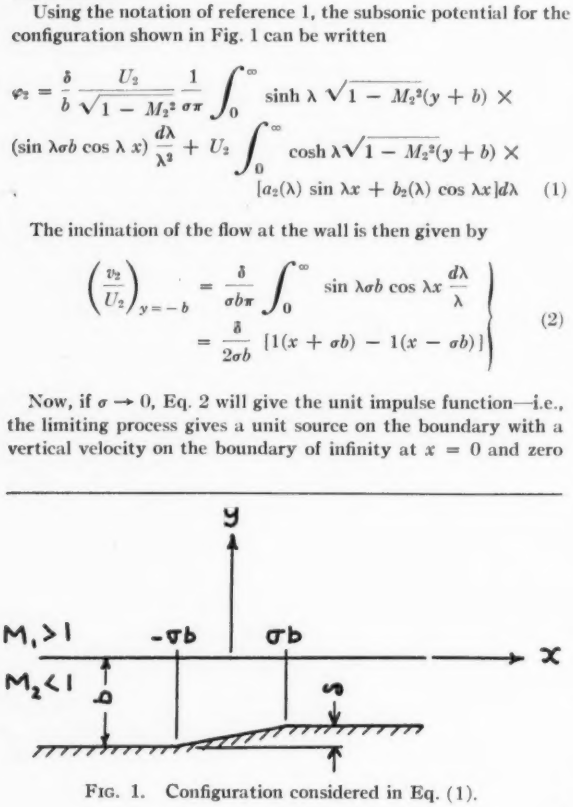

FIG. 1. Configuration considered in Eq. (1).

Proceeding in a manner identical with that of reference 1, the solution for the stepped boundary gives, for the pressure at the interface,

$$\frac{(\Delta p)_i^*}{(1/2)\rho_1 U_1^2} = \frac{\delta\cos(\theta/2)}{b\sqrt{(1-M_2^2)(M_1^2-1)}}\frac{e^{-\xi(\theta/\pi)}}{\cosh\xi} \quad (3)$$

Now, integrating with respect to x leads to the solution for the inclined wall, where the quantity δ is replaced by the wall angle ϵ. This results in

$$\frac{(\Delta p)_i^*}{(1/2)\rho_1 U_1^2} = \frac{2\epsilon}{\sqrt{M_1^2-1}}\left[1 - 2\cos\frac{\theta}{2}\,F_2(\xi;\,\theta)\right], \quad \xi > 0 \quad (4)$$

$$\frac{(\Delta p)_i^*}{(1/2)\,\rho_1 U_1^2} = \frac{4\epsilon}{\sqrt{M_1^2-1}}\cos\frac{\theta}{2}\,F_4(\xi;\,\theta), \quad \xi < 0 \quad (5)$$

One might further suspect an error in reference 1 from the fact that negative pressures occur at certain points along the interface, Fig. 10 of the reference.

REFERENCE

[1] Tsien, H. S., and Finston, M., *Interaction Between Parallel Streams of Subsonic and Supersonic Velocities*, Journal of the Aeronautical Sciences, Vol. 16, No. 9, pp. 515–528, September, 1949.

The Extension of the Prandtl-Glauert Rule

E. V. Laitone
Associate Professor, University of California, Berkeley, Calif.
January 25, 1950

THE APPLICATION OF THE Prandtl-Glauert Rule to three-dimensional flow and wind-tunnel wall effects has finally reached a satisfactory agreement in each case. An examination of most of the work prior to 1946[1–3] indicates the inherent difficulties, mainly in not satisfying the proper boundary conditions and erroneous conclusions in applying the Prandtl-Glauert Rule. By carefully considering the boundary conditions, the correct compressibility correction factors were finally obtained by Gothert and others.[4–9] I believe the simplest rigorous derivation is the one I gave in references 7 and 8. In addition, this method permits a direct evaluation of the actual velocity distributions on or about slender bodies. There has been some criticism of this proof because the perturbation potential was in the form described as Method I by Goldstein and Young.[1] However, the correct boundary conditions were used in each case so the same correct answer would be obtained independent of the choice of any constant factor multiplying the perturbation potential. For clarity and completeness, however, I should like to present the following as being the simplest rigorous approach:

(1) BODY OF REVOLUTION

The linearized potential equation for compressible flow with axial symmetry is

$$\beta^2\phi_{xx} + \phi_{rr} + (1/r)\phi_r = 0 \quad (1)$$

where for subsonic flow

$$\beta = \sqrt{1-M^2}$$

and the fundamental potential for a source of strength F located at the point ξ on the x axis and satisfying Eq. (1) is

$$\phi(x, r) = -(F/4\pi)\left\{1/[(x-\xi)^2 + (\beta r)^2]^{1/2}\right\}$$

Then, for a continuous distribution of sources along the x axis from $x = 0$ to $x = L$, we have

$$\phi(x, r) = -\frac{1}{4\pi}\int_0^L \frac{f(\xi)\,d\xi}{[(x-\xi)^2 + (\beta r)^2]^{1/2}} \tag{2}$$

The boundary condition to be satisfied at the body surface is

$$r_0' = \phi_r/(U + \phi_x) = (\phi_r/U) + 0(\phi_r\phi_x) \tag{3}$$

Eqs. (2) and (3) can be combined as

$$Ur_0' \approx \phi_r = \frac{\beta^2 r}{4\pi}\int_0^L \frac{f(\xi)\,d\xi}{[(x-\xi)^2 + (\beta r)^2]^{3/2}} = \frac{f(x)}{2\pi r} - \beta^2 f''(x)\, r \ln\frac{r}{L} + 0(r) \tag{4}$$

where the expansion of the integral expression is obtained by means of a Taylor series, as shown in reference 7. Therefore, we have

$$f(x) = 2\pi r_0 r_0' U + 0(r_0^4 \ln r_0) = US'(x) + 0(r_0^4 \ln r_0) \tag{5}$$

where $S = \pi r_0^2$ is the cross-sectional area of the body of revolution and the remainder term is exact only in the limit as β approaches unity. It is seen that, at least to the first order, the required source strength for a given body shape is independent of compressibility effects, but the resulting velocities in compressible flow are greater, as shown by combining Eqs. (2) and (5). For example, the total velocity component in the direction of the x axis, for any point on or about the body, is

$$u(x, r) = U + \phi_x = U\left\{1 + \frac{1}{4\pi}\int_0^L \frac{(x-\xi)S'(\xi)\,d\xi}{[(x-\xi)^2 + (\beta r)^2]^{3/2}}\right\} \tag{6}$$

which is the same correct result as given in reference 7.

It is seen from Eq. (6) that the first-order wind-tunnel wall correction in compressible flow would vary as $1/\beta^2$ for a body of revolution, since, for $r \gg (x - \xi)$,

$$u = U\left[1 + \frac{1}{4\pi r^2\beta^2}\int_0^L (x-\xi)S'(\xi)\,d\xi\right] \tag{7}$$

As shown in reference 7, the surface pressure coefficient on the body of revolution is given by

$$C_p[x, r_0(x)] = -2\frac{\phi_x}{U} - (r_0')^2 + 0(r_0^4 \ln r_0) = \frac{1}{2\pi}\int_0^L \frac{(\xi - x)S'(\xi)\,d\xi}{[(\xi-x)^2 + (\beta r_0)^2]^{3/2}} - (r_0')^2 + 0(r_0^4 \ln r_0) \tag{8}$$

where, again, the remainder term is exact only in the limiting case as β approaches unity. In this case, corresponding to incompressible flow, Eq. (8) provides a satisfactory solution for the pressure distribution on either a sharp or founded nose body of revolution, provided the thickness ratio is less than 10 per cent. As shown in reference 7, we may expand Eq. (8) by means of a Taylor series to show that at any point on the surface of a symmetrical body of revolution the first-order compressibility effects are given by

$$C_{P_M} \approx C_{P_0} - (S''(x)/\pi)\ln\beta \tag{9}$$

This shows that the compressibility correction for a body of revolution is affected by the body shape as well as the selected location on a given body.

(2) Two-Dimensional Profile

A similar analysis is easily made for two-dimensional flow.[8] In this case the linearized potential equation for compressible flow is

$$\beta^2\phi_{xx} + \phi_{yy} = 0 \tag{10}$$

so, for a continuous source distribution along the x axis from $x = 0$ to $x = C$, the potential satisfying Eq. (10) is

$$\phi(x, y) = \frac{1}{2\pi}\int_0^C f(\xi)\ln\sqrt{(x-\xi)^2 + (\beta y)^2}\,d\xi \tag{11}$$

and the boundary condition on the profile surface is

$$y_0' = \phi_y/(U + \phi_x) = (\phi_y/U) + 0(\phi_y\phi_x) \tag{12}$$

Therefore

$$Uy_0' \approx \phi_y = \frac{\beta^2 y}{2\pi}\int_0^C \frac{f(\xi)\,d\xi}{(x-\xi)^2 + (\beta y)^2} = \frac{1}{2}\beta f(x) + 0(y^2)$$

so that

$$f(x) = (2U/\beta)y_0'(x) + 0(y^2) \tag{13}$$

It is seen that now the source strength used for incompressible flow must be increased by $1/\beta$ in order to represent the same profile in a compressible flow.

Combining Eqs. (11) and (13), we derive the expression for the total velocity component in the x direction for any point on or about the body as

$$u(x, y) = U\left[1 + \frac{1}{\pi\beta}\int^C \frac{(x-\xi)y_0'(\xi)\,d\xi}{(x-\xi)^2 + (\beta y)^2}\right] \tag{14}$$

Again, the first-order wind-tunnel wall compressibility correction would vary as $1/\beta^2$, since, for $y \gg (x - \xi)$,

$$u = U\left[1 + \frac{1}{\pi y^2\beta^3}\int_0^C (x-\xi)y_0'(\xi)\,d\xi\right] \tag{15}$$

However, on the body or along the stream line leading to the stagnation point, the compressibility correction varies as $1/\beta$, since, for $y \approx 0$,

$$u = U\left[1 + \frac{1}{\pi\beta}\int_0^C \frac{y_0'(\xi)\,d\xi}{x-\xi}\right] \tag{16}$$

It must be noted that for u values *on the profile* the denominator vanishes when $\xi = x$, so the Cauchy principal value of the integral must be used. In this case, Eq. (16) provides a satisfactory surface pressure distribution for sharp nose profiles less than 10 per cent thick as

$$C_p = -\frac{2\phi_x}{U} = \frac{2}{\pi\beta}\left[\lim_{\epsilon\to 0}\int_0^{x-\epsilon} + \int_{x+\epsilon}^C \frac{y_0'(\xi)d\xi}{\xi - x}\right] \tag{17}$$

For rounded-nose profiles, it is necessary to use Eq. (14) for a satisfactory solution.

References

[1] Goldstein, S., and Young, A. D., *The Linear Perturbation Theory of Compressible Flow with Applications to Wind Tunnel Interference*, British A.R.C., R & M 1909, July, 1943.

[2] Thom, A., *Blockage Corrections in a Closed High-Speed Tunnel*, British A.R.C., R & M 2033, November, 1943.

[3] Tsien, Hsue-Shen, and Lees, Lester, *The Glauert-Prandtl Approximation for Subsonic Flows of a Compressible Fluid*, Journal of the Aeronautical Sciences, Vol. 12, No. 2, pp. 173–187, April, 1945.

[4] Gothert, B., *Plane and Three-Dimensional Flow at High Subsonic Speeds*, N.A.C.A. T.M. No. 1105, October, 1946.

[5] Lees, Lester, *A Discussion of the Application of the Prandtl-Glauert Method to Subsonic Compressible Flow over a Slender Body of Revolution*, N.A.C.A. T.N. No. 1127, September, 1946.

[6] Sears, W. R., *A Second Note on Compressible Flow about Bodies of Revolution*, Quarterly of Applied Mathematics, Vol. 5, No. 1, pp. 89–91, April, 1947.

[7] Laitone, E. V., *The Subsonic Axial Flow about a Body of Revolution*, Quarterly of Applied Mathematics, Vol. 5, No. 2, pp. 227–331, July, 1947.

[8] Laitone, E. V., *The Subsonic and Supersonic Two Dimensional Flow Fields about Slender Bodies*, Cornell Aeronautical Laboratory Publication No. 6, July, 1946.

[9] Young, A. D., *On the Compressibility Correction Factor for Axially Symmetric Bodies*, Readers' Forum, Journal of the Aeronautical Sciences, Vol. 16, No. 11, p. 703, November, 1949.

Stability of Alclad Plates

P. P. Bijlaard
Professor, Institute of Technology, Delft, Holland, on leave, Associate Professor, Cornell University, Ithaca, N.Y.
January 21, 1950

IN REFERENCE 1, the stability of Alclad plates, consisting of a core of high-strength aluminum alloy which is covered on each side with a coating of almost pure aluminum of very low strength, is investigated. The differential equation for the plates is derived, starting from stress-strain relations given by Ilyushin. The latter relations were derived from the present writer's exact theory[2] by making the assumption that for the elastic deformation Poisson's ratio is 0.5. Although this assumption does not cause much discrepancy with pure compression, it proves to give discrepancies from 20 to 30 per cent in the plastic reduction factor η in case of biaxial compression. This follows directly by inserting in the present writer's stress-strain relations (21) or (21a) in reference 2, with $\beta = \rho_2/\rho_1 = 1$, a value $\nu = 0.5$ instead of the actual value of about 0.3.

Moreover, it is easy to write down directly the differential equation of Alclad plates from the differential equation for homogeneous plates,[2]

$$EI\left[A\frac{\partial^4 w}{\partial x^4} + 2(B + 2F)\frac{\partial^4 w}{\partial x^2 \partial y^2} + D\frac{\partial^4 w}{\partial y^4}\right] + N_x\frac{\partial^2 w}{\partial x^2} + N_y\frac{\partial^2 w}{\partial y^2} = 0 \quad (1)$$

where the axes are assumed in the directions of the principal stresses ρ_1 and ρ_2 by which the plate is loaded, while $N_x = h\rho_1$ and $N_y = h\rho_2$.

The last two terms to the left in Eq. (1) refer to the deflecting forces exerted on a plate element by the compression forces N_x and N_y and consequently they remain the same for the Alclad plate. The first term to the left, however, refers to the restraining force given by the transverse shearing forces. In the Alclad plate this term will consist of the sum of the pertinent terms for core and coating. With a core thickness h and a thickness ah of each coating, the moments of inertia of core and coating are $h^3/12$ and $[(1 + 2a)^3 - 1]h^3/12 = gh^3/12$, respectively. Hence, the differential equation of the Alclad plate becomes

$$EI_c\left[A_a\frac{\partial^4 w}{\partial x^4} + 2(B_a + 2F_a)\frac{\partial^4 w}{\partial x^2 \partial y^2} + D_a\frac{\partial^4 w}{\partial y^4}\right] + N_x\frac{\partial^2 w}{\partial x^2} + N_y\frac{\partial^2 w}{\partial y^2} = 0 \quad (2)$$

in which

$$I_c = h^3/12, \quad A_a = A_c + gA_f$$
$$B_a = B_c + gB_f, \quad D_a = D_c + gD_f$$
$$F_a = F_c + gF_f$$

The subscripts a, c, and f refer to Alclad plate, core, and coating (faces), respectively. In the elastic domain

$$A_a = D_a = B_a + 2F_a = (1 + g)/(1 - \nu^2)$$

For a plate that is compressed in longitudinal direction and simply supported at the unloaded sides (Case 2 in reference 2), where for a homogeneous plate the plasticity reduction factor is (reference 2, Table 5):

$$\eta = \frac{\sigma_B}{\sigma_E} = \frac{\sqrt{AD} + B + 2F}{2/(1 - \nu^2)} = 0.455\,(\sqrt{AD} + B + 2F)$$

it follows immediately that, for the Alclad plate,

$$\eta = \frac{\sqrt{A_aD_a} + B_a + 2F_a}{2(1 + g)/(1 - \nu^2)} = \frac{0.455}{1 + g}\,(\sqrt{A_aD_a} + B_a + 2F_a) \quad (3)$$

In the same way the formulas for $\eta = \sigma_B/\sigma_E$ in Table 5 of reference 2 for Cases 1, 4, 13, 6, and 9 are valid for Alclad plates if all values A, B, D, and F are given the subscript a and all values σ_B/σ_E are divided by $(1 + g)$.

References

[1] Buchert, K. P., *Stability of Alclad Plates*, N.A.C.A. T.N. No. 1986, December, 1949.

[2] Bijlaard, P. P., *Theory and Tests on the Plastic Stability of Plates and Shells*, Journal of the Aeronautical Sciences, Vol. 16, No. 9, pp. 529-541, September, 1949.

Another Note on the Velocity of Sound

C. B. Millikan
Director, Guggenheim Aeronautical Laboratory, California Institute of Technology, Pasadena, Calif.
January 14, 1950

IN A RECENT NOTE,[1] Morduchow attempts to show that "the well-known differential expression $a^2 = dp/d\rho$ for the velocity of sound cannot, as is sometimes attempted, be rigorously derived from the steady one-dimensional differential equations of nonviscous flow." Unfortunately, his reasoning is faulty and his erroneous conclusion is likely to confuse unnecessarily the many students who have correctly derived this expression by the procedure he believes to be incorrect.

The three basic equations of the problem may be written, in a form slightly different from that used by Morduchow, as follows:

$$du^2 = -(2/\rho)u^2 d\rho$$
$$du^2 = -(2/\rho)dp$$
$$du^2 = -[2\gamma/(\gamma - 1)]d(p/\rho)$$

where the gas is assumed to follow the perfect gas law. If we can find the conditions under which these equations are consistent, then these conditions will correspond to a one-dimensional steady flow in which u, p, and ρ have constant values on either side of a discontinuity across which there are infinitesimal discontinuities du, dp, and $d\rho$. The ratios $dp/d\rho$, $du/d\rho$, etc., are meaningless (mathematically 0/0) except at the discontinuity where they are well defined.

For the second and third equations to be compatible we must have $dp/\rho = [\gamma/(\gamma - 1)]d(p/\rho)$, from which immediately follows $p/\rho^\gamma = \text{const}$. This tells us that the gas flows isentropically across the discontinuity; thus, the entire flow is isentropic. For the first and second equations to be consistent we must have $u^2 = dp/d\rho$, and combining this with the condition of isentropy, we find $u^2 = \gamma(p/\rho)$.

Thus, the condition for the existence of a stationary infinitesimal discontinuity in a one-dimensional flow with velocity u is

$$u^2 = dp/d\rho = \gamma(p/\rho)$$

and this velocity we define as the velocity of sound, a. Morduchow is led to what he calls a contradiction by taking the differential of this relation, obtaining $du^2 = \gamma d(p/\rho)$. This is obviously inconsistent with the third of our original equations (unless $\gamma = -1$). But the relation $u^2 = \gamma(p/\rho)$ is not a general functional relation between u, p, and ρ which holds for all values of these variables. It merely gives a specific relation between them which must be satisfied for a stationary discontinuity to be possible. Accordingly, the relation cannot be differentiated and the expression $du^2 = \gamma d(p/\rho)$ is meaningless and incorrect. The simple "steady-motion" derivation of $a^2 = dp/d\rho$, which has seen such yeomen service, seems to be respectable after all.

Reference

[1] Morduchow, Morris, *A Note on the Velocity of Sound*, Readers' Forum, Journal of the Aeronautical Sciences, Vol. 16, No. 10, p. 635, October, 1949.

On Downwash Corrections in Unsteady Flow*

John W. Miles
Department of Engineering, University of California at Los Angeles
December 16, 1949

STATLER[1] HAS STATED that the most important unsteady flow effect in the calculation of dynamic stability derivatives generally may be identified as the "complex downwash lag" factor, which will enter in the determination of wing-tail interference. While we have taken exception to the generality of his conclusions,[2] it does appear that the downwash lag will be important, and we wish to advance here a simple method for its calculation.

Assuming the harmonic time deepndence exp ($i\omega t$), the velocity potential (ϕ) at the upper and lower surfaces of the vortex sheet behind a plane wing must exhibit a dependence on the streamwise coordinate (x, positive downstream) which will ensure continuity of the pressure. If we assume that the vortex sheet remains in the plane of the wing ($z = 0$), this requirement is satisfied by taking

$$\phi(x, y, 0 \pm) = \pm\phi_1(y) \exp\left\{-ik\left[\frac{x - x_1(y)}{b}\right]\right\} \tag{1}$$

$$k = \omega b/U \tag{2}$$

where U is the freestream velocity, b is a reference length, y is the spanwise coordinate, $x_1(y)$ is the coordinate of the trailing edge, $\phi(x, y, z)$ is the velocity potential, and $\phi_1(y)$ is the value of this potential at the trailing edge of the upper surface. Calculating the pressure at the wing and evaluating the section lift and moment (about $x = 0$) coefficients (c_l and c_m), we find

$$\phi_1(y) \exp\left[ikx_1(y)/b\right] = \frac{1}{4} U\left[c_l(y) - \frac{ikc(y)c_m(y)}{b}\right] \tag{3}$$

c_l and c_m are referred to c and c^2, respectively, where c is the chord. Now, if $c_{l_k}(y)$ represents the lift coefficient calculated in the absence of unsteady flow effects and $\phi_0(y, 0 \pm)$ the corresponding velocity potential at the vortex sheet, we may write (assuming k to be small)

$$c_l(y) - (ikc(y)c_m(y)/b) = c_{l_0}(y) \exp\left[ik\delta(y)\right] \tag{4}$$

$$\phi(x, y, 0 \pm) = \phi_0(y, 0 \pm) \exp\left\{ik[\delta(y) - (x/b)]\right\} \tag{5}$$

Having the potential $\phi(x, y, 0 \pm)$, the calculation of $\phi(x, y, z)$ is reduced to a classical boundary value problem. In principle, the solution of this problem is straightforward, but, in practice, it is likely to prove cumbersome; moreover, the introduction of such important factors as viscosity and warping of the vortex sheet leads to even more serious complications. However, if $\epsilon_0(x, y, z)$ represents the downwash field in the absence of unsteady flow effects but including experimentally or empirically determined corrections, it appears reasonable to assume that the downwash field in unsteady flow, at locations not too remote from the vortex sheet, may be approximated by

$$\epsilon(x, y, z) = \epsilon_0(x, y, z) \exp\left\{ik[\delta(y) - (x/b)]\right\} \tag{6}$$

Consider now the application of the result (6) to a pitching oscillation of amplitude α_0 about the axis $x = ab$. The local angle of flow at the tail then may be written

$$\alpha_{\text{eff.}} = \alpha_0\left\{1 + ik[(x/b) - a]\right\} - \epsilon_T \tag{7}$$

where ϵ_T is the wing downwash at the tail. Substituting ϵ from Eq. (6) and differentiating with respect to α_0, we have

$$\frac{d\alpha_{\text{eff.}}}{d\alpha_0} = \left(1 - \frac{d\epsilon_{T_0}}{d\alpha_0}\right) + ik\left[\left(1 + \frac{d\epsilon_{T_0}}{d\alpha_0}\right)\left(\frac{x}{b} - a\right) + (a - \delta)\left(\frac{d\epsilon_{T_0}}{d\alpha_0}\right)\right] + 0(k^2) \tag{8}$$

where ϵ_{T_0} is implicitly dependent on the coordinates of a point on the tail and δ on y. Now, in the absence of downwash interference, the term α_0 in $\alpha_{\text{eff.}}$ would lead to a moment derivative $C_{M_{\alpha_0}} + ikC_{M_{\dot{\alpha}}}$, the latter term being due to unsteady flow effects, while the term $ik\alpha_0[(x/b) - a]$ would lead to the derivative C_{M_q}. Hence, in the presence of interference, we write

$$\frac{dC_{M_{\text{eff.}}}}{d\alpha_0} = \left(1 - \frac{d\epsilon_{T_0}}{d\alpha_0}\right) C_{M_{\alpha_0}} + ik\left[\left(1 + \frac{d\epsilon_{T_0}}{d\alpha_0}\right) C_{M_q} + \left(1 - \frac{d\epsilon_{T_0}}{d\alpha_0}\right) C_{M_{\dot{\alpha}}} + (a - \delta)\left(\frac{d\epsilon_{T_0}}{d\alpha_0}\right) C_{M_{\alpha_0}}\right] + 0(k^2) \tag{9}$$

where ϵ_{T_0} and δ now are assumed to have been appropriately averaged over the tail. A similar result holds for the lift derivative, and entirely analogous results may be obtained for the derivatives with respect to angle of yaw. We remark that the corrections $[1 - (d\epsilon_{T_0}/d\alpha_0)]$ and $[1 + (d\epsilon_{T_0}/d\alpha_0)]$ applied to $C_{M_{\alpha_0}}$ and C_{M_q}, respectively, are standard, but the introduction of the term $C_{M_{\dot{\alpha}}}$, together with its downwash correction and the term $(a - \delta)C_{M_{\alpha_0}}$, generally is neglected. The last term is presumably the "downwash lag" term referred to by Statler. It would appear that the usual analysis of downwash in unsteady flow[3] implicitly assumes $\delta = a$.

In applying the result (9), the derivative $(d\epsilon_{T_0}/d\alpha_0)$ may be calculated from steady flow theory or measured in the wind tunnel, so that it only remains to calculate an appropriately averaged value of $\delta(y)$. If we take this average as

$$\delta = \frac{1}{S}\int_{-l/2}^{l/2} c(y)\delta(y)dy \tag{10}$$

where S, c, and l are the area, chord, and span of the *wing*, and substitute $\delta(y)$ from Eq. (4), retaining only the first power of k, we have

$$\delta = \frac{1}{S}\int_{-l/2}^{l/2} c(y)\left\{\frac{c_{l_q}(y) + c_{l_{\dot{\alpha}}}(y) + [c(y)c_{m_{\alpha_0}}(y)/b]}{c_{l_{\alpha_0}}(y)}\right\} dy \tag{11}$$

Assuming $c_{l_{\alpha_0}}$ to be constant across the wing and taking $x = 0$ at the aerodynamic center of the wing, we obtain

$$\delta = \left[(C_{L_q} + C_{L_{\dot{\alpha}}})/C_{L_{\alpha_0}}\right]_{\text{wing}} \tag{12}$$

For conventional wing-tail configurations, δ will be negative. While it would have been a better approximation to have carried out the integration of Eq. (10) over the tail rather than the wing, it appears that the result (12) should be reasonably accurate in those cases where $\delta(y)$ does not exhibit large variations across the wing span. Thus, the results should not be applied to heavily swept wings without further investigation.

References

[1] Statler, I. C., *Dynamic Stability at High Speeds from Unsteady Flow Theory*, I.A.S. Preprint 187 (New York I.A.S. meeting, January, 1949).

[2] Miles, J. W., *Unsteady Flow Theory in Dynamic Stability*, Journal of the Aeronautical Sciences, Vol. 17, No. 1, pp. 62–63, January, 1950.

[3] Durand, W. F., *Aerodynamic Theory*, Durand Reprinting Committee, Pasadena, Calif., Vol. V, pages 49–51, 1943.

* This work was carried out at the Aerophysics Laboratory, North American Aviation, Inc., during the summer of 1949.

A Note on Boundary-Layer Type Solutions in Applied Mechanics

S. F. Borg
Assistant Professor of Aeronautics, U.S. Naval Postgraduate School, Annapolis, Md.
February 1, 1950

THE EULER EQUATION for nonviscous, nonheat-conducting flow in two dimensions

$$u\frac{\partial u}{\partial x} + v\frac{\partial u}{\partial y} = -\frac{1}{\rho}\frac{\partial p}{\partial x} \tag{1}$$

may be interpreted as a balance between inertia and pressure forces.

The Navier-Stokes equation

$$u\frac{\partial u}{\partial x} + v\frac{\partial u}{\partial y} = -\frac{1}{\rho}\frac{\partial p}{\partial x} + \nu\nabla^2 u \tag{2}$$

is a balance between inertia, pressure, and viscous forces.

Prandtl's boundary layer theory assumes that

$$\frac{\text{viscous effect}}{\text{inertia effect}} \to 0$$

or that the Reynolds Number is extremely large. This leads to the familiar boundary-layer solution and holds for extremely small values of viscosity provided the length parameter in the Reynolds Number is also not small.

Equations such as Eq. (2) have been the subject of some recent study.[1] It has been shown that, if the parameter that multiplies the highest term of the differential equation approaches zero (i.e., if $\nu \to 0$ above), then the solution to the equation approaches the solution corresponding to the equation for $\nu = 0$ [Eq. (1) above], except for a narrow region within which there is a rapid transition of—in this problem—velocity.

The phenomena are dependent upon the number of boundary conditions required for a unique solution of a partial differential equation. Thus, Eq. (2) being of a higher order than Eq. (1), it requires an additional boundary condition—the no-slip condition. For $\nu \to 0$, one is tempted to neglect the last term of Eq. (2), but, if this were done, the order of the equation would be lowered, a boundary condition would be lost, and the solution (at least in the neighborhood of the boundary) would differ from the no-slip solution.

"True" boundary-layer solutions—that is, solutions in which the form of the differential equation is similar to Eq. (2)—have been discussed. Taylor and Maccoll,[2] in their analysis of the shock front of supersonic flows, obtain a boundary-layer equation that leads to the characteristic thin layer (shock thickness) as viscosity and heat conduction approach zero. The laminar flow heat convection problem[3] also leads to an equation that is identical in form to the viscous flow equation.

Friedrichs[4] discusses a differential equation that occurs in the theory of plates and shells and which physically may be thought of as a balance of

plate effect plus membrane effect = transverse load effect

and considers the case in which

$$\frac{\text{plate effect}}{\text{membrane effect}} \to 0$$

It is found that for this case the boundary layer is in the slope of the structure at the supports and, in effect, that the structure acts like a membrane everywhere except at the supports, at which place a boundary condition is lost and a rapid transition in slope takes place in a narrow region, this being the boundary layer.

Another similar, although apparently unrelated, boundary-layer type effect occurs in the theory of plates.[5] If we consider a long plate, simply supported along its long sides, free along the short sides, and uniformly loaded transversely over its area, it is found that at the short edges the plate "curls" over in a narrow region—the boundary layer for this case. The phenomenon is undoubtedly due to a boundary condition effect; some distance away from the short edges a condition of plane strain exists, whereas at the edges this condition must be given up. The boundary-layer condition described by Friedrichs may be thought of as one in which a condition of plane stress prevails throughout the plate but is given up at the edges.

Bromberg and Stoker[6] discuss a boundary-layer effect that occurs in the theory of shells which is due to the inclusion in the plate theory of certain nonlinear, higher-order terms of the strain tensor.

Two additional types of boundary-layer effects which are due to singularities in the boundary conditions and which lead to characteristic thin layer regions will be described.

The first occurs in the Lame-Clapeyron theory of axially symmetric deformations of elastic bodies. Consider a rotating circular wheel. It is found[7] that the tangential and radial stress distributions for the case in which there is a small central hole in the wheel are the same as the solutions corresponding to no hole, everywhere except for a narrow region adjacent to the hole in which there is a rapid change in the stresses. This is a boundary-layer type effect and is connected with the following singularity in the boundary condition; for the case of no hole, the boundary condition is: (a) The radial deformation is zero at the center of the wheel. For the case of a small hole, the boundary condition is: (b) The radial stress at the edge of the hole is zero. The differential equation in deflection is the same for both cases, but in going from small hole to no hole there is a singularity in the boundary condition. The solution is similar in many respects to that of the small circular hole in an infinite plate subjected to tension stress. Also, there appears to be some connection with the St. Venant Principle.

Another boundary-layer effect occurs in the direct compression-buckling loading of a rod. If we consider the ratio of effects

$$\frac{\text{buckling (bending) stress}}{\text{direct compression stress}} \to 0$$

it is found that the governing parameters are the slope (θ) and the slenderness ratio (l/ρ) of the bar. The slenderness ratio being fixed in any given problem, it becomes necessary that the slope approach zero.

The problem can be set up as follows: for zero slope,

$$\sigma = P/A \tag{3}$$

for small slope,

$$\begin{cases} \sigma = (P/A) \pm [(Py)c/I] & (4a) \\ EI(d\theta/dS) = Py & (4b) \end{cases}$$

in which

σ = stress
P = load
A = area
y = deflection
c = distance from neutral axis of bar
EI = stiffness
dS = differential length along bar

For extremely small θ, the stress (4a) is nearly the same as the stress (3) for all values of P less than P_{Euler}. As P approaches and then exceeds P_{Euler}, it is found[8] that there is a rapid increase in σ corresponding to a small increase in P. Thus, the boundary-layer "region" in this case is the load P, and the term that corresponds to the velocity of the viscous boundary layer is the stress. For small θ, a boundary condition on the slope at the top of the bar is required, whereas for zero slope no boundary condition is needed. Thus, in going from small slope to zero slope a boundary condition is lost.

A familiar example of some interest—in that it indicates the importance of losing a boundary condition (dropping the highest order term of the differential equation)—in the boundary-layer type solution is the comparison of Stokes and Oseen flows.[9] The Stokes flow is a balance of viscous and pressure forces and leads to

$$\nu\nabla^2 u = (1/\rho)(\partial p/\partial x) \tag{5}$$

The Oseen improvement introduces a perturbation inertia term (first order in the differential equation)

$$U\frac{\partial u}{\partial x} + \nu\nabla^2 u = \frac{1}{\rho}\frac{\partial p}{\partial x} \qquad (6)$$

and now it is found that the flows of Eqs. (5) and (6) are the same in the boundary layer adjacent to the body but differ in the large region away from the boundary layer—which is just the reverse of the usual boundary-layer effect.

In concluding, we note that it would seem probable that a solution to certain plastic flow problems might be given in terms of boundary-layer solutions. For example, the occurrence of Lueders' lines appears to have some features that are typical of boundary layers, including that of a limiting ratio of effects—namely,

$$\frac{\text{plastic effects}}{\text{elastic effects}} \to 0$$

References

[1] See, for example, Friedrichs, K. O., *The Edge Effect in Bending and Buckling with Large Deflections*, Proceedings of Symposia in Applied Mathematics, Vol. 1, p. 188; American Mathematical Society, New York City, 1949.

[2] Taylor, G. I., and Maccoll, J. W., *The Mechanics of Compressible Fluids*, Aerodynamic Theory, Vol. 3, p. 218; Julius Springer, Berlin, 1935.

[3] Dryden, H. L., *Aerodynamics of Cooling*, Aerodynamic Theory, Vol. 6, p. 237; Julius Springer, Berlin, 1935.

[4] Loc. cit.

[5] Timoshenko, S., *Strength of Materials*, Vol. 2, p. 120, 2nd ed.; D. Van Nostrand Company, Inc., New York, 1941.

[6] Bromberg, E., and Stoker, S. J., *Non Linear Theory of Curved Elastic Sheets*, Quarterly of Applied Mathematics, Vol. III, No. 3, p. 246, 1945.

[7] Timoshenko, S., *Strength of Materials*, Vol. 2, p. 248, 2nd ed., D. Van Nostrand Company, Inc., New York, 1941.

[8] Timoshenko, S., *Theory of Elastic Stability*, p. 69, 1st ed.; McGraw-Hill Book Company, Inc., New York and London, 1936.

[9] Lamb, Horace, *Hydrodynamics*, Loc. cit., 612, 6th ed.; Dover Publications, New York, 1945.

Dynamic Stability at High Speeds from Unsteady Flow Theory

(*Continued from page 242*)

[17] Lagerstrom, P. A., and Graham, M. E., *Downwash and Sidewash Induced by Three-Dimensional Lifting Wings in Supersonic Flow*, Douglas Aircraft Company Report No. SM-13007, April, 1947.

Appendix

Specifications of Airplane Used in Example

(*A*) *Airplane—General*

The airplane is a low-wing, fighter type, powered by a jet-propulsion engine exhausting through the extreme aft end of the fuselage. The gross weight is 10,000 lbs., and, with a center of gravity location of 27 per cent mean aerodynamic chord, the moment of inertia about the lateral axis, I_Y, is 13,780 slugs-ft.^{2} The overall fuselage length is 34.5 ft.

(*B*) *Wings*

The span is 40 ft.; area, 240 sq.ft.; mean aerodynamic chord (M.A.C.), 6.75 ft.; and aspect ratio, 6.

(*C*) *Horizontal Stabilizer*

The span is 16 ft.; area, 45 sq.ft.; aspect ratio, 6; elevator hinge centerline, at 75 per cent chord; and tail length (distance from $c/4$ of wing M.A.C. to $c/4$ of tail M.A.C.), 15 ft.

Services of the Libraries of the Institute of the Aeronautical Sciences

The services of the Libraries are available to all members of the Institute, to Corporate Members, to advertisers in the AERONAUTICAL ENGINEERING REVIEW and AERONAUTICAL ENGINEERING CATALOG, and, under usual library limitations, to the public. Four specialized services are available.

The Paul Kollsman Lending Library

This lending library service makes available, *without charge*, the latest and more important aeronautical books.

Members may request the loan of any aeronautical or technical book they wish to borrow. Through an exchange agreement with the Engineering Societies Library, any book on general engineering may be borrowed from its great collection of over 160,000 volumes.

A photostating service is available at usual library rates.

Applications for membership in the library and further information will be sent on request.

The W. A. M. Burden Reference Library

This reference library contains over 12,000 aeronautical books, magazines, pamphlets, and reports gathered from world-wide sources and is one of the most complete aeronautical libraries in the world. Material from this library is not available for loan but may be used for reference purposes.

The Pacific Aeronautical Library

7660 Beverly Boulevard
Los Angeles 36, California

Established in cooperation with the aircraft companies the library serves. The leading aircraft companies in or near Los Angeles participate in its support and operation.

This service library for aeronautical research is available to the public for reading privileges. Source material includes aerodynamic and structural research reports, as well as books on drafting, production methods, history, and allied sciences. It furnishes books, periodicals, and pamphlet material to the participating aircraft companies to supplement their engineering libraries.

Technical Information Service

This service has experienced personnel under the supervision of trained aeronautical engineers to compile any information desired. The services range from listing specialized reference books to the preparation of exhaustive bibliographies, digesting of reports, and general surveys of any aeronautical subject. Some of the available services are:

Bibliographies on any aeronautical subject.
Reports on any aeronautical subject.
Digests of aeronautical books, papers, periodicals, and references.
Translations.
Engineering investigations of special aeronautical subjects.
Biographies of individuals engaged in aeronautics.
Photostats of any aeronautical or general engineering material.
Microfilms made on special order.
Photographs made from the Institute's photographic collection.
Drawings and tracings made.

In addition to the services mentioned any commission which comes within the scope of the Service will be accepted. Special arrangements may be made for work requiring several weeks or months.

Translators are available for accurate transcriptions of all foreign language data. Translations are carefully edited by trained engineers.

Reproductions of any material in the collections of the Institute may be ordered at standard photostat rates.

INSTITUTE OF THE AERONAUTICAL SCIENCES, INC.
2 EAST 64th STREET, NEW YORK 21, N.Y.